UNIVERSITÀ DEGLI STUDI DI PADOVA

SCUOLA DI SCIENZE
Dipartimento di Geoscienze
Direttrice Prof.ssa. Cristina Stefani

TESI DI LAURE MAGISTRALE
IN
GEOLOGIA E GEOLOGIA TECNICA

DEGASSING FROM SEDIMENTS INTRUDED BY CAMP BASALTS DURING THE END-TRIASSIC EXTINCTION EVENT

Relatore: Prof. Andrea Marzoli
Correlatore: Prof. Nereo Preto

Laureando: Lucrezia Valeriani
Matricola: 1128906

ANNO ACCADEMICO 2016/2017

Abstract

Riassunto

1 Introduction 1
  1.1 Large Igneous Provinces and mass extinctions 1
  1.2 The Central Magmatic Province 4
  1.3 The Triassic-Jurassic boundary mass extinction 6
    1.3.1 The Triassic-Jurassic boundary and the negative CIEs 9
  1.4 CAMP timing 10
2 Thermal metamorphism 15
  2.1 The thermal metamorphism theory 15
  2.2 Contact metamorphism of organic and inorganic material 17
  2.3 Organic matter and gas generation 20
    2.3.1 Gases as product of contact metamorphism 20
    2.3.2 The organic matter and its gaseous products 21
  2.4 The effect of a single sill and multiple sill intrusions on gases formation. 24
  2.5 Hydrothermal venting and breccia pipes: how gases escape to atmosphere 27
3 Samples’ geographic origin: basins stratigraphy and formation 31
  3.1 The Central Atlantic Margin basins and the rifting of Pangea 31
    3.1.1 The Arganà Valley 35
    3.1.2 The Newark Basin 37
  3.2 The Amazonas Basin 41
4 Sampling 45
  4.1 Sampling in the Arganà Valley 46
  4.2 Sampling in the Newark Basin 47
  4.3 Sampling in the Amazonas Basin 49
5 Methods 51
  5.1 Geochemical analyses 51
    5.1.1 Sample preparation 53
    5.1.2 Mass Spectrometer analytical error and sensitivity 54
  5.2 XRPD analyses 55
  5.3 Scanning Electron Microscope (SEM) analyses 56
  5.4 Vitrinite reflectance analyses 58
  5.5 Rock-Eval Pyrolysis analyses 59
6 Numerical Modeling: a 1D Sill Model 61

- 6.1 Model Input File 62
- 6.2 Method 65
  - 6.2.1 Thermal Diffusion 66
  - 6.2.2 Thermal maturation of organic matter 68
- 6.3 Model Output: Graphical User Interface (GUI) 71
- 6.4 Model limitations 74

7 Results 75

- 7.1 Geochemical Results 75
  - 7.1.1 Geochemical results for Brazilian samples 75
  - 7.1.2 Geochemical results for Moroccan samples 78
  - 7.1.3 Geochemical results for American samples 80
- 7.2 Vitrinite Reflectance results 82
- 7.3 Rock-Eval analyses results 84
- 7.4 XRPD analyses results 86
  - 7.4.1 XRPD results for the Brazilian samples 87
  - 7.4.2 XRPD results for the U.S.A. samples 88
  - 7.4.3 XRPD results for the Moroccan samples 91
- 7.5 SEM analyses results 94
- 7.6 SILLi model results 95
  - 7.6.1 Model results for Amazonas samples 95
  - 7.6.2 Model result for the Moroccan samples 97
  - 7.6.3 Model result for the U.S.A. study case 99

8 Conclusions 101

References 105

Acknowledgements 119

Abstract

Between the end of the Triassic and the beginning of the Jurassic one of the most important Phanerozoic mass extinction events occurred. During the end-Triassic biotic crisis the loss of ca. 50% of the marine genera and a significant turn-over of the terrestrial fauna and flora happened. It is also coincident with carbon cycle perturbations, characterized by three negative carbon isotope excursions. In correspondence with the end-Triassic biotic crisis, the Central Atlantic Magmatic Province, one of the largest magmatic province on our planet, emplaced (~ 201.5 Ma). It has been suggested that CAMP could have triggered this biotic crisis and the environmental changes associated with it (increase in atmospheric pCO_2 level, global warming, oceans stratification and acidification). Particularly, it has been proposed that sill emplacements could have generated a degassing of CO_2 of both organic and inorganic origin. Here, we investigate the impact of sill intrusions on the sedimentary rocks and particularly on the organic matter. Three study cases have been considered: the Amelal sill, outcropping in the southern portion of the Arganà valley (Morocco), the Palisades sill, intruded in the lower portion of the Lockatong Formation in the Newark basin (U.S.A.) and a sill intruded within the Nova Olinda Formation in the Amazonas basin (Brazil). Different kinds of analysis have been conducted in order to constrain the metamorphic effects of sill intrusions on the surrounding rocks and their organic matter: XRPD and SEM, $\delta^{13}C$ and T.O.C. through mass spectrometry, vitrinite reflectance and Rock-Eval analyses. Furthermore, 1D models have been calculated to quantify the amount of organic origin CO_2 released into the atmosphere during sill emplacements. The T.O.C. and the vitrinite data obtained by the analyses have been inserted in the model, besides other parameters, as i.e. rock densities, the initial T.O.C., rock heat capacities and thermal conductivities.

This research, even if it considers only the case of three sills is the most complete ever done on CAMP sills and demonstrates that the sill emplacement can be one of the most important factors triggering the end-Triassic climate changes. Particularly, we have noticed that the amount of produced CO_2 is not controlled

only and mainly by the thickness of the sill: the Brazilian sill, the thinner one, produced an amount of CO_2 larger than the 100 m thick Amelal sill. Also, degassing from organic matter happens at relatively low temperature making a prolonged heating at temperatures of about 100-200 °C more effective than very high temperatures contact metamorphic temperatures maintained for only short times. In this sense, the effects of sill intrusions are enhanced in the case of multiple intrusions rather than by intrusion of single sills. Crucial is the amount of original T.O.C. and the number of multiple sill intrusions in the studied basins. So, in basins as Amazonas basin or Solimões basin (Brazil) the amount of produced CO_2 is very high and has a great impact on the climate. Finally, it should be remembered that multiple sill intrusions affected also other regions of the CAMP (e.g. Guinea, Mali, Burkina Faso, Bolivia, the Pyrenees) besides those studied here.

The obtained carbon isotopic data show that the studied sedimentary rocks have low $\delta^{13}C_{org}$ (in the range -25 to -28‰). Emission of CO_2 (or CH_4) with such isotopic signature would explain the carbon isotopic shifts occurring during the last few hundred thousand years of the Triassic. It is also noteworthy that the $\delta^{13}C_{org}$ of the studied sedimentary sequences does not show any significant correlation with calculated temperatures, vitrinite reflectance, or, in general, distance from the sill. This suggest that the thermal effects of sill emplacement did not significantly fractionate the carbon isotopic composition of the residual organic matter.

Riassunto

Fra la fine del Triassico e l’inizio del Giurassico si verificò una delle più importanti estinzioni di massa del Fanerozoico. In questo frangente si estinsero circa il 50% degli organismi marini, fra cui i conodonti, e si verificò un importante turn-over della flora e della fauna terrestre. Associati all’ estinzione di massa vi sono tre shift isotopici negativi del Carbonio, rinominati come precursore, iniziale e principale. Oltre a tali perturbazioni del ciclo del Carbonio, si verificarono anche una serie di altri cambiamenti ambientali fra cui un aumento della pCO_2, l’ acidificazione e la stratificazione degli oceani ed un aumento delle temperature a livello globale. In corrispondenza del limite tra Triassico e Giurassico, inoltre, si mise in posto una delle più grandi province magmatiche affioranti oggigiorno sul nostro pianeta, la CAMP. E’ stato suggerito più volte come la CAMP possa essere una delle dirette responsabili dell’ estinzione di massa verificatasi in concomitanza della sua messa in posto. Il rilascio di anidride carbonica direttamente dal magma non basta però da solo a giustificare la formazione delle escursioni isotopiche negative sopra citate. L’ attività della CAMP potrebbe aver, per esempio, contribuito alla destabilizzazione dei gas termogenici, fra cui compaiono i clatrati, caratterizzati da un’ impronta isotopica del -60‰. Inoltre, un’ importante fonte di rilascio di anidride carbonica isotopicamente leggera ($\delta^{13}C$ = -35/-50‰) potrebbe derivare dall’ intrusione superficiale di sill entro successioni sedimentarie. Nel corso dello studio sono, quindi, stati considerati dei campioni appartenenti a tre diverse successioni sedimentarie intruse da tre sill. I campioni studiati provengono dal Marocco, dagli U.S.A. e dal Brasile. Su di essi sono stati effettuati diversi tipi di analisi per riuscire a quantificare gli effetti del sill sui sedimenti circostanti e sulla materia organica in essi contenuti. Sono state effettuate analisi geochimiche sulla materia organica, analisi al SEM, analisi di riflettanza di vitrinite, la Rock-Eval ed analisi in diffrazione da polvere. Alcuni dei dati ottenuti dalle analisi, fra cui i valori della riflettanza di vitrinite ed i dati di T.O.C., sono stati poi utilizzati per sviluppare un

modello 1D volto a quantificare la quantità di materia organica rilasciata in atmosfera a seguito della messa in posto dei sill. Dai risultati ottenuti dal modello si può dedurre che il degassamento di CO_2 a seguito della messa in posto dei sill può essere ritenuto uno dei meccanismi principali innescanti l’ estinzione di massa. In particolare, alla luce dei risultati ottenuti, risulta essere interessante il fatto che in zone come il Brasile o la Guinea vi siano moltissimi sill, dalle dimensioni variabili, intrusisi entro successioni sedimentarie. L’ effetto di molti sill, anche di piccole dimensioni, è stato stimato essere molto più importante rispetto all’ effetto di un unico grande sill, per cui in tali regioni si potrebbe essere verificato un degassing di grande entità che avrebbe, quindi, influenzato in modo consistente il clima e l’ ambiente della fine del Triassico.

1 Introduction

1.1 Large Igneous Provinces and mass extinctions

A Large Igneous Province (LIP; Fig. 1.1) is an abnormal and transient igneous event in Earth's history during which huge amounts of magma have been produced and subsequently erupted over a large area in a short period of time (Jones et al., 2016; Bryan et al., 2010). Due to their wide scale and relatively rapid emplacement, LIPs have been recently recognized as possible responsible for several Phanerozoic mass extinctions.

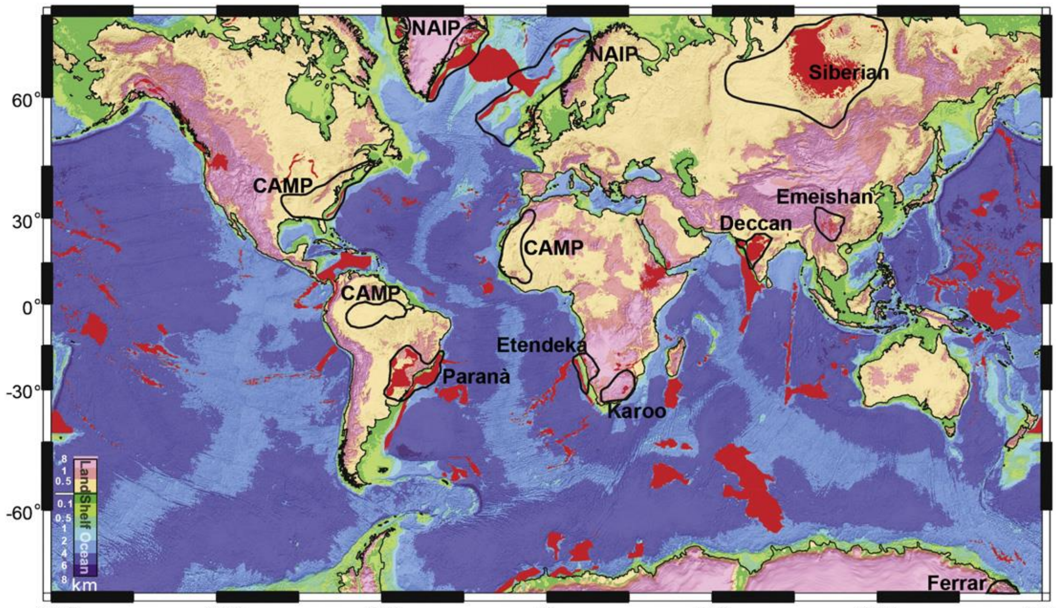

Fig. 1.1 The global distribution of LIPs and associated volcanic basins. LIPs product at the surface are reported in red, while the areas surrounded by black circles show the location of the most studied or the most important magmatic provinces (Jones et al., 2016).

The temporal and causal link between LIPs and rapid environmental and biosphere changes has been dealt with and debated for many years (Svensen et al., 2015). One of the most important problems is the relative timing between the biotic crisis and the LIP formation. Examining the timing of the Phanerozoic mass extinctions and the formation ages of LIPs, it is possible to observe a temporal correspondence for four of the five largest extinction events (i.e. the end-Permian extinction and the Siberian Traps; the K-Pg biotic crisis and the Deccan Traps) and for most minor crises since the Permian (Wignall, 2001). Interestingly, in some cases the onset of eruptions post-dates the main phases of extinctions: this could be due to several factors, including a non-complete knowledge of the evolutionary history of magmatic provinces or an inaccurate dating of one of the two events.

To understand how magmatic provinces may have caused mass extinctions, their impact and effects on climate must be considered (Fig. 1.2). Emission of a large amount of gases, such as carbon dioxide (CO_2) and sulphur dioxide (SO_2), is linked with magmatic activities and volcanic outpourings. Although they may both act as greenhouse gases, their effects are diametrically opposed and affect the climate for different periods of time (Wignall, 2001). The initial effect of sulphur dioxide is to cause warming of the stratosphere, but cooling of the troposphere. In the atmosphere, SO_2 reacts rapidly with water to give origin to sulphate aerosols. Sulphate aerosols reflect and absorb solar radiation within the stratosphere, causing a cooling below it (Jones et al., 2016; Sigurdsson,1990). Such effects are manifested on a large scale when the gases are injected into the low stratosphere where they are rapidly dispersed by the currents throughout the hemisphere. If they are not injected into the low stratosphere, their effects will be localized near the eruption area. Because of the rapid rain-out of the sulphate aerosols, usually their effects last only one or two years (Wignall, 2001). Vice versa, CO_2 has a longer residence time (a few centuries) in the atmosphere and its effects trigger larger scale, greater amplitude and longer duration climatic changes. Particularly, the effects of repeated large eruptions, typical of CFBs (Continental Flood Basalts), could be very significant from a climatic point of view (Wignall, 2001).

Another important greenhouse gas released into the atmosphere during LIPs eruptions is methane (CH_4). Rather than being a direct product of volcanism, methane is released chiefly through degassing of organic matter rich sediments or by clathrates, which are destabilized by heating due to the magmatic activity. The effect of CH_4 is to induce an atmospheric warming, as in the case of CO_2. The important difference between these two greenhouse gases is that methane has a stronger effect on the climate than CO_2 but has a reduced residence time (a few decades) in the atmosphere due to its rapid oxidation to produce CO_2 (Jones et al., 2016). Other gases released into the atmosphere by magmatic activity are chlorine (Cl_2), the effect of which is represented by an ozone depletion, hydrochloric acid (HCl), hydrofluoric acid (HF), sulfuric acid (H_2SO_4), which, together with HCl and HF, favors acid rain formation, and water (H_2O) (Wignall, 2001).

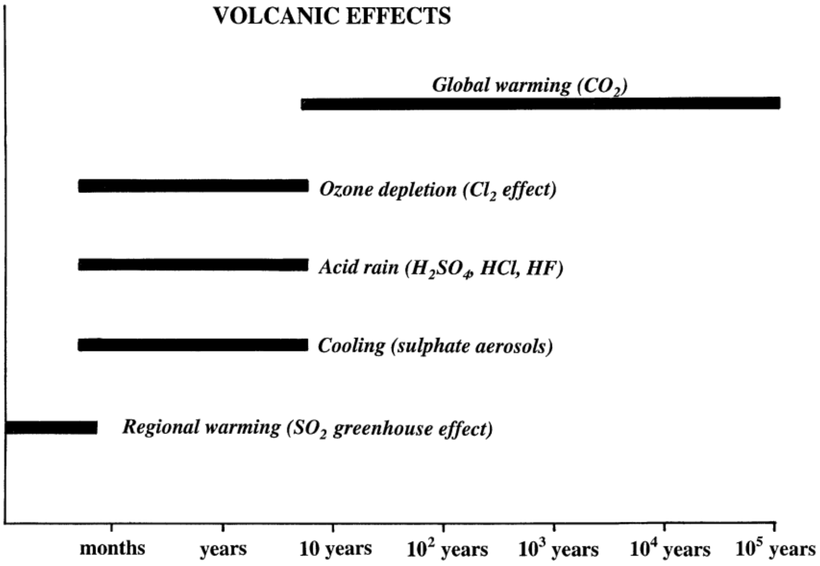

Fig. 1.2 Here the effects of the various volcanic gases released into the atmosphere are reported. Particularly, the duration of the volcanic gases effects is illustrated. So, it is possible to observe that the effects of some gases persist for a few months, whereas the effects of other gases, as CO_2, persist for a very long period of time (in the order of 10-10^5 years).

Sometimes volcanic emissions of CO_2 are not enough to justify negative carbon isotope excursions (CIEs) associated with some extinction events. In fact, the amount of CO_2 of mantellic origin required to explain and justify the emissions into the atmosphere, the CIEs and environmental and climatic changes may be too great (Ruhl and Kürschner, 2011). Moreover, magmatic-carbon originated from the mantle should be characterized by an isotopic composition of -5‰ or -6‰ ($\delta^{13}C$ vs. PDB), which can hardly explain a CIE, considering that atmospheric carbon has a $\delta^{13}C$ of about -8‰. We must therefore consider the effects of magmatic provinces on the dissociation of gas hydrates (clathrates) and on carbon-rich sedimentary sequences within which magmatic bodies (i.e. sills) intruded. One point in favor of this theory are the potentially quite low ($\delta^{13}C$) isotopic compositions of organic matter (ca. -25‰ to -30‰) and of methane clathrates (< -30‰).

1.2 The Central Magmatic Province

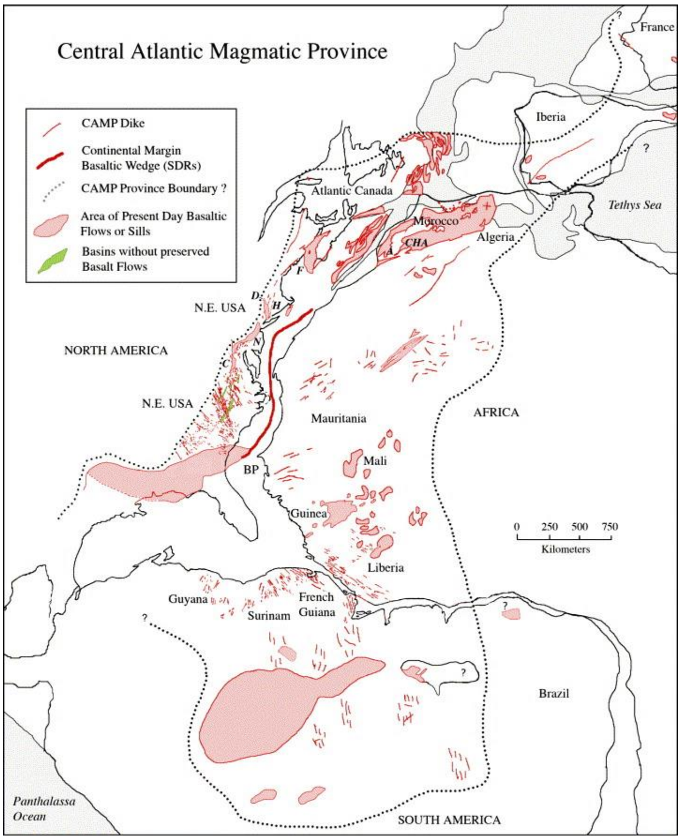

Fig. 1.3 The extension of the CAMP are shown here. It is possible to observe the country in which CAMP basalt (lavaflows, sills or dikes) outcrop (from McHone, 2000)

The Central Atlantic Magmatic Province (CAMP, Marzoli et al., 1999; Fig. 1.3) is one of the largest magmatic provinces on our planet, with an estimated area of 10^7 km^2 (Davies et al., 2017; Blackburn et al., 2013). It is represented by tholeiitic dykes, sills, layered intrusives and basalt flows, outcropping in North and South America, Africa and Europe (Davies et al. 2017; Marzoli et al. 1999). CAMP magmatic activity occurred in a relatively short period of time, with a peak at about 201.5 Ma, and it is associated with the breakup of Pangea and the formation of the Central Atlantic Ocean (Bertrand, 1991; Marzoli et al., 1999; Mc Hone, 2000). It is no coincidence that the lava-flows, sills and dikes remnants are mostly related to Triassic rift basins (i.e. in Portugal, Morocco, Brazil and Eastern North America) formed during extensional tectonics, occurred before the Pangea disruption (Bertrand, 2014). Nowadays CAMP rocks outcrop along both sides of the Central Atlantic Ocean, from North America (U.S.A. and Canada) to North Western Africa (Morocco, Algeria, Mali, Mauritania, Guinea, Liberia, Burkina Faso, Sierra Leone, Ghana, Ivory Coast and Senegal), from South America (Brazil, Bolivia, French Guyana, Guyana, Surinam and Venezuela) to Western Europe (France, Portugal, Spain). Although CAMP rocks are visible in such countries, the global volume of CAMP was reduced by a probable post-magmatic erosion (Marzoli et al, 2004), as evidenced by negative Sr and Os trends recorded by marine strata of the first Jurassic (Cohen and Coe, 2002; Callegaro et al., 2012).

Traces of CAMP emplacement are visible as seismetes and soft sediment deformation structures (syn-depositional or formed shortly after deposition of sediments) in many localities (Poland, Sweden, Luxemburg, Hungary, Slovakia, France, Southern Alps in Italy) (Lindström et al., 2015). The CAMP is commonly believed to be the responsible for the end-Triassic mass extinction. In the last decades, many evidences have been found to support this thesis, but also many criticisms have been taken against it. Precise dating and volume estimation and a good comprehension of large igneous provinces effects are required to understand the role of CAMP on the T-J boundary mass extinction.

1.3 The Triassic-Jurassic boundary mass extinction

A mass extinction event is generally defined as “a geologically brief interval (i.e. ~1 Ma) of elevated extinction rate that affects several taxa from a wide range of habitats (i.e. terrestrial and marine) all over the world” (Hallam and Wignall, 1997).

Nowadays the boundary between Triassic and Jurassic is based on the GSSP section of Kuhjock pass, in the Northern Calcareous Alps, Austria (Fig. 1.4). The beginning of the Jurassic is defined by the first appearance of the Hettangian (Early Jurassic) ammonite *Psiloceras Spelae* tirolicum species (Hillebrandt et al., 2013). Relying on the last occurrence of Triassic choristoceratid ammonoids and the first appearance of Jurassic psiloceratid ammonites, it has been possible to correlate the Northern Calcareous Alps sections with other TJB (Triassic-Jurassic boundary) successions in British Columbia (Canada; Ward et al. 2004; Williford et al., 2007), Nevada (U.S.A.; Guex et al. 2004, 2009) and Peru (Schoene et al., 2010) (Lindström et al., 2017).

Fig. 1.4 In the orange rectangle with black border rectangle the geographical location of the Triassic-Jurassic boundary sections in the eastern part of the Northern Calcareous is showed (modified from Hillebrandt et al., 2013).

Between the end of the Triassic and the beginning of Jurassic, ~ 201.3 Ma, one of the most important Phanerozoic mass extinctions occurred. The end-Triassic biotic crisis is characterized by the loss of ca. 50% of marine genera and a significant turn-over of the terrestrial fauna and flora (McElwin et al., 2009; Raup and Sepkoski, 1982; Spencer and Tanner, 2015;

Tanner et al., 2004). Among the species particularly affected by the mass extinction in the marine realm appear conodonts, radiolarians, bivalves, ammonoids and reef-building organisms (Spencer and Tanner, 2015; Tanner et al., 2004). Conodonts suffered complete extinction (Tanner et al., 2004) and there was the last occurrence of the Rhaetian ammonite *Choristoceras crickmayi*. Scleractinian corals, that became significant reef builders in the Triassic, also suffered a sharp decline followed by a phase of ‘‘reef gap’’ during the Hettangian and Early Sinemurian (Tanner et al., 2004). In the Thetyan realm the entity of the mass extinction is observed on reef communities, where the reef ecosystem was affected by a generalized collapse and there was a momentary cessation of carbonate sedimentation (Tanner et al., 2004). However, according to some authors (Hallam and Goodfellow, 1990) the reef collapse was caused by a sea level change. Marine phytoplankton also suffered strong losses during the end-Triassic extinction event, especially in the case of dinoflagellate cyst family *Suessiaceae*.

At the Tr-J boundary according to several authors a profound palynomorph extinction happened: in Olsen and Sues (1986), the Newark basin case is reported. Among spore and pollen taxa disappeared during or just after the mass extinction event can be counted *Granulopercilatipollis rudis*, *Rhaetipollis Germanicus*, *Ovalipollis ovalis*, *Limbosporites lundbladiae*, *Semiretisporis gothae*, *Polypodiisporites polymicroforatus* and *Ricciisporites tuberculatus*, all used as markers (Lindström et al., 2017).

As far as plants concerned, according to Ash (1986) seed sperns were primarly involved by the important changes occurred at the Triassic-Jurassic boundary: they recorded the loss of *Glossopteridaceae*, *Peltaspermaceae* and *Corystospermaceae* families (Ash, 1986; Traverse 1988; Tunner et al., 2004). Note that the question of how mass extinction struck is still debated. The Tr-J mass extinction event is temporary very close to a sequence of three globally observed CIEs in $\delta^{13}C_{TOC}$ records (TOC: Total Organic Carbon; Fig. 1.5), suggesting the possibility of an input of substantial quantities of gases such as CH_4 or CO_2, characterized by low $\delta^{13}C$, into the ocean-atmosphere system. One of the three negative excursion has been observed only recently: it is represented by a negative Rhaetic precursor Carbon isotope shift (~ -2‰/-3‰) (Lindstrom et al., 2017; Ruhl and Kürschner, 2011). The other two negative excursions are represented by an end-Rhaetian maximum negative shift of -8.5‰, followed, after a period of positive excursion, by a long-term -3.5‰ main negative Carbon isotope shift (Lindström et al., 2017; Ruhl et al., 2011).

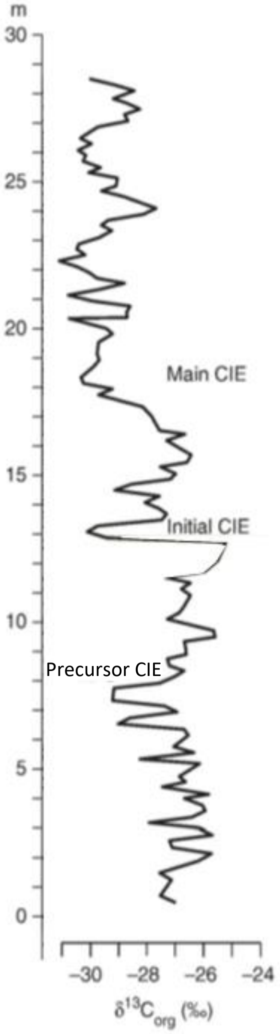

Fig. 1.5 C-isotope record for the St. Audrie' s Bay is showed here. In this record it is possible to observe the precursor CIE, the initial CIE and the main CIE (modified from Lindström et al., 2017).

Even if C-isotope analyses of some LIP basalt samples (not from the CAMP), yielded quite negative $\delta^{13}C$ values (-25‰ average) in a study of Hansen (2006), it is generally assumed that mantle-derived basalts, such as those from the CAMP, should have much higher $\delta^{13}C$ (ca -5‰). According to these data, negative carbon isotope excursions could not be produced only by CAMP emissions. Probably, they could be produced principally by shallow intrusions of magmas causing thermal metamorphism on subsurface strata rich in organic matter (Ruhl and Kürschner, 2011; Svensen et al., 2004), and by gas hydrates (whose original isotopic imprint is of about -60‰) destabilization (Ruhl et al., 2011). Note that these hypotheses are not mutually exclusive. Indeed, CAMP volcanism may have triggered the release of both thermogenic gases and clathrates emissions, amplifying the pCO_2 atmospheric increase effects on climate and environment (Schaller et al., 2011) and further promoting the resulting global warming, oceans acidification and stratification (Martindale et al., 2012).

Particularly, as suggested by Ruhl and Kürschner (2011), the Rhaetian precursor shift could be due to thermogenic gas emissions, happened because of early CAMP magmatic activity during which dikes and sills intruded just before CAMP lava flows. Ruhl and Kürschner (2011) also proposed a thermogenic emission of nearly 3000-7000 Gt of istopically light carbon to give origin to the negative precursor shift.

1.3.1 The Triassic-Jurassic boundary and the negative CIEs

In a recent research, conducted by Lindström et al. (2017), CIEs were studied and renamed. Lindström et al. (2017) based their work on combined palynological and ammonite correlation. The first negative carbon isotope excursion, defined by Ruhl and Kürschner (2011) as the Rhaetian precursor negative Carbon isotope shift (Fig. 1.5), was renamed Marshi CIE, on the base of the last occurrence (LO) of the *Choristoceras marshi* ammonite. The second negative shift, characterized by a $\delta^{13}C$ excursion of -8.5‰ (Fig. 1.5), was defined Spelae CIE, because of its concomitance with the first occurrence (FO) of the ammonite *Psiloceras Spelae* (note that the FO of the *P. Spelae* happened during the upper part of this isotopic negative excursion). The last one, that is the long-term main negative shift (-3.5‰; Fig. 1.5), occurred within the upper Tilmanni Zone, was called top-Tilmanni CIE.

As previously said, the first occurrence of *P. Spelae* determines the base of the Jurassic (Hillebrandt et al., 2013) and was dated at 201.36 ± 0.17 Ma (the age was obtained by dating two ash beds, respectively in New York Canyon, U.S.A., and in Pucara Basin, Peru; Schoene et al., 2010; Wotzlaw et al., 2014). The temporal period included between the LO of *Choristoceras marshi* (ca. 201.51 ± 0.15 Ma; Lindström et al., 2017) and the Triassic-Jurassic boundary, according to Lindström et al. (2017), corresponds to the time interval in which the end-Triassic mass extinction occurred.

1.4 CAMP timing

Nowadays there is a large amount of radio-isotopic ages available for the Central Atlantic Magmatic Province, represented mainly by $^{40}Ar/^{39}Ar$ dates, but also by several U/Pb ages. Because of the analytical uncertainty characterizing the various dating techniques and the possible alteration of sampled rocks, not all the dates that have been produced are exactly correct. Careful selection and revision of the produced ages (i.e. Marzoli et al., 2011) proves to be necessary to quantify the effective temporal distribution of CAMP magmatism. The U/Pb system accuracy is higher than the $^{40}Ar/^{39}Ar$ system accuracy. Moreover, there are some evident systematic differences between the two dating systems. First of all, the two systems date different minerals (zircon and plagioclase respectively) which have diverse closing temperatures, thus registering different ages. Secondly, the ^{40}K decay constant is less well-known than the U decay constant. This also makes the use of stratigraphic techniques necessary to obtain a correct understanding of the correlation between the CAMP and the

Triassic-Jurassic boundary. And so, biostratigraphy, magnetostratigraphy and geochemical stratigraphy give an important contribution to define the sequence of the events.

In a recent research (Davies et al., 2017), high precision U/Pb ages for zircon ($ZrSiO_4$) and baddeleyite (ZrO_2) from mafic intrusive CAMP rocks have been presented. Particularly, they presented a dating of 201.635 ± 0.029 Ma for the Kakoulima mafic intrusion in Guinea: this would seem to be the oldest age for CAMP magmatism. As stated by the authors, it is 150 ± 38 ka older than the North Mountain basalt (Fundy Basin, Nova Scotia) and 71 ± 61 ka older than the Amelal sill (Morocco), the oldest dates up to now attributed to CAMP activities. These new dating, presented in Davies's research, would agree with what has been said by Dal Corso et al. (2014), who suggested a mafic origin for the trioctahedral sheet silicates contained in Upper Triassic sediments analyzed from two different Moroccan sections. Such dates, obtained by Davies et al. (2017), indicate that the beginning of CAMP magmatism predates the mass extinction event (201.51 ± 0.15 Ma in marine realm, Schoene et al., 2010; 201.564 ± 0.015 Ma for the terrestrial end-Triassic mass extinction, Blackburn et al., 2013). So, most of CAMP activity may have occurred in correspondence with the end-Triassic mass extinction (Davies et al., 2017). Particularly, according to Davies et al. (2017), CAMP sills from the trans-Amazonian basins would have intruded at 201.525 ± 0.065 Ma. Such a scenario would see thermal metamorphism as one of the main causes of CO_2 and CH_4 degassing from organic sediments into the atmosphere and so it could be one of the possible responsible for the CIEs linked to the mass extinction (Davies et al., 2017; Svensen et al. 2004). With this in mind, it should be remembered how magmatic intrusions into Brazilian sedimentary basins (i.e. Amazonas and Solimoes basins) caused an alteration of thermal history that was able to cause petroleum generation and migration (Filho et al., 2008).

Different studies realized in the last years (Knight et al, 2004; Marzoli et al., 2004; Panfili et al., 2017) show how CAMP emplaced in a very short period of time.

Particularly, several palynological studies have been conducted in Morocco (Dal Corso et al., 2014; Marzoli et al., 2004; Panfili et al., 2017), where it is possible to observe four magmatic formations, subdivided on the base of geochemical, magnetostratigraphic and volcanological data (Bertrand, 1991; Knight et al., 2004; Marzoli et al., 2004). These formations are called Lower, Intermediate, Upper and Recurrent basalts and have been dated with a lot of high quality ages (Knight et al., 2004; Marzoli et al., 2011; Nomade et al., 2007; Verati et al., 2007). All the data suggest that Lower to Upper basalts emplaced in a short range of time at ~201 Ma; Recurrent basalts result to be younger (~199 Ma) (Panfili et al., 2017). This has been confirmed by a recent study conducted by Panfili et al. (2017), based on the main palynological taxa. By using palynological assemblages, characterized by the *Classopollis group* in association with *Patinasporites densus*, Panfili et al. (2017) obtained a Rhaetic age for sedimentary strata above the Upper basalt, also confirming previous researches according to which the sedimentary layers below the first flow date back to Rhaetian ages (Dal Corso et al., 2014; Marzoli et al., 2004). Palynological data seem also to be consistent with the Rhaetian age attributed to the Intermediate CAMP basaltic unit (Blackburn et al., 2013).

This implies that CAMP activity in Morocco occurred entirely during the late Triassic, with the exception of Recurrent basalts (emplaced ~199 Ma). These data leave space for a scenario in which most of CAMP emplaced more or less at the same time as the ETE (end-Triassic mass extinction; Lindström et al., 2017) and happened as a very fast event (maximum 0.14 Ma; Panfili et al., 2017). In such a scenario, CAMP would be responsible for negative carbon isotope shifts occurred in correspondence with ETE. In fact, following Panfili et al. (2017) Moroccan basalts emplaced between the Marshi and Spalae CIEs (sensu Lindström et al., 2017). Moreover, the negative CIE below Lower basalts was interpreted by Dal Corso et al. (2014) to be correspondent to the precursor negative carbon isotope shift identified by Ruhl and Kürschner (2011). Dal Corso et al. (2014) suggested that this negative precursor carbon isotope shift could be due to emplacement of basalts now eroded. This hypothesis seems to be strengthened by what argued by Lindström et al. (2017), according to whom CAMP basalts pre-date or are synchronous with the Marshi CIE, and might be the main cause triggering the mass extinction event. Davies et al. (2017) and Ruhl and Kürschner (2011) proposed a thermogenic origin for the precursor excursion. The thermogenic gas hypothesis (Svensen et al., 2004) would seem to be more accredited also for the Tr-J boundary mass extinction, and sill intrusions would play a more important role than originally thought.

2 Thermal metamorphism

As previously discussed in the first chapter, LIPs are usually associated with the presence of sills and dykes emplaced in sedimentary rocks. An important consequence of their emplacement is a rapid heating of the host sedimentary rocks, leading to devolatilization reactions of organic matter and hydrous minerals (Aarnes et al., 2011b;). Data obtained from modeling or from field activity demonstrate that large amounts of CH_4 and CO_2 were produced during these events and then released into the atmosphere (Aarnes et al., 2012; Aarnes et al., 2011a, 2011b; Aarnes et al., 2010; Iyer et al., 2017a; Stordal et al., 2017; Svensen et al., 2015; Svensen and Jamtveit 2010; Svensen et al., 2004). Negative carbon isotope excursions, verified in a temporal period close to these important magmatic activity, can be explained by a rapid and important release of ^{12}C enriched gases, such as the previously mentioned CH_4 and CO_2 (Dal Corso et al., 2014; Davies et al., 2017; Panfili et al., 2017; Ruhl and Kürschner, 2011; Svensen et al., 2004).

2.1 The thermal metamorphism theory

The thermal metamorphism theory has been developed only in the last decades. Particularly, Svensen et al. (2004) suggested that sub-volcanic parts of LIPs, i.e. dykes or sills, may give rise to a strong interaction with organic-rich sedimentary strata. This hypothesis was of great importance and opened a new path to understanding the climatic and environmental consequences of LIPs. The theory proposed by Svensen et al. (2004) can be summed up in the following points (Svensen et al., 2015):

- Sill emplacement into sedimentary rocks leads to a temperature increase into sedimentary rocks, with a series of reactions (devolatilization reactions), that will affect both minerals and organic matter;
- The contact aureole thickness is variable and depends on sill thickness and the distance between two (or more) sills;
- Greenhouse gases (CH_4 and CO_2) are produced by heated organic matter rich sediments. Such sediments have also a ^{12}C-enriched isotopic signature. For instance, thermogenic methane, produced by organic material into contact aureole, presents a carbon isotopic ratio value included between -35‰ and -50‰;
- Degassing to the atmosphere happens following the release of overpressure. It occurs during formation of both breccia pipes and hydrothermal vent complexes, or during a long-term seepage;
- Not all rocks produce the same type of gas. Carbon gases are produced by organic matter present in siltstones/sandstones and limestone. Instead, gases produced by magma-evaporite interaction give origin to sulfur- and halogen-bearing gases. The gases' climatic and environmental effects are very different;
- According to what has just been mentioned above, the climatic and environmental effects of sill/s intrusions depend on the type of sedimentary rocks in which the intrusions take place.

Svensen et al. (2004) also affirmed that a certain volume of melt intruded into sedimentary rocks might produce a higher carbon flux to the atmosphere than a similar volume of erupted magma. In fact, they estimated that the amount of carbon-bearing gas released by one cubic meter of CO_2-satured basaltic melt is about 3.6 kg; a melt intruded into organic-rich mudstones might produce a quantity of carbon per cubic meter of magma equal to 25-100 kg. Accordingly, the carbon flux, directed towards the atmosphere, would be more than an order of magnitude bigger in the case in which magma was intruded into sediments relatively rich in organic matter, rather than if the magma was thrown out and degassed to the surface (Svensen et al., 2004).

2.2 Contact metamorphism of organic and inorganic material

In contact aureole many consequences of igneous intrusions can be observed. First of all, traces of maturation of organic material are found. So, elevated vitrinite reflectance values (%Ro), loss of T.O.C., changes in carbon isotope composition ($\delta^{13}C$) and an increased aromatization are visible (Aarnes et al., 2010): it is possible to deduce that organic matter is very sensitive to thermal alterations. Normally, T.O.C. values will decrease symmetrically towards the intrusion contacts (Senger et al., 2014). In the case of Rock-Eval parameters, it is possible to observe a trend similar to that of the T.O.C., especially in the case of the Hydrogen Index parameter (HI) and the S2 peak values. Their values will decrease symmetrically, progressively approaching the sill (Senger et al., 2014). Nearing to the sill, it is also possible to observe a change in $\delta^{13}C$ values. In fact, a small fractionation in $\delta^{13}C$ to heavier values in the organic matter is evident in most of the cases (Barker et al., 1998; Senger et al., 2014). This suggest that isotopically light carbon was removed by sill intrusion from the contact aureole. Note that this $\delta^{13}C$ values trend is common in contact metamorphism sedimentary rocks, but the degree of fractionation does not depend on the sill thickness (Senger et al., 2014). Lastly, vitrinite reflectance values generally will increase towards the sill contacts. If the normal vitrinite reflectance trend is not visible, this could be due to the action of metamorphic fluids or hot fluids into the metamorphic aureole (Barker et al., 1998).

The distances at which organic matter is sufficiently altered to be included into gas or oil windows are generally expressed as percentage of dyke thickness (Muirhead et al., 2017). Note that the thermal alteration of organic matter also occurs at lower temperatures and with more elevated reaction rates than the thermal alteration interesting the inorganic bulk rock in which mineral reactions happen. This implies that the metamorphic aureole effects on organic matter are more extensive than the aureole where metamorphic minerals are formed (Muirhead et al., 2017). So, aureole thickness will vary significantly in relation to the parameters used (T.O.C., mineralogy, vitrinite reflectance, organic geochemistry, gas chromatography; Muirhead et al., 2017; Senger et al., 2014). In the case of a contact aureole based on vitrinite reflectance values, it can be divided into two parts: the inner part (close to the sill) shows vitrinite reflectance values > 1.5 %Ro and corresponds to the metagenetic stage, where secondary cracking of oil to gas occurs, and gas is the only product; the outer portion exhibits vitrinite reflectance values ranging between 0.5 %Ro and 1.5 %Ro and is the zone in which both oil and gas generates. For vitrinite values < 0.5 %Ro no hydrocarbons production occurs (Aarnes et al., 2010; Aarnes et al., 2011b; Fig. 2.1).

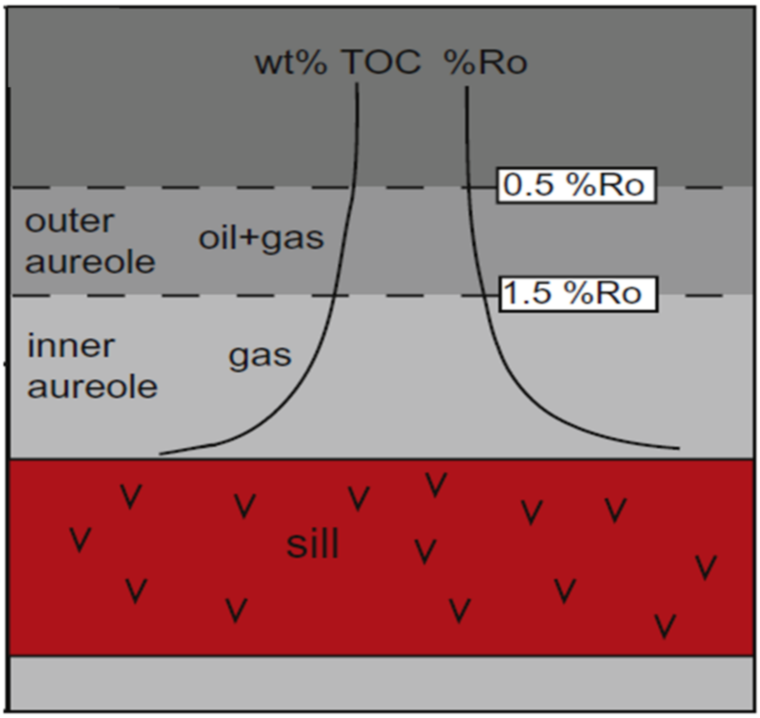

Fig. 2.1 Schematic contact aureole based on vitrinite reflectance values (%Ro; modified from Aarnes et al., 2010).

The contact metamorphic effects on the organic matter depend on several factors, among which appear intrusion thickness and temperatures of the intrusion, thermal gradient and emplacement depth, emplacement history, host rocks characteristics (depth, thermal conductivity, porosity, permeability, heat capacity…) and the cooling regime (Muirhead et al., 2017; Senger et al., 2014). Contact metamorphic processes, such as the release of pore water, degassing from organic matter or release of mineral-bound H_2O or CO_2, act on the source rock accelerating hydrocarbon maturation. In fact, in areas immediately close to intrusion, there is a general rock overmaturation, causing the overcooking of the source rocks (Senger et al., 2017; Senger et al., 2014).

Contact metamorphic processes in a context of large pluton intrusions are well documented. In these circumstances mineral dehydration and decarbonation reactions and host-rock melting reactions occur. In situations as sill or dike intrusions (or generically sheet intrusions) into sedimentary host-rocks, mineral reactions are comparatively less documented (Aarnes et al., 2010). There are some important differences between the two situations. First of all, the magma and the host rocks have different temperatures: shallow sedimentary host rocks show a maximum temperature much smaller compared to the rocks in the deeper crust; granitic magmas, that form plutons, have a lower temperature than basaltic magmas, which forms sills or dikes. So, in the case of a sheet intrusion, a very fast cooling happens due to the strong temperature contrast between magma and host sediment. Therefore, the available heat for metamorphic reactions is much lower (Aarnes et al., 2010). Therefore, contact aureoles around sills are relatively small.

Examples of contact metamorphic effects on the surrounding rocks can be the formation or the breakdown of some minerals (biotite, muscovite...) in relation to the temperature, the devolatilization and decarbonation reactions or even the melting of host rock (Aarnes et al., 2010; Holness et al., 2005). Holness et al. (2005) showed how in the case of a shallow sheet intrusion within fine grained sedimentary rocks, the sediments may undergo incipient melting as testified by microscopic melt rims around the minerals. Holness et al., (2005) noticed furthermore that melt rims become thicker towards the contact. Note that in the case of small contact aureoles, the relatively short duration of the metamorphic phenomenon, together with the static nature of the event, the textures developed at the metamorphic peak may be well preserved (Holness et al., 2005).

Other effects of contact metamorphism on the host rock are, for instance, the loss of porosity and the increase in rock density.

2.3 Organic matter and gas generation

2.3.1 Gases as product of contact metamorphism

As previously said, not all the types of rocks give origin to the same gas as rocks heating due to the metamorphism. In limestones, for instance, the main produced fluid is water (H_2O), with a limited production of CH_4 and CO_2 (Aarnes et al., 2011b). The main fluid produced by dolostones is ^{13}C-enriched CO_2; only if organic matter or graphite are present, the fluid will contain ^{13}C-depleted CH_4 (Svensen et Jamtveit, 2010). In the case of evaporites, the principal products are SO_2 or HCl (hydrochloric acid; Svensen et Jamtveit, 2010; Svensen et al., 2004). Particularly, if reactive organic matter or petroleum are present in evaporites, the generation of CH_4 and CH_3Cl (chloromethane, that may contribute to the ozone depletion once emitted into the atmosphere) will occur (Aarnes et al., 2011b; Svensen et Jamtveit, 2010; Svensen et al., 2009b). In some cases, CH_3Br (bromomethane) and other types of halocarbons can also be originated from evaporites (Aarnes et al., 2011b; Svensen et al., 2009b). Carbon-based gases are produced by heating organic-rich sedimentary rocks (as siltstones, sandstones, mudstones, shales; Svensen et al., 2004). Moreover, it is commonly shown by phase equilibria calculation that clay-rich lithologies, composed mainly of hydrous minerals and only by a small percentages of carbonates, can produce large amounts of CO_2 (Aarnes et al, 2011b; Kerrick and Connolly, 2001). In fact, it seems that high H_2O content in the bulk rock (or infiltration of external hot fluids) would increase CO_2 generation from decarbonation (Aarnes et al, 2011b). Lastly, because of the presence of oil and gas accumulations in many sedimentary basins at the time of sill emplacement, petroleum-derived gases, such as CH_4 or C_2H_6 (ethane) may have been the dominant metamorphic fluids produced (Svensen and Jamtveit, 2010; Svensen et al., 2009b).

2.3.2 The organic matter and its gaseous products

The composition of organic matter, contained in the wall-rocks, can be approximated as $n(CH_{2n}O)$, as organic matter consists not only of Carbon (C), yet also of Hydrogen (H) and Oxygen (O).

With the increase of temperature and/or burial, the organic matter structure becomes more and more complex. So, organic matters turn into kerogen during diagenesis, a phase that occurs under ambient temperature and ambient pressure and includes both microbial degradation and abiotic transformations. There are different types of kerogen based on the different properties characterizing the original organic matter (Fig. 2.2):

- Type I kerogen is relatively rare and initially has a high H/C ratio (≥ 1.5) and a low O/C ratio (< 0.1; Fig. 2.2). Lipids are the main compound, especially long-chain aliphatics. It derives essentially from algae, although organic matter of bacterial origin can contribute to its formation. If compared to the other types of kerogen, kerogen I contains low amounts of aromatic units and heteroatoms. Kerogen type I is generally associated to lacustrine sediments (Killops and Killops, 2005);
- Type II kerogen is more common than type I and has a relatively high H/C ratio while O/C ratio is still low (Fig. 2.2). It derives from algae but it may also contain zooplankton and phytoplankton. Its composition might have a further contribution of plant material. This would make kerogen II a mixture with midway characteristics among kerogen type I and kerogen

type III. Aliphatic structures are important and constitute abundant chains (Killops and Killops, 2005);

- Type III kerogen is very common. It has a very low H/C ratio (< 1.0) and a high O/C ratio (up to 0.3; Fig. 2.2). In kerogen type III there is a low amount of aliphatic structures, whereas it is characterized by a great quantity in aromatic compounds. It is produced by the lignin of the woody plants, that grow on land. Vitrinite macerals predominate in kerogen III. Aliclyclic structures are very abundant (Killops and Killops, 2005).

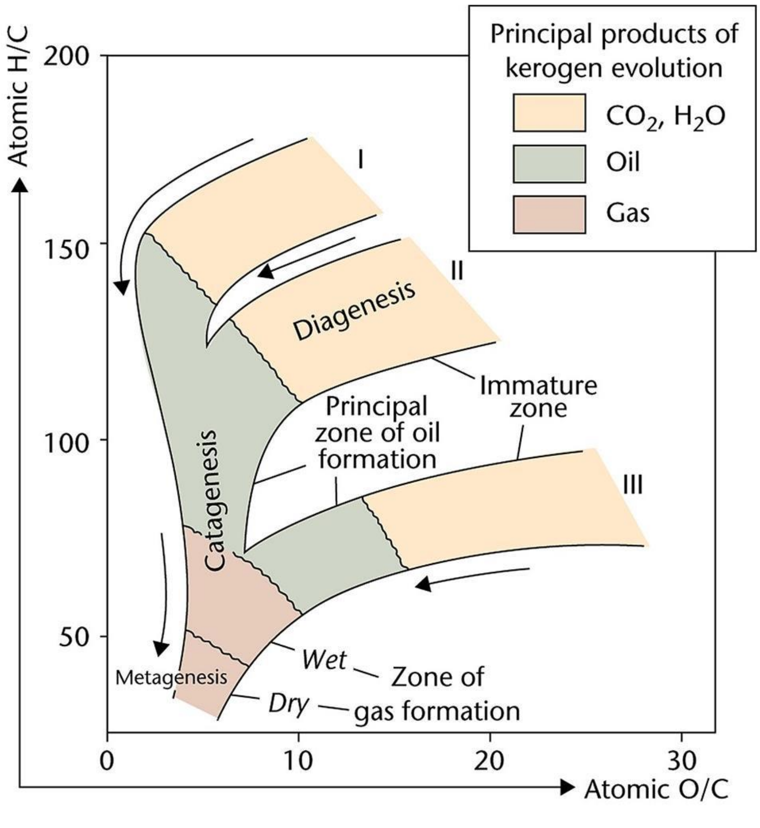

Fig. 2.2 Graphic representation of the main kerogen types. Their principal characteristics and products are also showed (from Allen and Allen, 2014).

In addition to the type of kerogen mentioned above, there is another type of kerogen called Type IV kerogen. This type of kerogen is of secondary importance because it has no hydrocarbon-generating potential.

As for the three main types of kerogen, they do not give rise to the same type of hydrocarbon. At increasing temperature, kerogen will first meet the “oil window”, within which oil generation occurs (100-150°C), and only then will reach the “gas window”, a temperature range within gas formation occurs (150-230°C) (Killops and Killops, 2005). Based on the type of original organic matter, any kind of kerogen will have a preference for producing gas or oil. Kerogen I shows a preference to produce oil; type II kerogen, even if contains fewer aliphatic units than kerogen I, is still capable to produce large amounts of oil. Kerogen III, in which aliphatic units are present as small chains whereas alicyclic structures constitute important compounds, produce a large quantity of gas and a very small quantity of crude oil (Killops and Killops, 2005).

Depending on the type of organic matter and temperature, the heated rocks generate CO_2 (if they contain continental origin organic matter) or CH_4 (if organic matter of marine origin is present inside the rocks; Svensen et al., 2017). In fact, once the appropriate temperatures for the gas formation have been reached, kerogen type I and II (commonly found in marine shales), generate hydrocarbon fluids as CH_4, because of their high hydrogen content (and low oxygen content). By contrast, type III kerogen (generally present in humic coals or poor source rocks), characterized by a high O/C ratio, a low H/C ratio and, so, a high oxygen content, produce CO_2 as main gas (Aarnes et al., 2011a, 2011b).

As proposed i.e. by Svensen et al., (2015), gas production may take place following the formula:

$$2CH_2O = CH_4 + CO_2$$

where CH_2O is an approximation of the organic matter composition and CH_4 and CO_2 are the produced gases. The quantity of gas produced depends also on the nature of the organic matter. Humic coals are mainly composed by kerogen III, from which only the 10-25% of organic matter can be converted into gas (Aarnes et al., 2010; Hunt, 1996). Instead in the case of type I kerogen or type II kerogen, they have a bigger potential of producing hydrocarbons (up to 95% of T.O.C. is converted into hydrocarbon) (Aarnes et al., 2010; Ungerer and Pelet, 1987).

Different productions of carbon-bearing gases produce also a different impact on the atmosphere. In fact, contact metamorphism in coal affects atmospheric carbon isotope values less than contact metamorphism in shales because CO_2 has a more positive $\delta^{13}C$ values in coals. Furthermore, it has also to be remembered that gas production from coal takes more time than gas production from shales (it depends on reaction timescales, influenced by heat transfer) and that gas amount produced by coal is nearly equivalent to half the gas amount produced by shales (Aarnes et al., 2011b). Specially, the most productive lithology is represented by organic matter rich shale: from modeling, it seems to produce the highest quantity of CH_4 (Aarnes et al., 2011b).

2.4 The effect of a single sill and multiple sill intrusions on gases formation.

In several previous studies, the attempt to quantify the influence of sill intrusions has been made. Specially, the importance of multiple sills emplacement into sedimentary basins have been investigated (Aarnes et al., 2011a).

Aarnes et al., (2011a) considered different study cases in order to determine if there are any significant differences between the intrusion of a small sill or a big sill and multiple sill emplacements. They used a one dimension model in Matlab to do this type of study. First of all, they assumed that sill thickness and host-rock lithology remain unchanged during time, so the volume of hydrocarbons generated is a function of the sill size.

On the base of their model, in the case of a sill with an area of 50 by 50 km, the hydrocarbons amount released should be equal to 4.3 gigatons (Gt) of CH_4 (Fig. 2.3). Then it is possible to observe that one single thin sill, intruded into an organic-rich formation, can generate several gigatons of greenhouse gases depending on the sill’ s lateral extent.

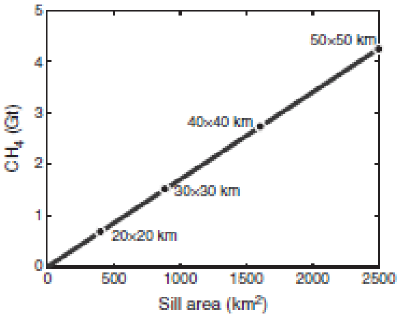

Fig. 2.3 Representation of the CH_4 amount released into the atmosphere on the base of sill area (from Aarnes et al., 2011a).

They studied several cases to understand how multiple sills intrusion can influence hydrocarbons production and if the distance between two (or more) sills is an important factor affecting gases production. They examined, for example, the situation in which two sills of 15 meter thickness emplace instantaneously with a vertical distance of about seven times their thickness (110 m). After 150 1D-model runs, they could assert that the 15 meters thick sills, emplaced at the same time, induce larger organic maturation and gas generation than two sills intruded at larger distances. Obviously, the interaction between the two sills will be greater if sills are closer one to each other. Furthermore, from several 1D model results, they obtained that there is an ideal vertical distance for yielding the maximum gas generation. In the case of two sills with a thickness of 15.5 m, the vertical spacing is about four times the sills thickness (60 m): in this case the total generation of gases is larger by 35% than the amount of gases released by two separate sills. After passing the vertical distance of 60 m between the sills, a decrease in gas production has been noticed in relation to the decrease of rocks volumes affected by thermal metamorphism (Fig. 2.4).

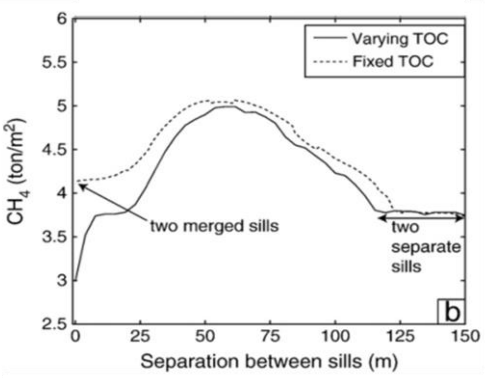

Fig. 2.4 Schematic representation of the amount of CH_4 released in the different cases of two merged sill and two separate sills. Note that in the case of two separate sills there is a specific distance, linked to their thickness (in this case 15.5 m), at which a maximum production of carbon-bearing gases occurs (from Aarnes et al., 2011a).

Similar observation have also been made for other sills thicknesses. For example, two sills characterized by a thickness of nearly 100 m have been considered. In this case, thermal interaction occurs within an ideal spacing of about ten times the sill thicknesses, with a maximum peak of hydrocarbons production at five sill thicknesses. The total gas generation is ~30% higher compared to that produced by two separate sills.

Another important result of the modeling performed by Aarnes et al. (2010) is that in some cases (they considered five sills of variable thickness intruded into the Ecca Group in the Karoo Basin) the hydrocarbon production affects the entire sedimentary basin and not only the metamorphic aureoles. Particularly, they have observed that multiple sill intrusions result in an elevated background thermal maturation and large scale gas production. In basins affected by volcanism, the background temperature remains particularly high for thousands of years leading favorable conditions for hydrocarbon production. This is due to the fact that higher background conditions require a smaller quantity of heat to cause kerogen breakdown. As a result of this intense magmatic activity, the thermal maturity of organic matter will be altered for several hundred meters from intrusions, gas production will occur inside all the volcanic basin and it will be greater than the quantity that can be estimated by assuming a single intrusion.

All these elements allow us to understand how many factors could have influenced gas production as a consequence of sill intrusions and how the numerical modeling can be complex in this type of study. Applying such findings to the case of the end-Triassic mass extinction, we can deduce that multiple sill intrusions within the Brazilian basins (Amazonas and Solimões basins) may have been a particularly effective source of green-house gases, more than basins (e.g. Morocco) where only single intrusions occurred (Davies et al., 2017).

2.5 Hydrothermal venting and breccia pipes: how gases escape to atmosphere

It is supposed that the fate of the gases produced as a result of magmatic intrusions can be of different nature. They can be partly trapped into sedimentary successions, lost to the surface by seepage because of the presence of fractures or they can also be injected into the atmosphere through explosion pipes (Iyer et al., 2017a; Stordal et al., 2017; Svensen and Jamtveit, 2010; Svensen et al., 2009a; Svensen et al., 2007). In many volcanic basins, there is evidence for rapid emissions of the aureole-generated gases into the atmosphere. In fact, when a sill intrudes a sedimentary succession, a series of changes and events happen (e.g. over organic matter decomposition and mineral reactions, pore fluid expansion or boiling) that result in a general overpressure within the sedimentary strata (Svensen and Jamtveit, 2010). The resulting overpressure cause the formation of breccia pipes and hydrothermal vent complexes (Jamtveit et al., 2004). Breccia pipes (sub-vertical cylindrical structures that cut sedimentary strata; Svensen et al., 2007; Fig. 2.5) are visible in many magmatic provinces, commonly associated to extinction events (i.e. Karoo Basin and Karoo-Ferrar LIP; Tunguska Basin and

Siberian Traps; Vøring and Møre Basin and Northeast Atlantic Igneous Province; Svensen and Jamtveit, 2010).

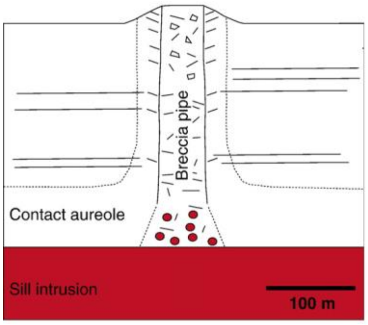

Fig. 2.5 Schematic cross section of a breccia pipe (modified from Svensen et al., 2007).

Vent structures are also characteristic features of volcanic basins as Vøring and Møre Basin, the Faroe-Shetland Basin and the Tanguska Basin (Svensen and Jamtveit, 2010; Svensen et al., 2009a; Fig. 2.6).

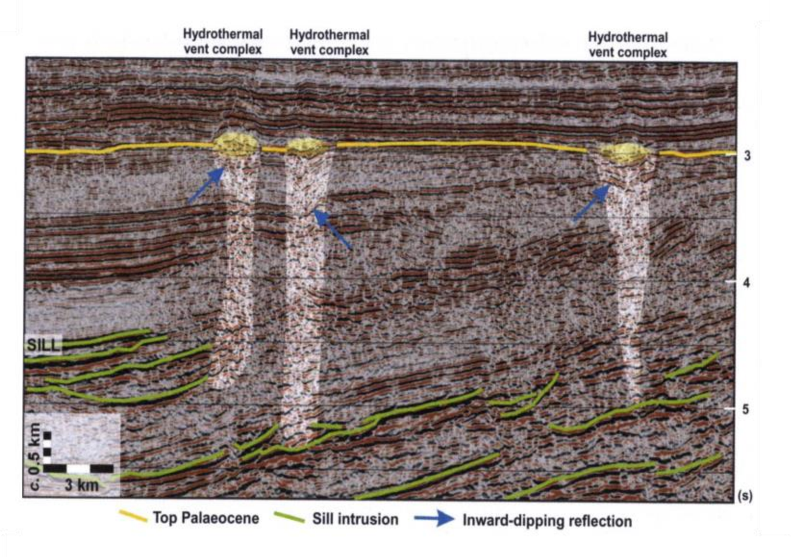

Fig. 2.6 Seismic profile from the Vøring and Møre basin,Norway. It is possible to observe the presence of hydrothermal venting complexes developed on kilometric scale (from Jamtveit et al., 2004).

Permeability is a key parameter for the control of the fluid flow efficiency and so it has a major control on the magnitude of overpressure. Particularly, unfractured shales, siliceous carbonates and crystalline rocks have a very low permeability. So, because of the permeability, a large overpressure occurs in these types of systems (Aarnes et al., 2012; Svensen et al., 2007).

No traces of the presence of breccia pipes or venting structures have been found in relation to CAMP (Svensen and Jamtveit, 2010). This leads to think that degassing may have occurred from the presence of pre-existing fractures or due to the deformation of host rocks induced the emplacement of the sills (i.e. Delaney et al., 1986). It should also be stressed how difficult it is to trace these types of structure in vast and vegetation-rich areas, as the Amazonian Basins.

3 Samples’ geographic origin: basins stratigraphy and formation

In this study, three sequences of samples have been considered. Each of the three sequences located in sedimentary basins affected by CAMP magmatism (~ 201.5 Ma). The sedimentary basins are: the Amazonas basin in Brazil, the Arganà Valley in Morocco and the Newark basin in the U.S.A.. Particularly, two of the three considered basins, namely the Arganà Valley basin and the Newark basin, developed during the end-Triassic breakup of the Pangea.

3.1 The Central Atlantic Margin basins and the rifting of Pangea

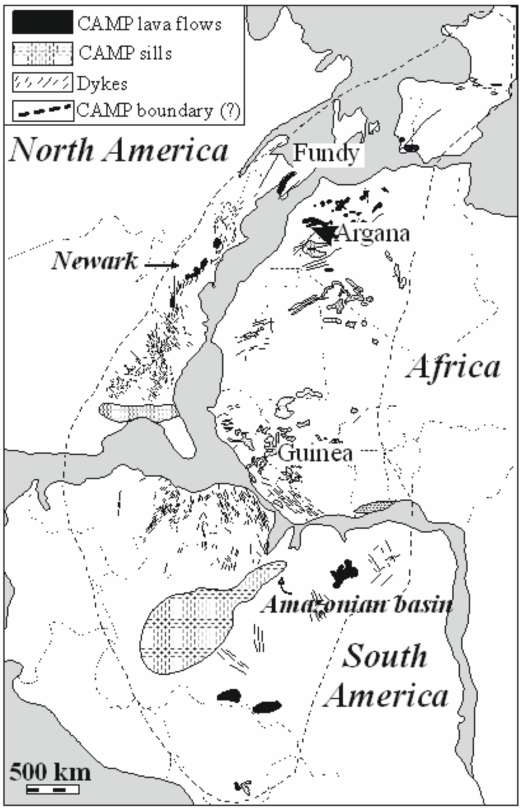

Fig. 3.1 The Central Atlantic magmatic province in a ca. 201 Ma reconstruction of Pangea. The CAM principal basins and the Amazonian basins are shown (modified after Marzoli et al., 2011).

The CAM (Central Atlantic Margin; Fig. 3.1) basins are the result of the incipient rifting of the Pangea, due to diverging movements of the North American and African plates, and represent a stratigraphic record generally comprised between the Late Triassic and the Early Jurassic (Olsen, 1997). Some of the most famous of the CAM basins are located in eastern U.S.A. and Canada (Olsen, 1997; Olsen et al., 1996; Schlische and Anders, 1996; Fig. 3.1). CAM basins are represented by half graben complexes. The basins are delimited by a major normal fault system, in the direction of which basin strata tilt (Olsen, 1997; Fig. 3.2). Synsedimentary half graben development is evidenced by the following observation, made with the integration of multiple studies: 1. decrease of the dip of the strata by moving topwards (i.e. observable through the drill holes); 2. fanning of strata toward the border fault system (observed thanks to seismic profiles); 3. thickening of the layers towards the border faults (as observed from continuous cores and outcrops); 4. evidence from the results of paleocurrent and sediment provenance studies (Olsen, 1997).
All of the CAM basins have sequences that show strong vertical changes in facies, reflecting large-scale tectonic and climatic changes during the time. Particularly, basin sections are made up of one or more tripartite sequences consisting of a lower coarse-grained fluvial facies, followed by a transition upward into shallower-water facies and even coarse fluvial facies (Olsen, 1997). This kind of vertical sequences has been explained in several ways: 1. it was interpreted as the result of the specific succession of the tectonic events that affected the basins; 2. it was suggested that these sequences are a consequence of the sequential filling of hydrographically linked basins; 3. it was also explained as the result of the filling of a widening half graben basin bounded by a normal fault (Olsen, 1997). Note that, besides multiple tripartite sequences, fluvial sequences delimited by unconformity have been observed in many CAM basins.

Furthermore, studies conducted over the last decades have demonstrated that four basic tectonostratigraphic sequences (defined as TS I, TS II, TS III and TS IV and visible in Fig. 3.2) can be observed in most of the CAM basins. These sequences have been defined on stratigraphic base, are generally, even if not in all cases, bounded by unconformities and probably result from significant changes in the rate of extension (Olsen, 1997). TS I is represented by initial synrift sedimentary rocks of possible Anisian age; TS II, instead, consists of early synrift sedimentary rocks of possible Ladinian to Carnian age; TS III represents rocks of middle synrift phase with a Late Triassic age; lastly, TS IV consist of late synrift sedimentary and volcanic rocks of Late Triassic to Hettangian age, with the addition of the overlying sedimentary rocks belonging to the late synrift phase (from Hettangian to, in some cases, Pliensbachian age; Olsen, 1997).

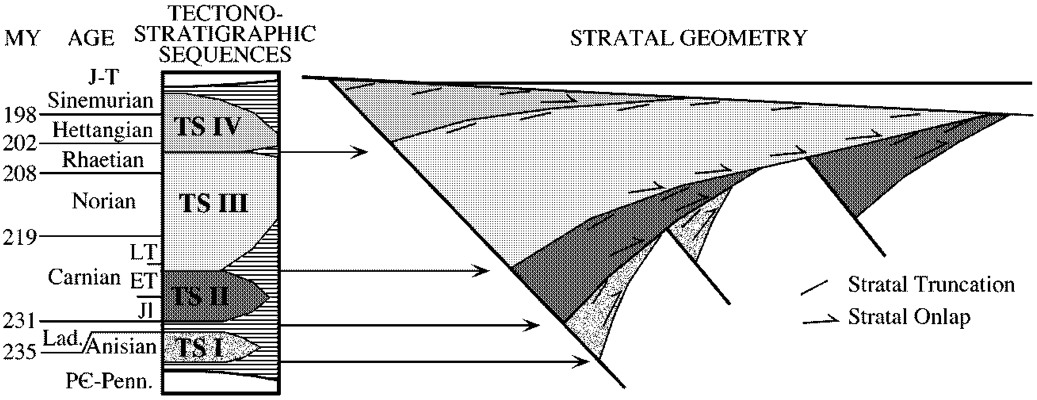

Fig. 3.2 In the figure a simplification, based primarily on seismic profiles and coring, of the CAM basins is reported. It is possible to observe their tectonostratigraphic sequences (TS I, TS II, TS III and TS IV with their relative ages) and the presence of a normal fault system, delimiting the basins (from Olsen, 1997).

TS I has been identified only in the Fundy basin and in the Arganà basin. This sequence is delimited both below and above by two unconformities, that separate it from the older prerift rocks and the younger synrift strata. TS I, generally, consists mostly of fluvial and aeolian rocks deposited under an arid environment (Olsen, 1997). Traces of this tectonostratigraphic sequence are present in the Fundy Basin or in the Arganà Basin, where it is termed as Ikakern formation (Olsen, 1997).

The sequence TS II shows typical characteristics of a more humid depositional environment than the previous TS I sequence or the following TS III one. It is

delimited below by an angular unconformity. In some cases it is also possible to observe an angular unconformity in its upper portion (Olsen, 1997).
TS II is present in several CAM basins; for example TS II can be found in the Arganà Valley, where it is named Timezgadiwine Formation (Olsen, 1997).

TS III is the most widespread sequence within the CAM basins. In some basins this tectonostratigraphic sequence is represented only by fluvial sediments. Instead, in the other cases TS III consists of a thick basal fluvial interval, followed upwards by a thicker lacustrine sequence.
The TS III sequence is well represented in the Newark Basin and is represented by the Stockton Formation, the Lockatong Formation and the Passaic Formation. In the Arganà valley the TS III is constituted by the Bigoudine Formation (Olsen, 1997).

The TS IV sequence comprises the tholeiitic lava flows of the CAMP and the Triassic-Jurassic boundary.
It is thought that during the deposition of this sedimentary sequence an increase in the subsidence rate occurred. It can not be ruled out that unconformities can be found at the top of this tectonostratigraphic sequence or within it: in fact, for example, some traces of erosion have been found in the Hartford basin (Olsen, 1990). TS IV can be well observed in the Hartford Basin, where there is its type area, in the Newark Basin, in which TS IV start within the uppermost portion of the Passaic Formation, and in the Arganà Valley, where comprises the uppermost Bigoudine formation and the overlying sedimentary units (Olsen, 1990).

3.1.1 The Arganà Valley

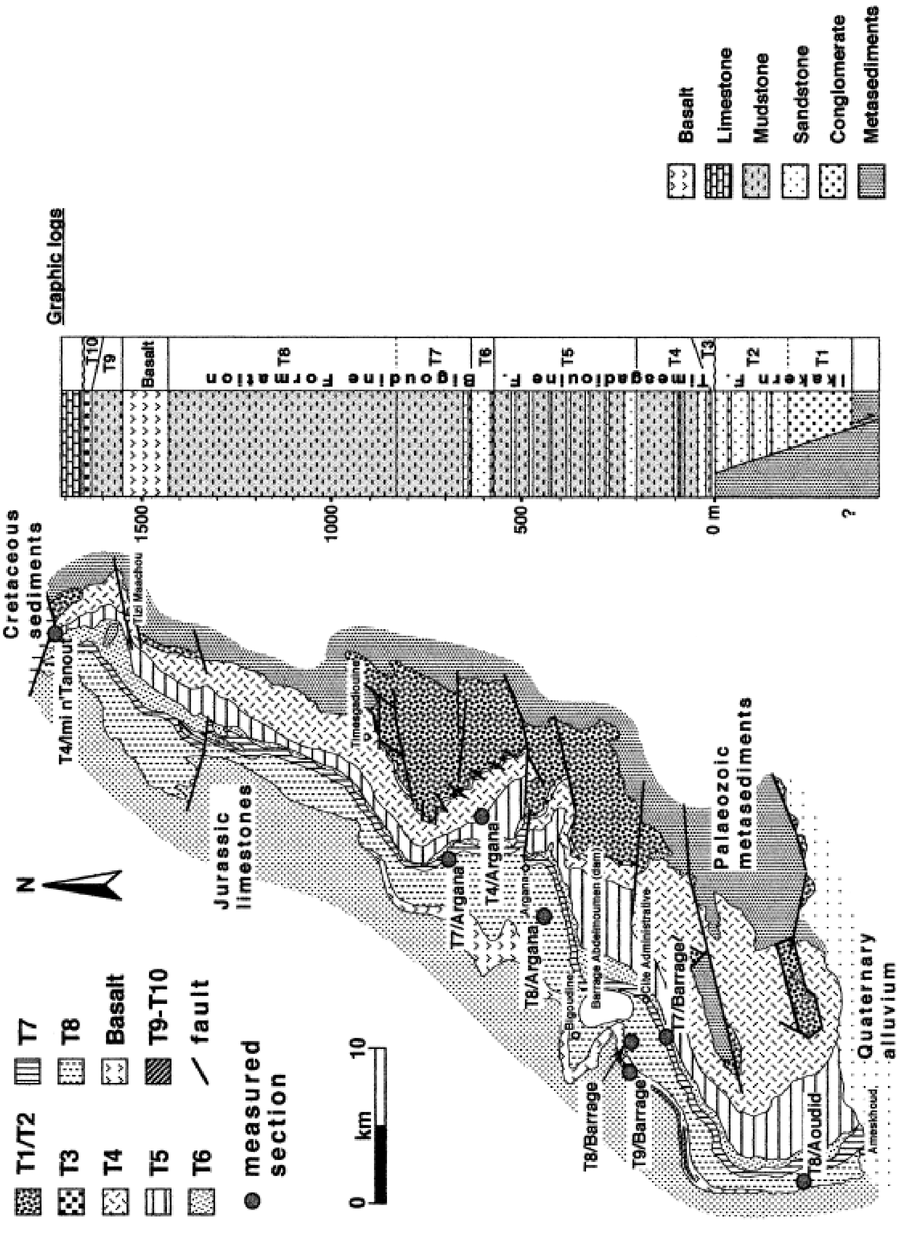

Fig. 3.3 In the figure are shown a geological map of the Arganà Valley and a complete simplified log illustrating the lithostratigraphy of the valley. In the log, besides formations name, the acronyms for each member constituting the various formation are reported. Note that in the log, the name of the Ameskround Fm. (T9-T10) and the limestone are missing. In the map, as visible from the legend, the extension and the position of the individual members, with the exception of the Jurassic Limestone, is reported (modified by Hoffman et al., 2000).

The Arganà Basin (Fig. 3.3) is one of the CAM basins, developed during the end-Triassic breakup of the Pangea. It is located between Agadir and Marrakesh, along the western side of High Atlas chain, and is constituted primarly by continental red beds, that gain a thickness of more than 1600 m (Hoffman et al., 2000). The red beds are represented by a vertical succession of alluvial, fluvial, aeolian and playa deposits (Hoffman et al., 2000). Particularly, in the Arganà Basin it is possible to observe the presence of several sedimentary cycles, that, commonly, comprise ephemeral lake shales at the base, playa mudflat mudstones in the intermediate portion and aeolian and fluvial sandstones in the cycles upper portion. It is thought that this cyclicity is linked to some Milankovitch cycles and is therefore considered to be the result of paleoclimatic changes and palaeohydrological fluctuations associated with them (Hoffman et al., 2000). The long-term paleoclimatic changes are visible by comparing the different formation present in the basin (Hoffman et al., 2000; Olsen, 1997). For instance, previous studies (Smoot, 1991) showed the presence of evaporite molds, nodules, crystal of gypsum and halite and other very soluble salts within the Bigoudine Formation. So, Bigoudine Formation appears to have formed under a more arid climate if compared, for example, with the underlying Timezgadiwine Formation, deposited under humid conditions (Olsen, 1997). A similar cyclicity have also been observed in the Newark Supergroup basins (Hoffman et al., 2000; Olsen, 1997).

Stratigraphically, in the Arganà Basin it is possible to observe three main formations, the Ikakern Fm., the Timezgadiwine Fm. And the Bigoudine Fm., further subdivided in eight litostratigraphic units, and overlaid by the CAMP tholeiitic basalts (Hoffman et al., 2000; Olsen, 1997; Fig. 3.3). Note that Ikakern Formation is separated from the metasediments by an unconformity; Timezgoudine Fm. also is devided from the underlying Ikakern Formation by an unconformity (Baudon and Redfern, 2011; Hoffman et al., 2000). Continuing upwards, above the CAMP basalts there is the Ameskround Fm., also subdivided in two members (Hoffman et al., 2000; Fig. 3.3).

At the top of the stratigraphic sequence there are marine Jurassic limestones (Hoffman et al., 2000; Fig. 3.3).

At the base of Ikakern, Timezgadiwine and Bigoudine formations, there are some conglomerates, that grade upwards into finer sediments (sandstones, siltstones, mudstones). The finer sediments of the upper portion can be interbedded or, as previously said, cyclically stacked (Hoffman et al., 2000).

The Ameskround Formation shows quartzitic conglomerates at its top. They are separated from the underlyng cyclically stacked mudstones, sandstones and siltstones by an erosive unconformity (Hoffman et al., 2000).

These formations show a low T.O.C., estimated to be generally minor than or equal to 0.5 % (note that all the T.O.C. data reported in this chapter and in the following chapter are expressed in percentage of weight; Sachse et al., 2016).

The samples used for our research have been taken from the upper portion of the Bigoudine formation. Particularly, they have been taken from the sedimentary sequence below the Amelal sill, which has a thickness of ~ 100 m and is outcropping in the southern portion of the Arganà Basin. The samples are red siltstones. Note that their color becomes darker approaching the sill (from red to dark red or violet).

3.1.2 The Newark Basin

Also developed during the rifting of the North American and the African plates at the time of the breakup of the Pangea, the Newark Basin (Fig. 3.4), covering ~ 7770 km^2 (Olsen et al., 1996; Steckler et al., 1993) and belonging to the Newark Supergroup, is characterized by one of the best example of cyclicity in lacustrine lithologies, evident at many thickness scale (Olsen, 1997). It is thought that the sedimentary cyclicity is primarly due to lake-level variations, following almost periodic Milankovian cycles governed by celestial mechanisms (Hoffman et al., 2000; Olsen, 1997).

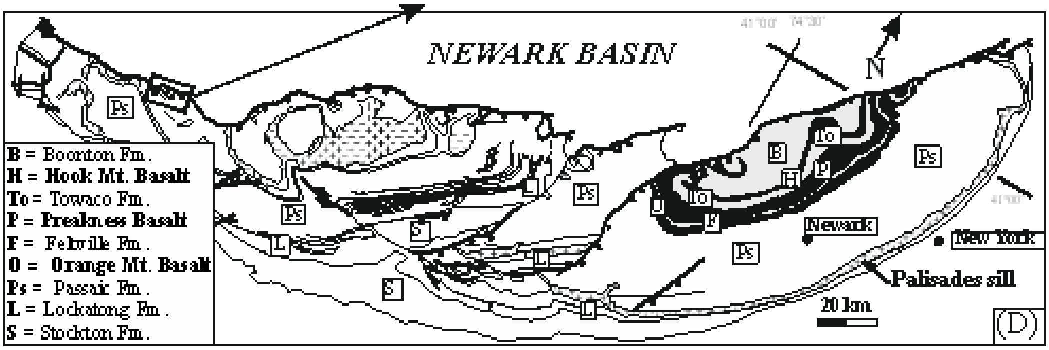

Fig. 3.4 Simplified geological map of the Newark basin showing its formations, its main faults, its perimeter and the Palisades sill (Marzoli et al., 2011).

The Newark Basin has a thickness of nearly 7 km, comprising more than 5 km of cyclical lacustrine rocks (Olsen, 1997; Olsen et al., 1996). The formations present and visible in the Newark Basin are the following (Fig. 3.4):

- Stockton Fm.: Stockton Formation, the basal formation of the Newark Basin, is dominated by fluvial sequences (Olsen, 1997; Olsen et al., 1996). It is constituted by gray and pebbly arkose, red sandstones and mudstones (Olsen et al., 1996; Olsen, 1997). It is possible to find some carbonate nodules in many mudstones; interclast conglomerates are abundant within the sandstones. Furthermore, sandstone and pebbly sandstone sequences, whom color is, generally, gray or white, are interbedded by gray mudstone (Olsen et al., 1996).

  Stockton Fm. show a thickness of about 1800 m (Olsen, 1997). The boundary between the Stockton and the overlying Locktong formations is based on the first occurrence of black or gray shale sequences (Olsen et al., 1996). Its average T.O.C. is nearly of 0.13% (Turner-Peterson et al., 1984);
- Lockatong Fm.: As previously said its base is determined by the first occurrence of gray or black shale sequences; instead its top has been localized where red beds start to predominate over the gray or black ones (Olsen et al., 1996). The basal portions of the Lockatong Fm. are generally sand-rich. Moving toward the middle portion of the formation, it is

possible to find a cyclical alternation between black shales and massive mudstone. Moving further upwards gray and black mudstones are found (Olsen et al., 1996). The Lockatong Formation, deposited in a lacustrine environment, as the following Passaic Formation, shows clearly a certain cyclicity, main feature of the Newark Basin and nearly absent in the Stockton Formation (Olsen, 1997; Olsen et al., 1996). This formation show an average T.O.C. of ~ 1.21% (Katz et al., 1988);

- Passaic Fm.: The base of Passaic Formation is defined as where red clastic rocks become dominant over black and gray ones. At its top is the Orange Mountain Basalt lava flow (Olsen et al., 1996).

  The Passaic Formation, originated in a lacustrine environment alternated with a fluvial one, is the thickest formation present in the Newark Basin (ca. 3300 m) and is also the most widespread formation (Olsen, 1997; Olsen et al., 1996). It shows a cyclicity similar to that of the Lockatong Formation and is composed by red, gray and black mudstone (Olsen, 1997). The average T.O.C. of Passaic Fm. is of ~ 1.22% (Katz et al., 1988);
- Feltivelle Fm.: the Feltville Formation is located above the Orange Mountain Basalt lava flow and below the Preakness Basalt lava flow (Olsen, 1997; Olsen et al., 1996). It is constituted by red, gray and purple sandstones and red mudstones, with subordinate amounts of cyclically repeated gray, black and purple mudstones (Olsen et al., 1996). The Feltville Fm. shows an average T.O.C. of ~ 2.37% (Katz et al., 1988);
- Towaco Formation: this formation is delimited below by Preakness Basalt and below by Hook Mountain Basalt (Olsen, 1997; Olsen et al., 1996). Both Towaco Formation and Boonton Formation are cyclical and show the same cyclicity of the underlying formations (Olsen et al., 1996). The Towaco Formation is very similar to the Feltville Formation, except for the presence of more fine grained sandstones and black calcareous laminated shales (Fedosh and Smoot, 1988). Towaco Fm. average T.O.C. is ca. 1.06% (Katz et al., 1988);

- Boonton Formation: located above the Hook Mountain Basalt, this formation consists of black laminated calcareous shales, that grades into gray siltstones, are distributed into the predominant red sandstones and mudstones (Fedosh and Smoot, 1988).

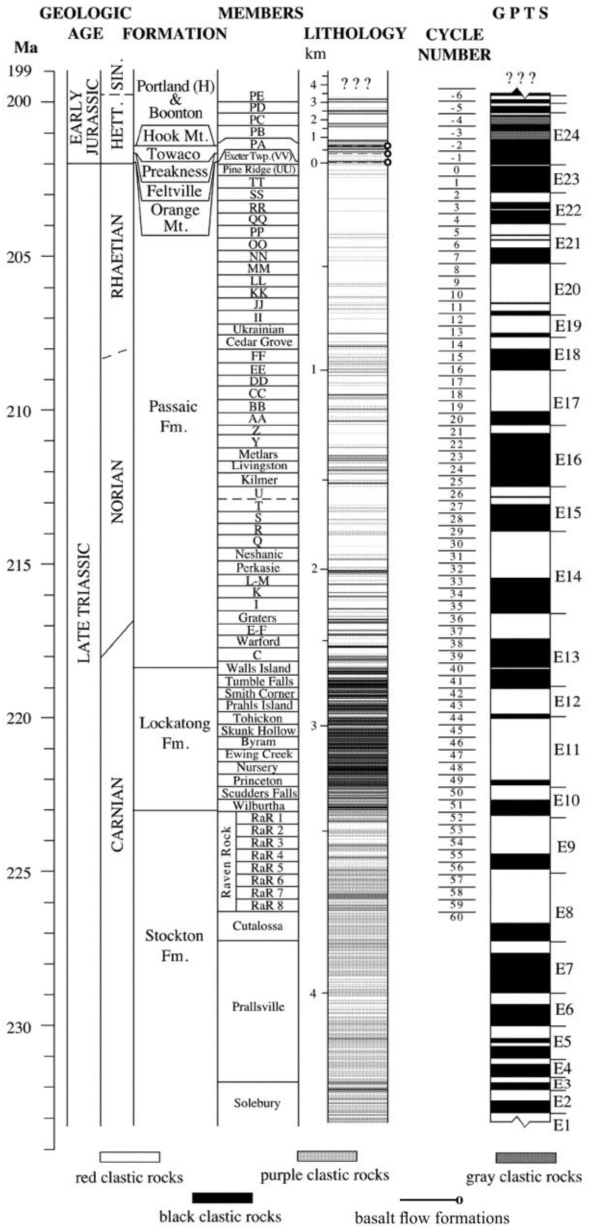

Fig. 3.5 Newark basin section stratigraphic nomenclature, with cyclostratigraphy, magnetostratigraphy and interpreted chronostratigraphy (from Olsen et al., 2002).

According to several authors (Roden and Miller, 1991; Steckler et al., 1993; Walters and Kotra, 1990; Withjack et al., 2013) after deposition there would be a basinal uplift, resulting in the erosion of nearly 2 km of sediments.

The samples considered for our study come from the Lockatong Formation. They are metamorphosed black shales and have been taken at different distances from the Palisades sill (~ 300 m; Van Houten, 1971), outcropping along the western side of the Hudson River and intruded within the Lockatong Formation. Note that Palisades sill gave origin to an unusual assemblage of contact metamorphic minerals characterized by sodium mineral associations (Van Houten, 1971).

3.2 The Amazonas Basin

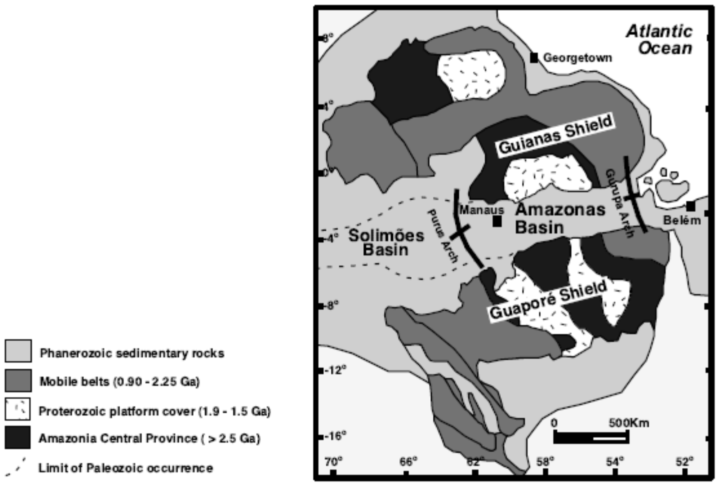

Fig. 3.6 Simplified map of the Amazonas basin, Brazil (modified from Gonzaga et al., 2000)

The Amazonas basin (Fig. 3.6) does not belong to the basins devoleped during the Pangea breakup (note that the breakup of Gondwana super-continent, with the movement of the current South America toward west and the current Africa

toward the east, occurred 140-130 Ma; Clemente, 2013). In fact, it does not appear in the list of the local basins considered to have formed during this geological event (i.e. Santos, Campos, Pelatos, Potiguar, etc; Cainelli and Mohriak, 1999; Clemente, 2013).
The Amazonas Basin is a 500,000 km^2 intracratonic basin located in northern Brazil, between the Guyana (to the north) and the Brazilian craton (to the south; Cunha et al., 2007; Gonzaga et al., 2000; Fig. 3.6). It is separated from the Marajò Basin by the Gurupà arch on the east and from Solimões Basin by the Purus arch on the west (Cunha et al., 2007; Gonzaga et al., 2000). The basin's sedimentary fill is about 6 km thick and consists chiefly of Paleozoic rocks intruded by late Triassic-early Jurassic sills and dikes, and covered and buried by Cretaceous-Tertiary rocks (Gonzaga et al., 2000).

The sedimentary record of the Amazonas Basin can be divided into two transgressive and regressive megasequences: a Paleozoic one, that can be divide into three second order sequences (the Ordovician-Devonian sequence; the Devonian-Tournasian and the Pensilvanian-Permian sequence), and a Cretaceous-Tertiary one (Cunha et al., 2007; Gonzaga et al., 2000). All the Paleozoic sequences are bounded by unconformities (Gonzaga et al., 2000). Furthermore, the Paleozoic sequences were affected by a magmatic event, happened ~201.525 ± 0.065 Ma (Davies et al., 2017) and corresponding to the CAMP activity, at which tholeiitic basaltic sills intruded in distinctive levels throughout the basin. Particularly, in the Nova Olinda Formation there is a great presence of sills at all the levels of the lithologic column (Gonzaga et al., 2000).
Below there is a brief description of the sequences and formations that can be found within the basin (Fig. 3.7):

- Ordovician-Devonian sequence: it presents an alternation of marine and glacial clastic sediments. So, in this sequence it is possible to find siltstones, sandstones, shales, pelites, diamictites, etc (Cunha et al., 2007).
- Devonian-Tournaisiana sequence: this represents the second cycle of transgressive and regressive nature occurred in the Amazonas basin, and it

is constituted by the Urupadi group and the Curuà group (Fig. 3.7). The Urupadi group consists of two formations: the Maecuru Formation, composed by sandstones and deltaic or neritic pelites, is characterized by an original T.O.C. of ~0.5%; instead the Ererê Formation is composed by siltstones, shales and neritic to paralic sandstones with an original T.O.C. of ~ 1%. The Curuà group is divided into three main sequences: the Barrairinha Formation, represented by dark gray to black shales deposited during a transgressive event and showing an original T.O.C. of ~ 6%; the Curiri Formation, constituted by glacial to marine diamictites, shales and siltstones and characterized by and original T.O.C. of ~ 1%; the Oriximinà Formation, composed by fluvial-deltaic sandstones and shales associated with storm deposits and showing an original T.O.C. of ~ 0.7% (Cunha et al., 2007; Gonzaga et al., 2000). There is another formation belonging to the Curuà group, the Faro Formation, that, because of its limited extension within the basin, is not considered in our model.

- Pennsylvanian-Permian sequence: this represents a third depositional cycle, after a time lag of about 15 Ma (Cunha et al., 2007). It consits of only a group, the Tapajós group (Fig. 3.7). The Tapajós group is composed by four formations: the Monte Alegre Formation, composed by aeolian sandstones interspersed with siltstones and lacustrine and interdune sandstones and characterized by an original T.O.C. of ~ 1%; the Itaituba Formation, that comprise infratidal carbonates, shales and sabkha evaporites with an original T.O.C. of ~ 0.5%; the Nova Olinda Formation, always composed by infratidal carbonates, shales and sabkha evaporites and characterized by an original T.O.C. of ~ 0.6%; the Andirà Formation, formed by reddish siltstones, sandstones and shales and featured by an original T.O.C. of ~ 0.5% (Cunha et al., 2007; Gonzaga et al., 2000).
- The Cretaceous-Tertiary megasequence is located above all the Paleozoic sediments and is represented by the Alter de Chão Formation (Fig. 3.7), made up of fluvial sandstones and argillites, whom T.O.C. is equal to 0% (Gonzaga et al., 2000).

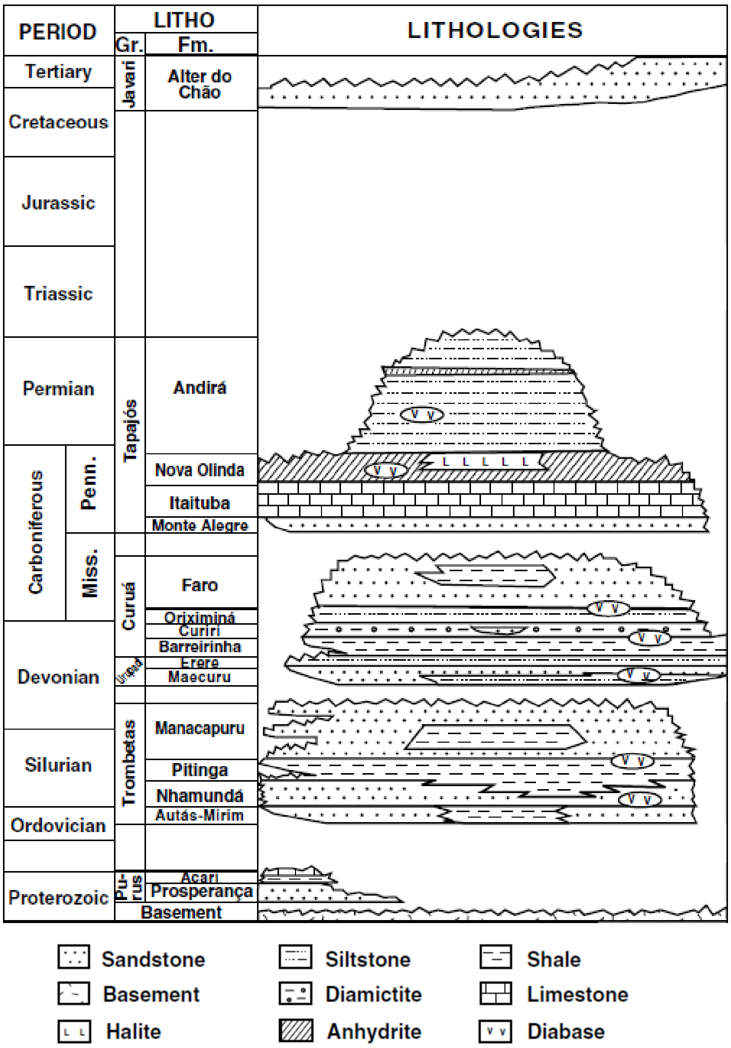

Fig. 3.7 A stratigraphic chart of the Amazonas basin is reported. It is possible to observe the various formations and groups forming the basin. Their ages are shown (modified by Gonzales et al., 2000).

The samples used for this study consist of gray or light brown siltstones and come from the Nova Olinda Formation.

4 Sampling

As previously said in chapter 3, the samples used for this study come from three different localities affected by CAMP magmatism. The sills considered intruded at shallow level (probably at 1-5 km depth) within Triassic or Paleozoic sedimentary sequences. The thickness of the Palisades sill (U.S.A.) is variable: along the Hudson river it reaches a thickness of about 300 m, while along the western margin of the Newark basin it thins to a few tens of meters. The Amelal has a maximum thickness of ~ 100 m where we did the sampling of the underlying sedimentary strata, while it thins out towards the North. The thickness of the Brazilian sills is difficult to estimate. From the stratigraphic section reported below (Fig. 4.1) it appears that in the region where we sampled relatively thin (a few tens of meters) sills were emplaced at several levels within the Paleozoic sediments.

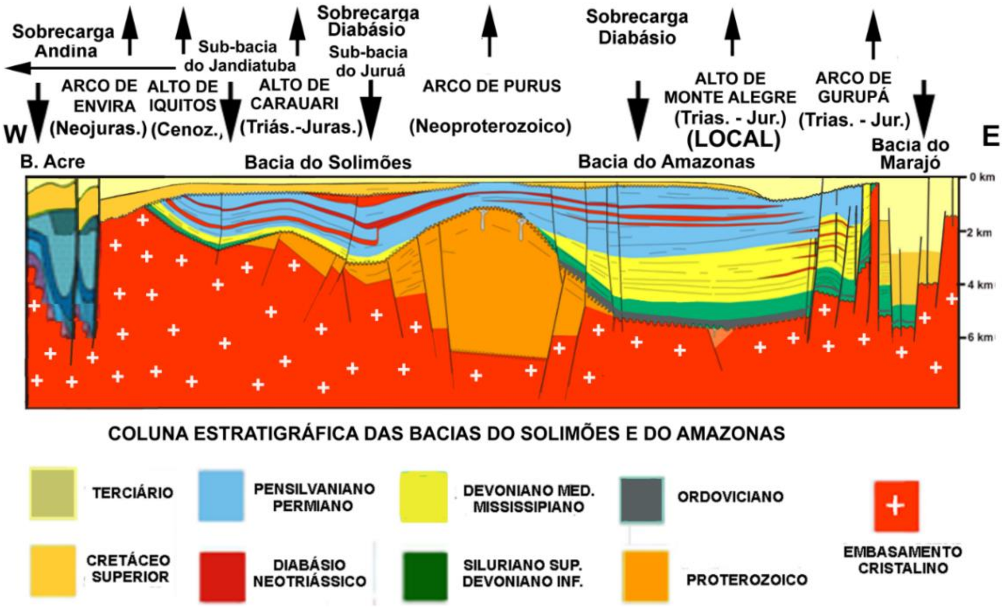

Fig. 4.1 Stratigraphic section for the Amazonas basin and the Solimões one, Brazil (modified from Wanderley Filho and Travassos, 2011).

The used samples have been taken at different distances from the sills. In U.S.A. and in Morocco they were collected from below the sills, while in Brazil the only outcropping sedimentary strata were collected above the sill.

Sampling activity occurred in July 2014 in the Amazonas basin, in September 2015 in the Newark basin, and in October 2015 in the Arganà Valley. I participated to this last sampling campaign.

4.1 Sampling in the Arganà Valley

Fig. 4.2 Location of the Amelal sill, Arganà Valley, between Agadir and Marrakesh (Google Earth).

The sampling activity occurred in a sedimentary section belonging to the Bigoudine Formation located below the Amelal sill (Fig. 4.3), outcropping in the southern Arganà Valley and visible along the road to Agadir (Fig. 4.2).

Fig. 4.3 The Amelal sill is located at the top of the cliff in this picture. It is also possible to observe the sedimentary sequence in which the sill intruded.

Thirty samples, renamed as LV, were taken from this sedimentary section. Sampling started at ca. 78 m from the sill (sample LV 01) and reached the very contact with the sill (sample LV 30 collected just below the first magmatic rock). The average sampling interval was ~ 1.5/2 m, with some exceptions (i.e. sample LV 23 was taken at a distance from the sill of 36 m, whereas sample LV 24 was picked up at a distance from the sill of 31.5 m).

Note that all the samples were wrapped in the tinfoil in order to avoid any kind of contact with extraneous organic Carbon. The samples were then individually rested in a bag to prevent any contact with the other samples in the case of possible tinfoil laceration.

4.2 Sampling in the Newark Basin

Two sites were sampled. One is located in eastern New Jersey, close to the Hudson river, while the second sampling site is located in western New Jersey (Fig. 4.4).

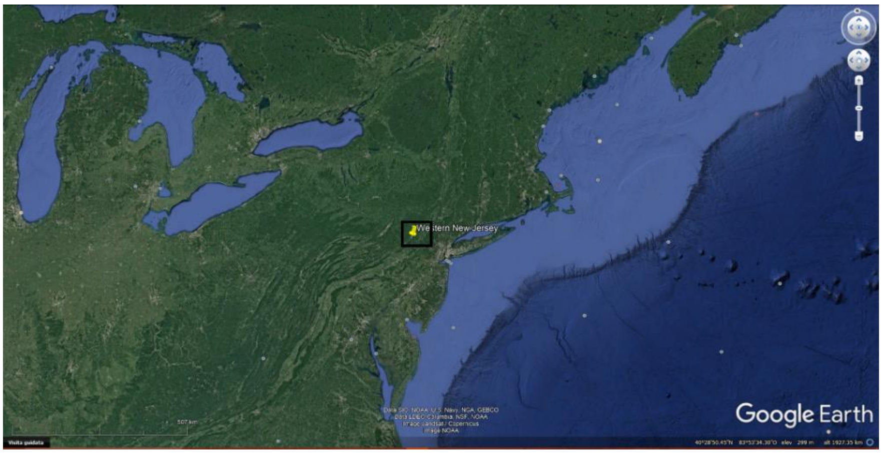

Fig. 4.4 The locality, from which the studied samples were taken, is highlighted by the black rectangle.

At the first site, fourteen samples were collected from the basal contact of the sill (sample LO 12 contains the contact) to about 13 m below the sill. The collected sediments belong to the Lockatong formation. At the second site, eleven samples, named as LO 37 to LO 47, were picked up below a branch of the Palisades sill from a succession of sedimentary strata, also pertaining to the Lockatong Formation. The vertical interval covered by the sampling is of ~ 26 m. The sample LO 47 is the most distant sample from the sill, just harvested at the maximum distance from the sill of ~ 22.3 m. Instead, LO 37 is the closest sample to the sill. The average sampling interval, with which samples were collected, is of ca. 2/2.5 m. Only among the lowest samples (LO 44 – LO 47) the distance increases to 3-4 m.

Also in the case of the American samples, every precaution was taken during the sampling phase. So, the samples were covered with tinfoil, in order to prevent any contamination. The samples were then singularly inserted in little bag to avoid any possible contact with the other samples in the event that tinfoil had broken.

4.3 Sampling in the Amazonas Basin

Fig. 4.5 Above is shown the position of Monte Alegre, Brazil (Google Earth).

The Brazilian samples were picked up from a sedimentary succession (Fig. 4.6), belonging to the Nova Olinda Formation, near Monte Alegre, located in the Parà state along the Amazon River (Fig. 4.5).

Fig. 4.6 The sedimentary succession, from which the Brazilian samples were taken, is shown here.

Nineteen samples were collected within a maximum vertical distance from the sill of ~ 11 m. RS 19 is the sample picked up at the maximum distance from the sill.

Instead RS 2 is the closest sample to the sill, taken at a distance of ~ 0.1 m from the sill.
The sampling interval, with which the samples were picked up, is ~ 0.5 m for the samples RS 02 – RS 15, whereas is equal to ~ 1 m for samples RS 15 – RS 19. During the sampling, care was taken to prevent any kind of contamination; specially, like in the other two cases, the samples were wrapped into tinfoil to avoid contamination with organic Carbon also during the following transportation phases. Note that every sample, after being encased in tinfoil, was put in a bag in order to avoid any kind of contact with the other sample.

Note that the same precautions have been used in the following phases of samples wash and preparation, just to prevent also in these phases any contamination with extraneous organic Carbon or with the Carbon contained in the objects.

5 Methods

The samples considered in our study were used to do different kinds of analysis: Carbon isotopic analysis, XRPD and SEM analysis, vitrinite reflectance, and Rock-Eval analysis.

5.1 Geochemical analyses

The Carbon isotopic analyses and the estimation of the Total Organic Carbon (T.O.C) were performed on a Thermo Scientific Delta V Advantage Isotope Ratio Mass Spectrometer in continuous flow mode, coupled with a Flash 2000 Elemental Analyser and a ConFlo IV interface, present at the Geosciences Department of University of Padova (Fig. 5.1).

Fig. 5.1 The Thermo Scientific Delta V Advantage Isotope Ratio Mass Spectometer present at the Geosciences Department, University of Padova.

Methods of atomic and molecular spectroscopy are based on the existence of separable spectrum lines characteristic of the various isotopes or of isotopic molecules. A Mass Spectrometer may be divided into four different parts: an inlet system, an ion source, an ion deflector or mass separator and an ion detector. Spectrometer analyzes CO_2 gas resulted from high temperature combustion. A beam of electrons is emitted by a heated metal (tungsten or rhenium) filament, and is directed to pass between two parallel plates. Here the beam is collimated by means of a weak magnetic field. Subsequently, positive ions are produced by collisions between gas molecules and the collimated electron beam. The positive ions will be further accelerated by passing through accelerating plates. The light ions will move with a high velocity, the heavy ones with a lower velocity. Afterwards, the ions will enter a magnetic field perpendicular to the direction of the charged particles and they will be deviated. The path the ion follows in the magnetic field is a function of the mass of that ion: this is the basis of mass spectroscopy. After being diverted, the particles, on the base of their mass and path, will collide on one of the machine’s detectors: a current flow will generate that can be converted into an adjustable signal (Hoefs, 1973).
To do this kind of analysis it is necessary to use some international standards and some internal standard, whose $\delta^{13}C$ is known. The international standards used for the spectrometry are the following: IAEA-CH6 and IAEA-CH7, whose isotopic composition is respectively -10.449‰ and -32.151‰ (Coplen et al., 2006). The $\delta^{13}C$ values of these international standards are normalized to the VPDB (Vienna Pee Dee Belemnite) reference standard for calcite. The VPDB is an artificial version of the PDB standard, based on a Cretaceous marine fossil, the *Belemnitella americana*. Note that, besides the international standard $\delta^{13}C$ values, the $\delta^{13}C$ values of both internal standards and geochemical analyses results, reported in this chapter and in the following ones, are normalized to the VPDB reference standard.

The internal standards generally used are two: the first one is a C3 plant sucrose, whose $\delta^{13}C$ is nearly -26‰ (Dal Corso et al., 2017), instead the second one, called MAQ-1, is a mixture prepared from Carrara marble, so it is constituted only just calcite, and its $\delta^{13}C$ value is ca. 2.58%.

In addition to the standards, some blanks (empty capsules of various materials and sizes) are inserted in different runs. Usage of standards and blanks is very important during correction and calibration of raw data, resulting from the analyses with the Elemental Analyser. Blanks are used for the correction of the data, instead calibration is based on repeated analyses of international standards (IAEA-CH6 and IAEA-CH7).

5.1.1 Sample preparation

At first, all the rock samples were crushed with an agate mortar to obtain a fine powder. Close attention was paid to this first phase, in order not to pollute the dust in any way. In fact, the samples were carefully chosen and washed with deionized water. Special attention was also paid to avoid any kind of contact with materials or objects containing Carbon.

For the $\delta^{13}C$ analyses and T.C. estimations, the sample treatment continued with acidification and centrifugation steps. About two grams of sample were placed in falcon tubes and treated with HCl (diluted to 10%) to remove possible residual carbonates from the sediments. Samples were then rinsed with deionized water and centrifugated until neutrality was reached. In a second phase, a variable quantity of samples (6-10 mg for samples from U.S.A.; 16-20 mg for Brazilian samples; 10-15 mg for the Moroccan ones) was weighed, put into tin capsules and fed to the Elemental Analyser.

For the T.O.C. analyses, samples were directly weighed and acidated into silver capsules. In fact, after weighing the samples, six drops of HCl (every drop is equal to 20 μl of HCl) were added to the silver capsules, in order to remove residual carbonates. The silver capsules content was dried for a night and then the capsules were fed to the Elemental Analyser. Note that for the T.O.C. a set of only twelve samples were chosen for each groups of samples. Each sample was weighed and placed in two silver capsules so as to be as safe as possible of the results veracity.

5.1.2 Mass Spectrometer analytical error and sensitivity

The Mass Spectrometer analytical error declared by the manufacturer is ca. 0.2‰. This value is constantly monitored to confirm the validity and the reproducibility of the results. For this purpose, analyses of an internal standard (C3 plant sucrose) are effectuated repeatedly. In a recent study, thanks to the repeated analyses on the C3 plant sucrose, it has been shown that the value for the long-term internal reproducibility is better than 0.15‰ (Dal Corso et al., 2017).

During this work, the machine's sensitivity in measuring Carbon isotope values for low organic matter samples was tested. Two samples, called tre34 and z231, whose $\delta^{13}C$ values were known from a previous study and were of ca. -21.35‰ for the first sample and -28.11‰ for the second one, were considered and diluted with some quartz powder. The fine quartz powder was crushed with an agate mortar in order not to contaminate it with some organic Carbon. In a first step, two mixtures, called tre34-1 and z231-2, were created. The two mixtures contained respectively 12.02% of sample tre34 and 6.41% of sample z231. Then, another mixing, a further dilution with some quartz powder forming ntre34. The quantity of the original sample tre34 contained into the final mixture ntre34 was 4.74%.

After producing these compounds, they were prepared for the analyses to the Mass Spectrometer. So, they were weighed and placed into tin capsules. Many mixture samples, also of different weight, were prepared so as to obtain a reliable and representative data population. Both for mixture tre34-1 and mixture z231-2, twenty-two samples were weighed: twenty samples had a medium weight of 2.12-2.14 mg, while two samples had an average weight of about twelve mg. For the third mixture, ntre34, were prepared twenty samples with a weight ranging between 1.45 mg and 2.46 mg.

The average $\delta^{13}C$ data obtained from the analyzes are as follows: -19.11‰ for the most diluted mixture ntre34; -20.98‰ for low weight mixture tre34-1 samples and -21.31‰ for high weight blend tre34-1 samples; -27.29‰ for low weight mixture z231-2 samples and -28.09‰ for high weight blend z231-2 samples. The isotopic analysis results showed how Mass Spectrometer precision decreases slightly for very diluted compounds (e.g. mixture ntre34) and so for samples whose carbon content is very low. Instead they demonstrated that the machine' s precision in analyzing mixture samples, diluted to ~7%-12% of the total mass, is good or very good on the basis of the sample weight. In fact, $\delta^{13}C$ values for the tre34-1 and z231-2 samples with a high weight (~12 mg) were closer to $\delta^{13}C$ values of the original samples tre34 and z231 than $\delta^{13}C$ values for the tre34-1 and z231-2 samples with a low weight (medium weight of 2.12 mg or 2.14 mg). We can therefore assert that the Mass Spectrometer has a good sensitivity in measuring $\delta^{13}C$ values for sediments whose organic component is particularly diluted. Furthermore, observing the data obtained from this machine sensitivity test, we decided to weigh our Brazilian, Moroccan and American samples over 10 mg, so that the machine's measurements were as good as possible.

5.2 XRPD analyses

The X-ray powder diffraction analyses, carried out at Geosciences Department of University of Padova (Fig. 5.2), were made preliminarily to know the samples composition. They gave some information about the rocks metamorphic conditions and they resulted very useful during the samples preparation for the T.O.C. analyses.

In fact, on the base of rock compositions and of the presence of carbonates, it was possible to decide how many drops of hydrochloric acid to insert in the silver capsules to acidate the samples and to ensure that carbonates remnants were not present in the samples.

The sample preparation for the XRPD analyses is simple and does not require many steps. At first, rocks were broken in order to reduce considerably their size.

After being washed with deionized water and dried in an oven at about 50 °C, they were crushed with an agate mortar to obtain one gram of a fine powder. Next, the powders were placed in a sample holder rotating at an angular velocity ϴ (Fig. 5.2). The machine’s detector, instead, rotates with a double angular velocity of 2ϴ to preserve the reflection condition with respect of the sample surface. The detector performs continuous scans changing its angle around the sample and keeping a distance R constant. The final product are the diffractograms, diagrams in which several peaks, placed at various position 2ϴ and linked to the different phases present in the rocks, are represented.

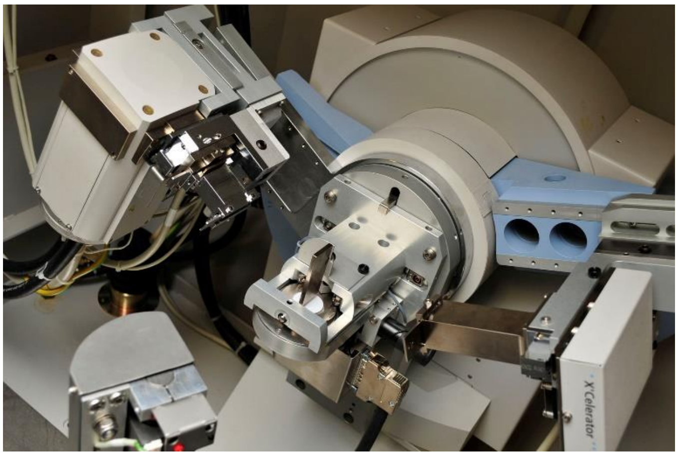

Fig. 5.2 Internal details of the diffractometer present at the University of Padova.

5.3 Scanning Electron Microscope (SEM) analyses

The Scanning Electron Microscope analyses were carried out at Department of Geosciences at University of Padova. These analyses have proved to be necessary to clarify the samples composition or to estimate the maximum temperature reached by the samples at contact with sills. SEM analyses have been very useful in the case of Brazilian samples to try to discriminate the temperature reached in the area surrounding the intruded sill according to the presence or absence of some minerals, as biotite or graphite.

The sample used for the SEM analyses consists of a thin section, which is bombed and scanned by an electron beam. The beam is produced by a metal filament, generally tungsten, for thermo-ionic effect. The filament has a dimeter of 0.1 mm and is placed on an insulating material. It must be crossed by a current of 2.5 A to gain the temperature at which the thermo-ionic effect can happen and to produce the electron beam.

Thanks to the Scanning Electron Microscope (Fig. 5.3), it is possible to have a greatly enlarged image of a rock thin section. So, structures, zoning or minerals of very small sizes can be observed.

Fig. 5.3 The Scanning Electron Microscope present at the Geosciences department of University of Padova.

At first, the preparation of thin sections requires rock samples to be cut with a diamond-studded saw in order to reduce their dimensions. Once the samples are reduced to the size of a brick, they are polished on a spring with abrasive pastes. The rock bricks are then glued to some slides. They are left to rest so as to dry the glue. The bricks dimensions are further diminished and, finally, there is the last polish before the thin sections are ready.

5.4 Vitrinite reflectance analyses

Vitrinite derives from kerogen type III and is an amorphous portion of the organic matter. In effect, it is a maceral of Carbon deriving from the lignin-cellulosic walls of the plant cells. Under the microscope, it seems to be translucent, with a color ranging from ochre yellow to dark brown (Fig. 5.4).

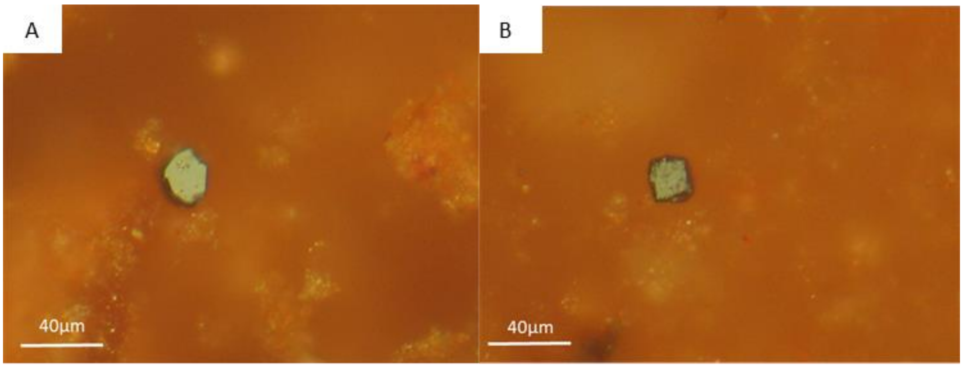

Fig. 5.4 Fragments of vitrinite in two samples from Morocco: A) sample LV 2 B) sample LV 25.

The vitrinite reflectance (Ro%) is the most used indicator to determine the maturity of the source rock. The method is based on vitrinite' s ability to reflect the light and on the ratio between reflected and incident light, expressed as a percentage. The measurement of the vitrinite reflectance power is related to the fact that, with the increase of temperature, the structure of the organic matter becomes more and more ordered producing a bigger ability to reflect the incident light. So, at increasing temperature, there is an increase in vitrinite reflectance values.

The vitrinite reflectance analyses were carried out at Roma Tre University. The samples chosen for this type of analysis were prepared only preliminarily at

Geosciences Department at University of Padova. So, at first from the original rocks, smaller fragments were obtained. These fragments have been cleaned and washed and, lastly, they have been ground with an agate mortar.

Note that very small fragments of organic matter or the reshaped ones, like also the inertinite fragments, are generally excluded to calculate Ro% average values.

5.5 Rock-Eval Pyrolysis analyses

Rock-Eval analyses were made at Earth Science Department of the University of Lausanne. The purpose was to obtain an estimate of the temperature reached by samples selected and information concerning their thermal maturity for this type of analysis.

The Rock-Eval pyrolysis is a quantitative analysis of the hydrocarbons produced by kerogen pyrolysis. It is very used in Petroleum Geology in estimating the petroleum potential of sedimentary rocks by heating samples in an open pyrolysis system under non-isothermal conditions (Behar et al., 2001).

About 100 mg of finely ground rock sample is placed into a furnace at 250 °C, in an inert atmosphere, and raised to a temperature of 550 °C. An internal probe records the temperature corresponding to the maximum pyrolysis. Different kinds of data are provided: three of the most important data obtained by the analysis are peaks and are called S1, S2 and S3. These three peaks give information about the hydrocarbons already present in the rock before pyrolysis and evolved at a low temperature of ca. 300 °C (S1), about the hydrocarbons (oil and gas) that can still be produced by kerogen breakdown (S2) and the volatiles amount produced after the kerogen cracking and during the cooling (S3; Behar et al., 2001). Another important parameter provided is the maximum temperature (Tmax), at which the generation of S2 occurs. Tmax is an expression of kerogen maturity. The higher will be the maximum temperature values and the longer the kerogen maturity will be (Behar et al., 2001).

For the Rock-Eval analyses, the samples were prepared preliminarily at Geosciences Department at University of Padova. The samples were reduced in size and washed with some deionized water. Then they were dried in a 45°C degree oven and they were crushed with an agate mortar to avoid any kind of contact with organic Carbon.

6 Numerical Modeling: a 1D Sill Model

In this work we have used a 1D FEM (Finite Element Method) numerical model in Matlab, SILLi, in order to quantify the amount of CO_2 released into the atmosphere by sill intrusions into sedimentary sequences. SILLi (Iyer et al., 2017b) calculates the thermal effects of sill emplacement into sedimentary strata in basins and can be used with any lithological column characterized by tabular magmatic intrusion with a regular shape. The model considers not only the magmatic activity which interested a basin, but all the basin's evolution: from the depositional events to the erosional ones, from its initial geothermic history to sill emplacement and thermal perturbations, from its burial history to the alteration of organic matter during basin's development. The 1D Sill Model has a further advantage: in fact, it allows to consider the intrusion of multiple sills both at the same time and at different moments of the basin's evolution (Iyer et al., 2017b). The data required for the correct usage of this 1D Sill Model are several: they can be extrapolated from previous studies, especially in the case of information concerning the stratigraphy of the basin or in the case of specific characteristics for each formation present in the basin; data can also be obtained from different analyses such as Carbon isotopic analyses or vitrinite reflectance analyses. All the data are inserted into an Excel file, whose name is entered in the Main Matlab script (named sill1d_main.m), one of the necessary files required to run the model. The other needed scripts to run the model are: the Matlab script to read input (called sill1d_input.m), the Matlab computational script (named sill1d_compute-dep.m), the 1D thermal solver (denominated thermal1d_fem.m), the Vitrinite reflectance calculation script (coeff_diff.m) and the post-processing scripts (such as geological_timescale_color.m, geological_timescale_data.m, hatchfill.m, errorbarxy.m, input_postproc.m, output_postproc.m). All these scripts must be present in the same directory (Iyer et al., 2017b). After running the model, it is possible to observe its results. The results show the thermal evolution of the stratigraphic columns considered and all the changes happened after sill emplacement such as TOC changes. The amount of organic and inorganic CO_2 released in the atmosphere after sill intrusion is also considered and shown.

6.1 Model Input File

The model input consists of an Excel file (*.xls) and is read by the Matlab file, SILLi.m. The Excel file is composed by seven tabs containing all the parameters needed for the model's correct development and described later in this paragraph. For this study, all the required parameters (i.e. rock density, thermal conductivity, original, heat capacity, etc…), concerning the different lithologies and the sill/s present in the studied basins, were taken from Aarnes et. al (2011) or from Waples and Waples (2004).
All the input data must be based on information obtained from the observation and the study of a borehole (with horizontal stratigraphy) or of an outcrop. If the case study is outcrop-based, it is important to understand the basin stratigraphy and reconstruct a stratigraphic column. In addition to this, if the stratigraphy was tilted after sills emplacement, the strata and the sill/s should be rotated back to their original horizontal position (Iyer et al., 2017b).

As said previously, the Excel file used for this model consists of seven different tabs, based on data required.

- Fluid: this is the first tab and contains three columns related to the pore-fluid properties. The three columns describe the fluid name, its density (kg/m^3) and its heat capacity (J/kg/K). Water is the default fluid considered. Only a single phase can be insert (Iyer et al., 2017b);
- Lithology: this is the second tab present in the input Excel file. Here it is possible to find input data for the stratigraphic column. The parameters

required for each formation are density (kg/m^3), heat capacity (J/kg/K), porosity (fraction), thermal conductivity (W/m/K), initial T.O.C (Total Organic Carbon) content (wt%), latent heat of organic maturation (kJ/kg) and latent heat of dehydration (kJ/kg). Note that all the properties used should correspond to the current values. It is possible to give to the model some information about the carbonate type contained into each formation. So, in the specific column, values ranging from one to three should be inserted (1 = marl, 2 = dolomite, 3 = dolomite/evaporite mix). Other parameters, which can be included, are the present-day top depth (m) and the age (Ma) of each formation. These two values are important to reconstruct the depositional sequence and to determine the sedimentation rate of each layer. Note that the age of each formation must be expressed by a single value (generally the average value of the depositional interval is chosen) (Iyer et al., 2017b).

In some columns, such as the porosity column, the T.O.C. column, the latent heat (both of organic maturation and of dehydration) and the carbonate columns, zero values can be inserted (Iyer et al., 2017b). The data concerning the erosional events are entered in another tab, described below;

- Erosion: the properties required for this tab are similar to those used in the Lithology tab, with the addition of the erosion time (Ma) and the thickness (m) of the eroded stratum. Note that the top depth of the eroded layer must be coincident with the top depth of a sedimentary layer present in the Lithology tab. Instead the age of an eroded layer can not be the same of that of any other layer: in fact, generally it has to be later than the time of deposition (Iyer et al., 2017b). Particular attention must be paid to the case in which the erosion time of an eroded layer lies between the depositional time of the eroded layer and the sediments above it (Iyer et al., 2017b);
- Sills: this fourth tab contains the necessary information for the description of the sill/s emplaced into a sedimentary basin. Besides the top depth and the sill thickness, other parameters are required such as the emplacement

time (Ma), the emplacement temperature (°C), the melt and solid densities (kg/m^3), the melt and the solid heat capacities (J/kg/C), the latent heat of crystallization (kJ/kg), the solidus and liquidus temperatures of the magma (°C) and the thermal conductivity (W/m/K). The intrusion of a sill is considered as an instantaneous event. Furthermore, a sill top depth can not correspond with the top depth of a sedimentary stratum. On the other hand, the top depth of a sedimentary layer can not be internally to a sill inclusion (Iyer et al., 2017b);

- Temperature data: this tab contains temperature data (°C) in relation to the depth (m). It allows to reconstruct the geothermal gradient of the sedimentary basin considered. It is necessary to insert at least two data points: the first one must coincide with the sedimentary basin surface and so with the top of the stratigraphic column (Iyer et al., 2017b). Care should be taken not to attribute negative values to the sedimentary column top depth, based on the geotherm: negative values can only be assigned if necessary (Iyer et al., 2017b);
- Vitrinite data: the present-day vitrinite reflectance data are assigned to this tab. There are three columns in which it is possible to write in depth values (m), vitrinite data values (%Ro) and the standard deviation of the values. All these data are not compulsory: they have to be inserted only when available. Specially, they are very useful to increase the model resolution, allowing a direct comparison between the modelled vitrinite values and the vitrinite reflectance observations (Iyer et al., 2017b);
- T.O.C. data: this is the last tab. Here T.O.C. content data measured from samples coming from the sedimentary column are input. There is also a column to enter the depth data of each sample. The tab may not be compiled if no information is available. Obviously, these data are useful and necessary to make a good comparison between the measured T.O.C. data and the modelled T.O.C. data (Iyer et al., 2017b).

6.2 Method

The one dimension model recreates the thermal effects of sill emplacement into a sedimentary basin. Each sedimentary layer, included the eroded layers, is deposited sequentially in time. The sedimentation rate for each stratum is defined by the ratio between the layer thickness and the time difference between its top age and the top age of the layer previously deposited (Iyer et al., 2017b).

For the discussion of the future two paragraphs, reference will be made to the following Tab. 6.1 (Iyer et al., 2017b):

Symbol	Description	Units
A	Frequency or Arrhenius factor	s^{-1}
c_{peff}	Effective rock heat capacity	$J\ kg^{-1}\ K^{-1}$
c_{pf}	Fluid heat capacity	$J\ kg^{-1}\ K^{-1}$
c_{pr}	Rock heat capacity	$J\ kg^{-1}\ K^{-1}$
c_{pm}	Melt heat capacity	$J\ kg^{-1}\ K^{-1}$
E	Activation energy	$KJ\ mol^{-1}$
f	Stoichiometric factor	
F	Fraction of reactant converted	Fraction
g	Gravitational acceleration	$m\ s^{-2}$
i	Reactive component	
L_c	Latent heat of crystallization	$kJ\ kg^{-1}$
L_{om}	Latent heat of maturation	$kJ\ kg^{-1}$
m_{CO_2}	Carbon to CO_2 conversion factor	3.66
R	Gas constant	$J\ K^{-1}\ mol^{-1}$
R_{CO_2}	Rate of CO_2 generation	$kg\ m^{-3}\ s^{-1}$
R_{om}	Rate of organic matter degradation	$kg\ m^{-3}\ s^{-1}$
t	Time	s

T_L	Liquidus temperature	°C
T_S	Solidus temperature	°C
T	Temperature	°C
T_{d1}	Upper temperature limit of dehydration reactions	°C
T_{d2}	Lower temperature limit of dehydration reactions	°C
T_{d1} - T_{d2}	Temperature range for dehydration reactions	350-650°C
w	Amount of reactive component	Fraction
w_i	Amount of material for component i	Fraction
w_0	Initial concentration of the total reactant	Fraction
w_{0i}	Initial concentration for the component i	Fraction
φ	Rock porosity	Fraction
ρ_f	Fluid density	kg m^{-3}
ρ_r	Rock density	kg m^{-3}
κ	Conductivity	W m^{-1} K^{-1}
TOC	Quantity of T.O.C. that has reacted for each time	%
TOC_0	Initial T.O.C. of a rock	%

Tab. 6.1 Above all the parameters used in the SILLi model are reported (modified from Iyer et al., 2017b).

6.2.1 Thermal Diffusion

The thermal solver calculates the temperature inside the stratigraphic column. Its work is based on the geotherm described in the fifth tab of the input file and on the heat diffusion equation,

$$[\varphi\rho_f c_{pf} + (1-\ \varphi)\rho_r c_{peff}]\frac{\partial T}{\partial t} = \nabla \cdot (\kappa \nabla \mathrm{T}) \qquad (1)$$

Where φ is the rock porosity, ρ_f represents the fluid density, c_{pf} is the fluid heat capacity, ρ_r is the rock density, κ is the conductivity of a rock, T is the temperature (Tab. 6.1). c_{peff} is the effective rock heat capacity,

$$c_{peff} = c_{pm}\left[1 + \frac{L_c}{(T_L - T_S)c_{pm}}\right] \text{ if } [T_S < T < T_L] \quad (2)$$

$$c_{peff} = c_{pr} \qquad\qquad \text{if } [T_S > T] \quad (3)$$

Note that the effective rock heat capacity accounts for the latent heat of fusion in the crystallizing parts of the sill (Svensen et al., 2017; Iyer et al., 2017b; Galushkin,1997).

Thanks to the geotherm and the energy diffusion equation, the thermal solver can calculate and apply some fixed temperatures both at the top and the bottom of the sedimentary sequences at every step, in order to computes the temperature reached within the sedimentary columns (Iyer et al., 2017b). Note that sill emplacement is considered as instantaneous: it occurs at the specified time and temperature. This assumption is of great help while the model is developing and especially during thermal diffusion study. The thermal diffusion happens after sill intrusion. The time-steps used for thermal diffusion are automatically calculated on the base of sill thickness and characteristic time, required for thermal diffusion. At first, the time step is small in order to try to solve in the most accurate way the thermic evolution of the contact aureole developed all around the sill. At a later time, when the energy released by the sill/s cooling will be entirely dispelled, the time-steps used will be gradually raised (Iyer et al., 2017b). As known into the contact aureole dehydration reactions occur. Heat diminution due to its consumption during dehydration reactions at high temperature is a further factor that influence the rocks thermal state near the intrusion (Galushkin, 1997; Hanson and Barton, 1989). The dehydration reactions are limited by rising temperature of the rocks and by a temperature interval of about 350-650 °C (Galushkin, 1997). So, in the model they can be amplified by modifying the energy diffusion equation when sediments temperature increase into the above mentioned temperature range (350°C<T<650°C) (Iyer et al., 2017b; Wang et al., 2012; Galushkin, 1997). The energy diffusion equation will be modified in the following way:

$$\left[\varphi\rho_f c_{pf} + (1 - \varphi)\rho_r c_{peff}\right]\frac{\partial T}{\partial t} = \nabla \cdot (\kappa \cdot \nabla \mathrm{T}) - \mathrm{H} \tag{4}$$

where H is:

$$H = \frac{(1 - \varphi)\rho_r L_d}{T_{d1} - T_{d2}} \cdot \frac{\partial T}{\partial t} \tag{5}$$

When in the sedimentary column there is an erosional layer, the model also considers the erosional event as an event that happens in a unique step at a certain time. The top and bottom temperature boundary conditions will be accordingly changed in the new stratigraphic column (Iyer et al., 2017b).

6.2.2 Thermal maturation of organic matter

Vitrinite reflectance is one of the most common indicators of thermal maturity. It is not only used in basin analysis or in the exploration for oil and gas, but also for estimating the maximum temperature reached by sedimentary rocks near igneous intrusions or in geothermal area. The EASY%Ro method, presented for the first time by Sweeney and Burnham (1990), is a widely utilized method for the calculation of the thermal maturity of a source rock: it is also used in the SILLi model. This model can be used for any type of thermal history. In fact it can be utilized in cases as non-deposition, uplift and cooling, or when heating rates change during the time (Sweeney and Burnham 1990).

The EASY%Ro model uses twenty Arrhenius first-order parallel-reactions with the purpose to describe the complex mechanisms leading to the kerogen breakdown due to the increased temperature. The Arrhenius reaction used in the model for the i^{th} component at a time-dependent temperature is given by:

$$\frac{dw_i}{dt} = -w_i A exp\left[-\frac{E_i}{RT^t}\right] \tag{6}$$

where w_i is the amount of material for each component i, A is the frequency or Arrhenius factor, E_i is the activation energy (Tab. 6.1) and T^t, as mentioned just before, is the time-dependent temperature (Iyer et al., 2017b; Sweeney and Burnham, 1990). Note that we use a range of activation energies in EASY%Ro method because itself is a function of temperature. The choice to make use of twenty parallel equation with the same A (frequency factor) and different Es (activation energies) is based on the fact that the complex reactions, such as kerogen breakdown, are better represented by a set of parallel reactions (Sweeney and Burnham, 1990).

The total amount of material which has reacted can be determined by summarising all the individual reactions:

$$\frac{dw}{dt} = \sum_i \frac{dw_i}{dt} \tag{7}$$

Then we can obtain the fraction of reactant converted thanks to the following formula:

$$F = 1 - \frac{w}{w_0} = 1 - \sum_i f_i \left(\frac{w_i}{w_{0i}}\right) \tag{8}$$

where w is the amount of reactive component, w_0 is the initial concentration for the component i, w_i is the amount of material for the component i, w_{0i} is the initial concentration for the component i and f_i is the stoichiometric factor for the parallel reaction components (Tab. 6.1). Thanks to the last equation, the vitrinite reflectance values can be easily calculated. For this aim the used equation is the following:

$$\%Ro = exp(-1.6 + 3.7F) \tag{9}$$

where F is the fraction of reactant converted (Tab. 6.1). Through the penultimate algorithm described above, it is also possible to compute the quantity of T.O.C. that has reacted for any set time using the initial T.O.C. of a rock (TOC_0) and F the fraction of reactant converted at a datum time:

$$TOC(t) = TOC_0 F(t) \tag{10}$$

Consequently, the rate of organic matter degradation can also be calculated by:

$$R_{om} = (1 - \varphi)\rho_r \frac{\partial TOC}{\partial t} \tag{11}$$

where φ is the rock porosity, ρ_r is the rock density and *TOC* equals to the quantity of T.O.C. reacted for each time (Tab. 6.1).

Generally, following the metamorphic action on sedimentary rocks, the production and emission of CH_4 occur (Aarnes et al. 2010). In this work, we assume that all the organic matter, present in the contact aureole, has been converted into carbon dioxide (CO_2) because of kerogen breakdown. Besides, the EASY%Ro method assumes that the maximum quantity of T.O.C. converted in CO_2 is equal to the 85% of the initial amount. Although this percentage is a good initial approximation, it does not take into account the variation in the consumption and transformation of organic matter into the contact aureole (Iyer et al., 2017b; Svensen et al., 2015). In the inner part of a contact aureole, data show that all the organic matter has reacted or has been consumed due to a strong increase of temperature that triggered the reactions necessary for this purpose

(Iyer et al., 2017b). The amount of CO2 produced $\left(R_{CO_2}\right)$ for a time-step and so released is equal to:

$$R_{CO_2} = R_{om} m_{CO_2} \tag{12}$$

where m_{CO_2} is a stoichiometric factor used to convert organic matter into CO2 (Tab. 6.1).

As a consequence of what has been discussed in this subsection, the energy diffusion equation will be equal to:

$$\left[\varphi \rho_f c_{pf} + (1 - \varphi)\rho_r c_{peff}\right] \frac{\partial T}{\partial t} = \nabla \cdot (\mathrm{κ} \cdot \nabla \mathrm{T}) - \mathrm{H} - L_{om} R_{om} \tag{13}$$

where φ is the rock porosity, ρ_f represents the fluid density, c_{pf} is the fluid heat capacity, ρ_r is the rock density, c_{peff} represents the effective rock heat capacity, κ is the conductivity of a rock, T is the temperature, R_{om} is the rate of organic matter degradation, and L_{om} is the latent heat of maturation for the organic matter (Tab. 6.1). H is a parameter obtainable from (5).

6.3 Model Output: Graphical User Interface (GUI)

The model output consists of a GUI (Graphical User Interface) which contains three tabs: the first one represents all the input data, the second one shows the time evolution of the model results and the last one contains two graphic representations of the released CO2, both organic and inorganic (Iyer et al., 2017b).

In the results tab we can observe the evolution of temperature, vitrinite reflectance, TOC content, maximum temperature, hydrostatic pressure, organic and inorganic CO2 released in the sedimentary column during the time period considered for the development of the model (Iyer et al., 2017b; Fig. 6.1). Note that the regions highlighted in grey and reported within the different graphs (see Fig. 6.1) represent the sill intrusion.

Thanks to the results tab (Fig. 6.1), it is possible to examine the behavior of the individual curves, each of them are attributed to a singular parameter. The observation of the curves movement as they approach the sill is particularly interesting. It is also possible to create a correlation between the various observables parameters.

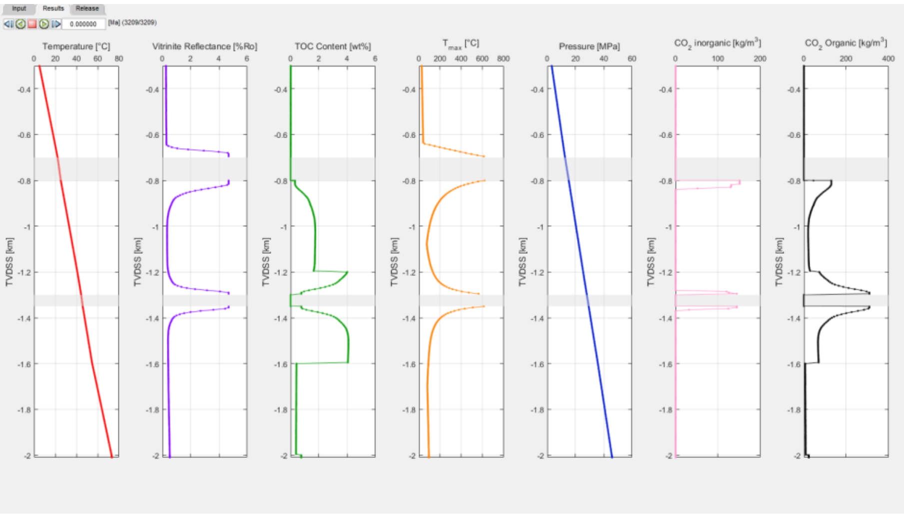

Fig. 6.1 Snapshot of the results tab for a hypothetical sedimentary column with two sills intruded visible as the regions highlighted in grey (from Iyer et al., 2017b).

The amount and the release rates of organic and inorganic CO_2 generated by the sediments heating present all around a sill intrusion are shown in the release tab (Iyer et al., 2017b; Fig. 6.2). Note that the amount and the rates of release of CO_2 are extended all over the entire stratigraphic column.

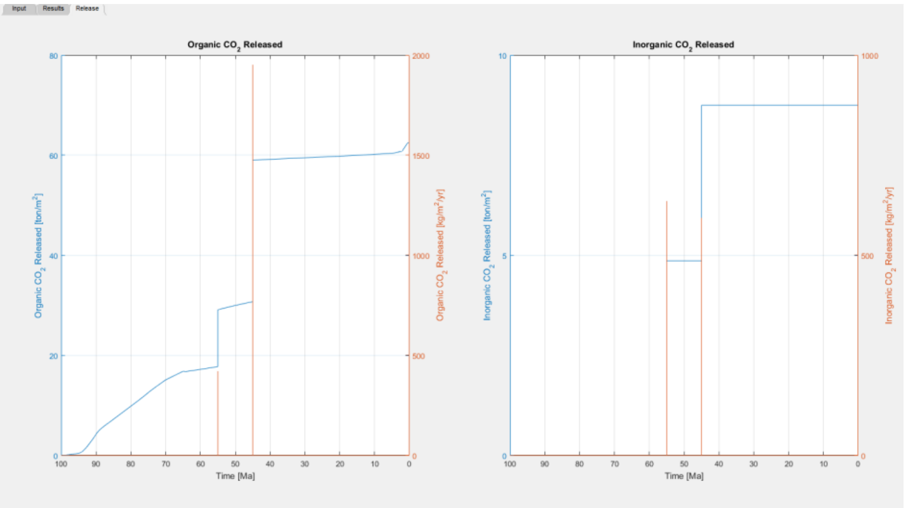

Fig. 6.2 Example of a release tab for a hypothetical sedimentary column. As it is possible to observe, in this tab the graphic for the organic CO2 and the inorganic CO2 released into the atmosphere are showed (from Iyer et al., 2017b).

We can use the cumulative amount and rates of release of CO_2 to quantify the total volume of gas released in the atmosphere simply by multiplying the values by the total area of basin interested by sill intrusion (Iyer et al., 2017b). Svensen et al. (2007) suggested to use the following formula to calculate the total mass of carbon generated in a contact aureole:

$$WC = FC * A * h * d \tag{14}$$

where WC is the total mass of carbon generated in contact aureole, FC is the amount of carbon, expressed in wt%, converted to methane or carbon dioxide, A is the area of the contact aureole, h is the sill thickness and d is the rock density (about 2400 kg/m^3 for shallow crust). The total mass of carbon released because of thermal metamorphism can be finally converted to equivalents of methane (WC $*$ 1.34) or carbon dioxide (WC $*$ 3.66) (Svensen et al., 2015). For instance, if only 1 wt% of the organic carbon contained in shales or siltstones is transformed into some kind of carbon-based gas, the gas production, associated with a cumulative volume of 5000-10000 km^3 sill intrusion, is equivalent to 230-460 Gt C, corresponding to 310-600 Gt of CH_4 (Svensen et al., 2015; Svensen and Jamtveit, 2010).

6.4 Model limitations

The model shows some limitations. One of them has been already discussed in the subsection 1.2.2 and it is concerning the percentage of conversion of T.O.C present in all sedimentary rocks used in the EASY%Ro method. Another one important limitation is due to the fact that the model is one-dimensional and it is not able to resolve thermal effects that would require a three-dimensional model (Iyer et al., 2017b). Furthermore, as recalled by Iyer et al. (2017a), the model does not take into account for the advective transport of heat. Previous models (Iyer et al. 2017a) have shown that this process is dominant is high permeability systems or at sill borders when a sill is intruded in a low permeability system. This model, instead, works well in the case of low permeability systems in which shales, mudstones, marls, sandstones with a very low granulometry, etc., are present (Iyer et al. 2017b). One last model restriction, showed by Iyer et al. (2017b), is linked to the fact that in the contact aureole it does not consider any other kind of reactions besides the decarbonation reactions.

7 Results

7.1 Geochemical Results

As previously said, geochemical analyses on the organic matter have been made at the University of Padova. Thermo Scientific Delta V Advantage Isotope Ratio Mass Spectrometer has been used to carbon isotopic analyses, through which we have obtained carbon also T.C. and T.O.C. values.

In the following subparagraphs, the geochemical results of each of the three series of samples used in our study (the first one from Brazil, the second one from Morocco and the last one from the U.S.A.) are shown and described.

7.1.1 Geochemical results for Brazilian samples

From Tab. 7.1 it is possible to observe how T.C. values (%) increase moving away from the sill. In fact, sample RS 02 is located at a distance of ~ 0.2 m from the sill and presents a T.C. value of 0.03%, whereas RS 19, taken at a distance from the sill of ca. 10.7 m, shows a T.C. value of 0.21%. Particularly, from sample RS 16 T.C. values are higher than 0.1% (with the exception of sample RS 09, yielding a T.C. of nearly 0.1%). This trend has been interpreted as the result of sill's intrusion. Because of the intrusion of the sill, the organic matter would be subject to a series of reaction that, as described in chapter 2, would trigger the CO_2 formation and the subsequent degassing into the atmosphere. Instead, Carbon isotope values do not show any particular variation. Their values are all concentrated at ca. -25‰, and their average value is ~ 25.24‰.

Sample	Distance (m)	Weight (mg)	δ13C (VPDB)	TC%
RS 02	0.2	19.426	-26.99	0.01
RS 03	0.7	13.367	-25.16	0.01
RS 04	1.2	18.843	-25.10	0.02
RS 05	1.7	17.117	-23.62	0.02
RS 06	2.2	17.090	-25.42	0.01
RS 07	2.7	15.240	-25.79	0.01
RS 08	3.2	16.514	-24.25	0.02
RS 09	3.7	13.033	-26.20	0.02
RS 10	4.2	16.670	-25.88	0.03
RS 11	4.7	10.378	-24.69	0.05
RS 12	5.2	17.480	-24.71	0.03
RS 13	5.7	10.766	-24.08	0.05
RS 14	6.2	19.503	-25.05	0.08
RS 15	6.7	17.913	-25.97	0.08
RS 16	7.7	14.012	-25.88	0.12
RS 17	8.7	11.915	-25.47	0.09
RS 18	9.7	8.138	-25.29	0.24
RS 19	10.7	9.854	-25.93	0.21

Tab. 7.1 From left to right: samples name, samples distance from the sill, amount of sample used to make carbon isotopic analyses and estimate the total carbon value, carbon isotopes results and total carbon results. Note that the weight of all the samples is between 8 mg and ca. 20 mg.

Later on, T.O.C. analyses have been performed. As explained in subparagraph 5.1.1, not all samples have been considered to make the T.O.C. analyses: in fact, only twelve samples have been examined and it has been preferred to use the most distant samples, starting from the last one (RS 19).

Interestingly, as it is reported in Tab. 7.2, T.O.C. data are very similar to T.C. data. This means that the total content of carbon corresponds to the total content of organic carbon and that in both cases all carbonate residues have been removed.

Observing further Tab. 7.2, it is also possible to note that T.O.C. values (%) increase moving away from the sill. So, the previously mentioned trend is confirmed and the hypothesis according to which the presentday values are the product of a probable CO_2 degassing into the atmosphere, occurred after sill intrusion.

Sample	Distance (m)	Weight (mg)	TOC (%)
RS 07	2.7	12.900	0.01
RS 07	2.7	12.137	0.01
RS 08	3.2	11.947	0.01
RS 08	3.2	10.902	0.01
RS 09	3.7	11.835	0.02
RS 09	3.7	14.835	0.02
RS 11	4.7	14.554	0.03
RS 11	4.7	18.490	0.03
RS 12	5.2	17.232	0.03
RS 12	5.2	15.439	0.03
RS 13	5.7	10.662	0.05
RS 13	5.7	11.958	0.05
RS 14	6.2	11.676	0.08
RS 14	6.2	10.006	0.09
RS 15	6.7	15.550	0.05
RS 15	6.7	12.889	0.04
RS 16	7.7	11.017	0.11
RS 16	7.7	12.147	0.11
RS 17	8.7	16.035	0.07
RS 17	8.7	16.202	0.08
RS 18	9.7	18.406	0.16
RS 18	9.7	13.567	0.16
RS 19	10.7	15.972	0.19
RS 19	10.7	16.128	0.19

Tab. 7.2 In the table are reported the name of each sample used for T.O.C. analyses, their distance from the sill, their amount used for the analyses and their T.O.C. values.

The T.C. trend for the Brazilian samples, which as mentioned above has been found to correspond to the T.O.C. trend, is well visible in Fig. 7.1.

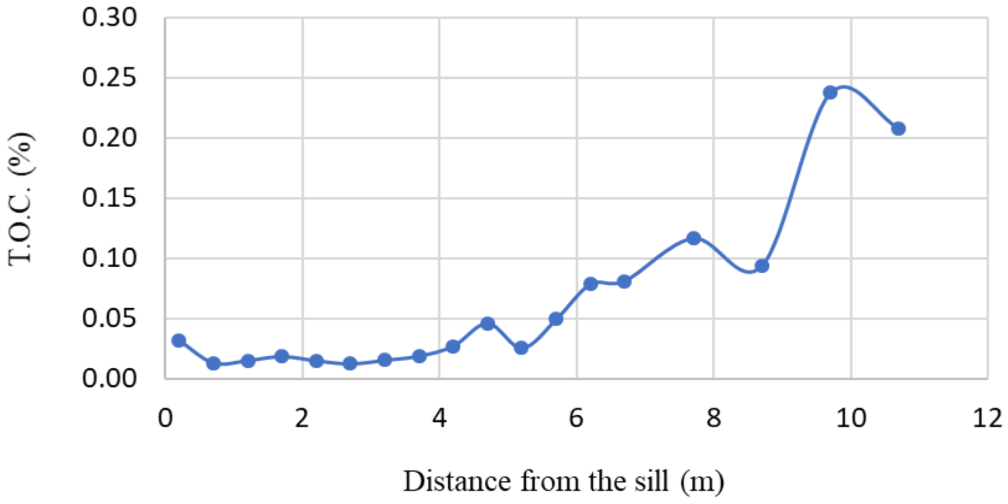

Fig. 7.1 the T.C. trend for the Brazilian samples. It is possible to observe the T.C. values increase with the increase of the distance from the sill.

7.1.2 Geochemical results for Moroccan samples

The geochemical analyses on the Moroccan samples do not include T.O.C. data. The choice not to carry out this type of analysis on Moroccan samples has been dictated by their low organic matter content. In fact, considering that these samples didn’t react during the laboratory acidification phase, which means that their carbonate content was really low, we could estimate that their Total Carbon values (Tab. 7.3) were equivalent to their Total Organic Carbon values. As it is possible to observe in Tab. 7.3, Total Carbon (T.C.) values (%) are very low and no trend is visible for the Moroccan samples. The low carbon content can be attributed to the nature of the Bigoudine Formation to which the collected samples belong. In fact, according to several authors (Hoffman et al., 2000; Olsen, 1997) the Bigoudine Formation was deposited under more arid conditions. On the basis of these data, it would seem that, in the case of the Arganà

Valley, the intrusion of the Amelal sill did not have a great impact on the organic matter, whose quantity was already low before the sill intrusion.

This suggests that in this context, despite the Amelal sill thickness (~ 100 m), the CO_2 degassing, occurred due to the sill emplacement, was neglible.

Sample	Distance (m)	Weight (mg)	$\delta^{13}C$ (VPDB)	TC (%)
LV 01	77.7	10.869	-26.25	0.11
LV 02	76.7	10.979	-21.16	0.01
LV 03	75.7	14.506	-21.05	0.01
LV 04	75	10.467	-24.82	0.07
LV 05	73.9	14.761	-25.58	0.05
LV 06	71.3	11.250	-26.19	0.07
LV 07	70.5	12.638	-24.79	0.04
LV 08	69.5	12.672	-26.35	0.04
LV 09	68	11.245	-25.57	0.03
LV 10	66.8	10.611	-26.09	0.06
LV 11	64.3	11.107	-25.34	0.05
LV 12	61.8	11.985	-26.30	0.04
LV 13	60.5	11.556	-26.06	0.05
LV 14	56.5	13.711	-26.72	0.09
LV 15	54.5	13.033	-25.83	0.04
LV 16	52.5	11.177	-22.64	0.02
LV 17	50.5	10.306	-26.36	0.04
LV 18	49.9	11.766	-26.57	0.10
LV 19	48.5	13.976	-26.01	0.04
LV 20	43.5	11.668	-25.18	0.02
LV 21	40	13.282	-25.71	0.03
LV 22	37.5	14.845	-24.08	0.01
LV 23	36	11.325	-25.96	0.06
LV 24	31.5	11.316	-25.29	0.03
LV 25	26.5	14.271	-26.27	0.05
LV 26	21.5	12.075	-25.27	0.01
LV 27	14	10.774	-25.79	0.03
LV 28	9	11.811	-26.25	0.06
LV 29	4	11.836	-27.51	0.03
LV 30	contact	15.038	-26.01	0.03

Tab. 7.3 Carbon isotope results are here reported for each of the thirty Moroccan samples. So, besides their name and their weight, $\delta^{13}C$ and total carbon data are shown.

The absence of a clear trend for the studied samples collected in the Arganà Valley basin is well visible in Fig. 7.2.

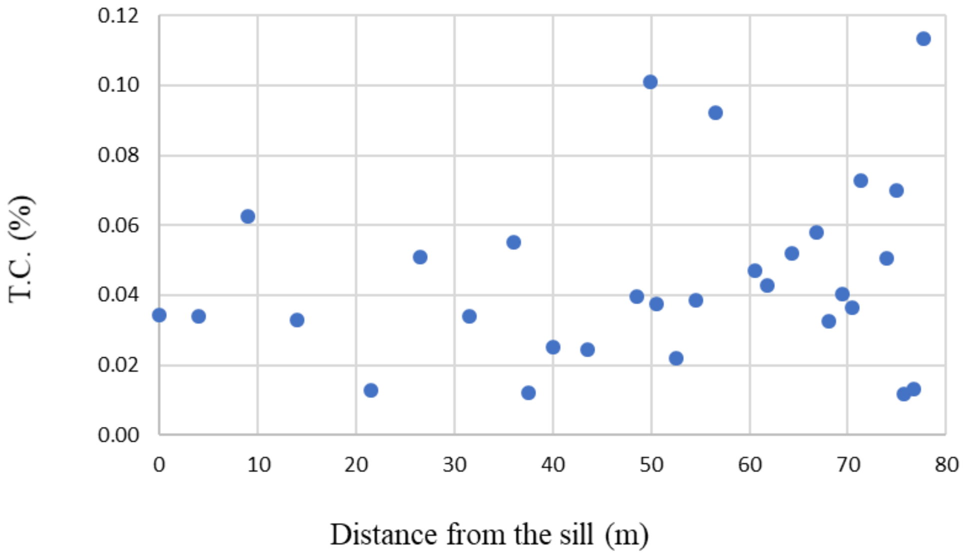

Fig. 7.2 The T.C. values (%) for the Moroccan samples, which correspond to the T.O.C. values (%), are here reported. Note that a clear trend of values increase is not visible.

7.1.3 Geochemical results for American samples

The carbon geochemical analyses on the American samples include carbon isotopes analysis and T.O.C. analysis. As visible in Tab. 7.4, the carbon isotopes results show lighter values than the other two groups of samples (the Moroccan and the Brazilian ones).

Sample	Distance (m)	Weight (mg)	δ^{13}C (VPDB)	TC (%)
LO 37	1.7	6.150	-27.60	Not Measured
LO 38	3.4	7.390	-27.62	Not Measured
LO 39	5.1	8.632	-27.63	Not Measured
LO 40	6.4	6.022	-27.86	Not Measured
LO 41	8.5	6.940	-26.73	Not Measured
LO 42	10.7	6.241	-26.93	Not Measured
LO 43	13.2	7.406	-28.02	Not Measured
LO 44	14	9.678	-27.99	Not Measured
LO 45	17.5	8.268	-27.93	Not Measured
LO 46	20	8.503	-27.55	Not Measured
LO 47	22.3	6.412	-27.70	Not Measured

Tab. 7.4 From left to right: samples name, their distance from the Palisades, their weight for the analyses, their δ^{13}C values, and the TC column, where it is specified that no analyses and estimation for it have been done.

In Tab. 7.5, the T.O.C. values (%) for samples from U.S.A. are illustrated. T.O.C. values appear to be very low (≥ 0.01%) throughout the sampled section. Since the T.O.C. values are very low and close to the analytical detection limit, it has been decided not to repeat the analyses.

The T.O.C. results are still useful for the purpose of this study. By considering that Lockatong Formation, within which the Palisades sill intruded (201.5 Ma) the sill' s thickness (~ 300 m), and the contact aureole thickness (200-240 m; Van Houten, 1971), it is likely that the low T.O.C. values, obtained during this research, are the result of the sill intrusion. This suggests a probable high degassing from the generally quite T.O.C.-rich Lockatong Formation, in the Newark Basin, during sill emplacement.

Furthermore, it is important to remind the distance of the samples from the sill. Their maximum distance is of ca. 22.3 m from the sill: they are very close to the Palisades sill. So, their low T.O.C. values are probably due to their closeness to the sill.

Sample	Distance (m)	Weight (mg)	TOC (%)
LO 37	1.7	9.289	≤ 0.01
LO 37	1.7	6.998	≤ 0.01
LO 38	3.4	12.375	≤ 0.01
LO 38	3.4	7.866	≤ 0.01
LO 39	5.1	8.736	≤ 0.01
LO 39	5.1	6.203	≤ 0.01
LO 40	6.4	9.535	≤ 0.01
LO 40	6.4	6.120	≤ 0.01
LO 41	8.5	7.289	≤ 0.01
LO 41	8.5	8.505	≤ 0.01
LO 42	10.7	7.403	≤ 0.01
LO 42	10.7	9.488	≤ 0.01
LO 43	13.2	6.379	≤ 0.01
LO 43	13.2	5.868	≤ 0.01
LO 44	14	9.976	≤ 0.01
LO 44	14	9.222	≤ 0.01
LO 45	17.5	8.817	≤ 0.01
LO 45	17.5	8.219	≤ 0.01
LO 46	20	7.247	≤ 0.01
LO 46	20	9.425	≤ 0.01
LO 47	22.3	9.436	≤ 0.01
LO 47	22.3	7.240	≤ 0.01

Tab. 7.5 From left to right: samples name, samples distance from the sill, their weight for the T.O.C. analyses and T.O.C. results.

7.2 Vitrinite Reflectance results

Vitrinite reflectance analyses have been conducted on two set of samples: the first one from Brazil (samples named RS) and the second one from Morocco (samples called LV). Each of the two groups were constituted by four samples. The analyses, made at Roma Tre University, have been carried out with the purpose to observe the thermal effect of sills intrusion on the organic matter. Furthermore, these data have been inserted in the input Excel file used as a base for the 1D sill model (Iyer et al., 2017b), developed with the aim to quantify the amount of CO_2 (or in some cases CH_4) released into the atmosphere as a consequence of sills emplacement.

Vitrinite reflectance analyses have not been conducted on the North America samples as their T.O.C. (%) is so low hindering reliable vitrinite reflectance measurements. The same is true for the Brazilian sample RS 11, which yielded too low T.O.C. (Tab. 7.7). It should however be remembered that vitrinite reflectance values (Ro%) do not fall within the compulsory data to be entered in the 1D SILLi model input Excel file (Iyer et al., 2017b).

The data obtained are contained within the following tables (Tab. 7.6 and Tab. 7.7), where vitrinite reflectance results (Ro%) and the calculated standard deviations (stdv Ro%) of each sample are reported:

Sample	Ro%	stdv Ro%
LV 30	0.83	0.18
LV 28	1.01	0.26
LV 25	1.05	0.15
LV 22	1.07	0.21
LV 02	1.53	0.64

Tab. 7.6 From left to right: sample name, vitrinite reflectance values and standard deviation values of each sample.

Sample	Ro%	stdv Ro%
RS 03	1.55	0.59
RS 07	1.01	0.01
RS 11	-	-
RS 15	1.15	0.07
RS 19	1.22	0.19

Tab. 7.7 From left to right: sample name, vitrinite reflectance values and standard deviation values of each sample.

An important observation concerning the trend of vitrinite reflectance values can be made from Tab. 7.6 and Tab. 7.7. In the case of the Moroccan section vitrinite reflectance values are decreasing when approaching the sill. In fact, sample LV 30, collected at the contact with the Amelal sill, yielded apparently relatively high vitrinite reflectance, while sample LV 2, one of the most distant sample from the sill, yielded higher values. Such trend is opposite to the expectation, as vitrinite reflectance values should increase moving towards the sill (remember that vitrinite reflectance values increase with the increase of temperature values). Instead, in the case of Brazilian samples vitrinite reflectance values increase towards the sill contact (samples RS 03 and RS 19 have been taken at a distance from the sill of ~ 0.7 m and ~ 10.7 m, respectively).

The anomalous trend of vitrinite reflectance values of the Moroccan samples can be explained by considering the action of metamorphic fluids. In fact, as shown by Barker et al. (1998) metamorphic fluids (or in general hot fluids) can alter the organic matter and so influence vitrinite reflectance values.

7.3 Rock-Eval analyses results

Rock-Eval analyses have been made at the University of Lausanne in order to constrain the maturity of organic matter. Unfortunately, the organic matter amount in our samples are too low to produce significant data.

Rock-Eval analyses have been carried out only for the Brazilian and the Moroccan samples. In fact, after analyzing these two sets of samples and having seen the results, in light of the values obtained from the carbon geochemical analyses for US samples, it was decided not to continue with this type of analyses even for American samples.

On the other hand, the T.O.C. values obtained from Rock-Eval analyses are very similar to the T.O.C. values obtained from the carbon geochemical analyses, conducted at University of Padova. In Tab. 7.8 and Tab. 7.9 the T.O.C.

results (%) from Rock-Eval analyses are reported.

The T.O.C. results are near-identical in the case of the Brazilian samples. From Tab. 7.9, it is possible to observe a trend of increasing values at increasing distance from the sill. This trend has been already observed in the subparagraph 7.1.1, where it has been suggested that this trend is probably due to the generation and the degassing of gases from organic matter after sill emplacement.

Sample	Distance (m)	TOC (%)
LV 01	77.7	0.04
LV 04	75	0.04
LV 07	70.5	0.01
LV 12	61.8	0.02
LV 16	52.5	0.02
LV 18	49.9	0.03
LV 20	43.5	0.02
LV 22	37.5	0.02
LV 24	31.5	0.01
LV 26	21.5	0.02
LV 27	14	0.01
LV 28	9	0.01
LV 29	4	0.01
LV 30	contact	0.02

Tab. 7.8 Here T.O.C. data from Rock-Eval analyses for Moroccan samples are reported. Samples name and their distance are also shown.

Sample	Distance (m)	TOC (%)
RS 02	0.2	0.01
RS 04	1.2	0.02
RS 06	2.2	0.01
RS 08	3.2	0.02
RS 10	4.2	0.02
RS 12	5.2	0.07
RS 14	6.2	0.07
RS 16	7.7	0.13
RS 18	9.7	0.16
RS 19	10.7	0.23

Tab. 7.9 T.O.C. data from Rock-Eval analyses for the Brazialian are reported. Samples name and their relative distances from sill are presented.

In conclusion, the results reported in Tab. 7.8 and Tab. 7.9 are very important to confirm the validity of the measurements made with the Thermo Scientific Delta V Advantage Isotope Ratio Mass Spectrometer, present at University of Padova. So, they reinforce our tests results on the machine’ s sensitivity.

7.4 XRPD analyses results

In this section the XRPD analysis results for each of the three sedimentary sequences considered during this research are illustrated. Note that, in general, due to the nature of the contact metamorphism in the case of the intrusion of a sill, no important mineralogic evidence of the contact metamorphism has been identified.

7.4.1 XRPD results for the Brazilian samples

In Fig. 7.10 the mineralogical results for the Brazilian sequence are shown. Quartz and muscovite are present in all samples. Anatase is always present in most of the sedimentary sequence, except for samples RS 2 and RS 7. Chlorite is also near-ubiquitous: it is not present only in three samples, RS 03, RS 04 and RS 05.

The presence of goethite is observed only in the first four samples of the succession. Also paragonite is present in some of the first samples of the studied succession (RS 3 through RS 8).

Pyrophyllite, instead, as illustrated from Fig. 7.10, is present in the last thirteen samples of the succession, from sample RS 7 to RS 19.

Kaolinite is present only in a few samples (RS 3, RS 4, RS 12 and RS 17) and its presence is interpreted as resulting from late alteration processes. Finally it should be noted that anorthite is present only in sample RS 2, whereas apatite is present only in sample RS 18 (Fig. 7.10).

Interestingly, goethite and paragonite disappear from the succession just before the appearance of pyrophyllite. A semiquantitative estimation could be useful in order to well understand if there is a relationship between the appearance and the disappearance of these minerals.

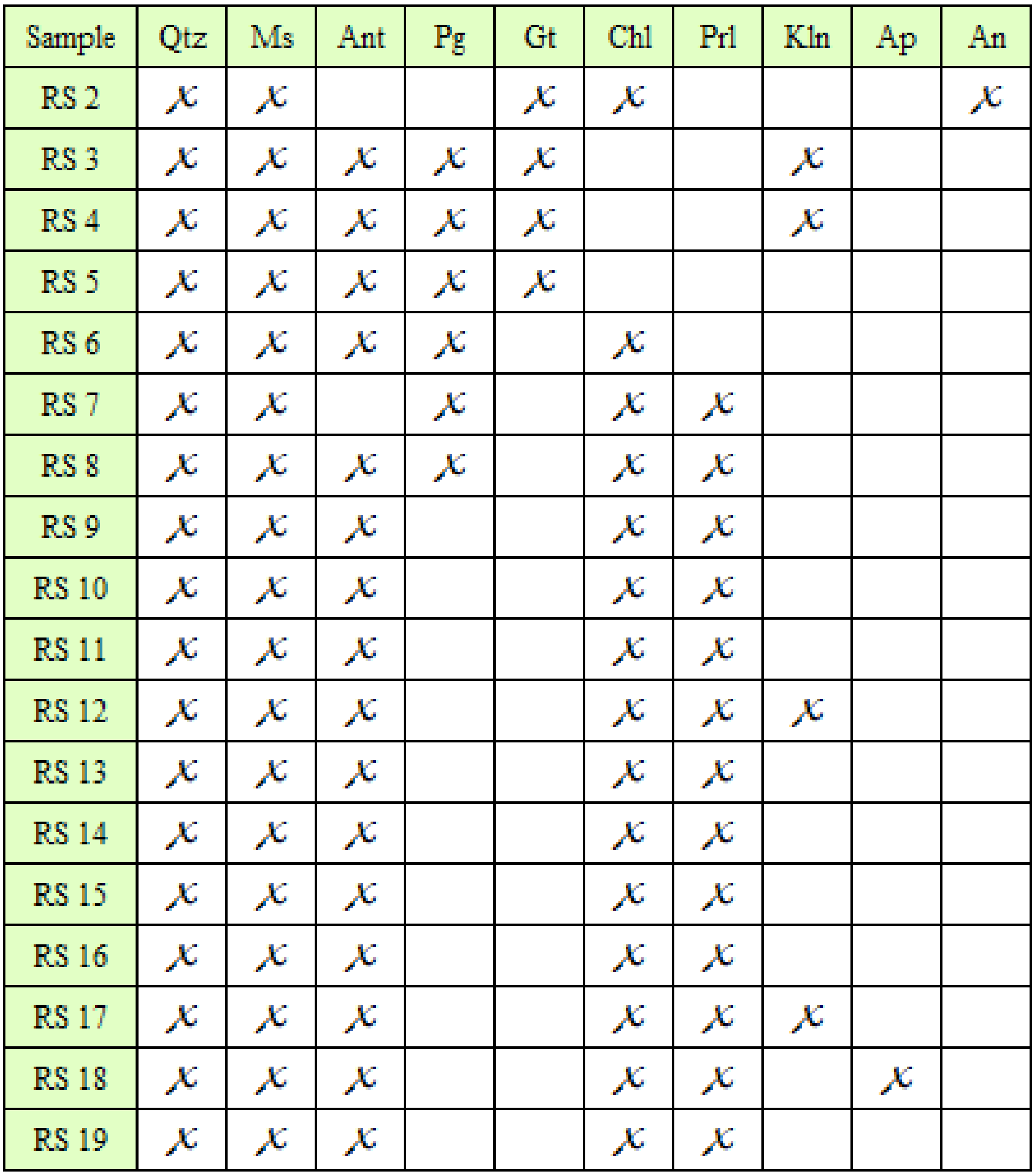

Sample	Qtz	Ms	Ant	Pg	Gt	Chl	Prl	Kln	Ap	An
RS 2	✗	✗			✗	✗				✗
RS 3	✗	✗	✗	✗	✗			✗		
RS 4	✗	✗	✗	✗	✗			✗		
RS 5	✗	✗	✗	✗	✗					
RS 6	✗	✗	✗	✗		✗				
RS 7	✗	✗		✗		✗	✗			
RS 8	✗	✗	✗	✗		✗	✗			
RS 9	✗	✗	✗			✗	✗			
RS 10	✗	✗	✗			✗	✗			
RS 11	✗	✗	✗			✗	✗			
RS 12	✗	✗	✗			✗	✗	✗		
RS 13	✗	✗	✗			✗	✗			
RS 14	✗	✗	✗			✗	✗			
RS 15	✗	✗	✗			✗	✗			
RS 16	✗	✗	✗			✗	✗			
RS 17	✗	✗	✗			✗	✗	✗		
RS 18	✗	✗	✗			✗	✗		✗	
RS 19	✗	✗	✗			✗	✗			

Tab. 7.10 The mineralogical association for the Brazilian samples is illustrated.

7.4.2 XRPD results for the U.S.A. samples

XRPD analyses are reported in Tab. 7.11. In this case the semiquantitative estimate has been made in order to obtain more information concerning the metamorphic effects of sill emplacement on the sedimentary sequence.

<table>
<tr><th rowspan="2">Sample</th><th colspan="2">Mca</th><th rowspan="2">Am</th><th rowspan="2">Ccn</th><th rowspan="2">Pl</th><th rowspan="2">Ne</th><th rowspan="2">Prh</th><th rowspan="2">Ep</th><th rowspan="2">Cal</th><th rowspan="2">Anl</th></tr>
<tr><th>Di</th><th>Tri</th></tr>
<tr><td>LO 37</td><td colspan="2">Di+30</td><td>6</td><td>1</td><td>55</td><td></td><td>4</td><td>0</td><td>?</td><td>4</td></tr>
<tr><td>LO 38</td><td colspan="2">19</td><td>12</td><td>9</td><td>50</td><td>11</td><td></td><td></td><td>?</td><td></td></tr>
<tr><td>LO 39</td><td colspan="2">18</td><td>18</td><td>7</td><td>43</td><td>15</td><td></td><td></td><td></td><td></td></tr>
<tr><td>LO 40</td><td colspan="2">25</td><td>8</td><td>6</td><td>48</td><td>12</td><td></td><td></td><td></td><td></td></tr>
<tr><td>LO 41</td><td colspan="2">16</td><td>14</td><td>6</td><td>47</td><td>15</td><td></td><td></td><td></td><td></td></tr>
<tr><td>LO 42</td><td colspan="2">29</td><td>9</td><td>7</td><td>42</td><td>14</td><td></td><td></td><td>?</td><td></td></tr>
<tr><td>LO 43</td><td colspan="2">23</td><td>6</td><td>10</td><td>49</td><td>13</td><td></td><td></td><td></td><td></td></tr>
<tr><td>LO 44</td><td colspan="2">31</td><td>3</td><td>11</td><td>50</td><td>6</td><td></td><td></td><td></td><td></td></tr>
<tr><td>LO 45</td><td colspan="2">35</td><td></td><td>15</td><td>50</td><td></td><td></td><td></td><td></td><td></td></tr>
<tr><td>LO 46</td><td colspan="2">34</td><td>3</td><td>17</td><td>46</td><td></td><td></td><td></td><td></td><td></td></tr>
<tr><td>LO 47</td><td colspan="2">32</td><td>0</td><td>12</td><td>56</td><td></td><td></td><td></td><td></td><td></td></tr>
</table>

Tab. 7.11 In the table the results of the XRPD analyses, conjunct to the semiquantitative estimate, for the American samples are illustrated. Note that Di = dioctahedral micas and Tri = trioctahedral micas. The question mark reported in the table are due to the fact that from XRPD analyses minerals, as i.e. calcite, have been identified, but from the semiquantitative estimate they have not been found.

As it is possible to observe from Tab. 7.11, the nearest sample to the sill (LO 37) shows the presence of analcime and prehnite. The presence of epidote and calcite in this sample is not well constrained. Note that sample LO 37 is probably the only sample containing dioctahedral micas. The mineralogical association of sample LO 37 is most likely due to the metamorphic effects of sill intrusion. Nepheline and cancrinite are not found at the contact with the sill. Their first occurrence happens in sample LO 38, taken at a distance of 4 m from the sill. Another interesting observation is always concerning the nepheline-cancrinite association. From Tab. 7.11, it is possible to note that when nepheline is present in the sample, cancrinite values are low, whereas cancrinite percentage increase when nepheline disappears. This is observable especially in the last four samples of the studied sedimentary succession. Note that cancrinite is a reaction product of nepheline.

Noteworthy is the absence of the quartz from the mineralogical association visible in Tab. 7.11. This absence is considered to be due to the autochthonous origin of the rocks. This hypothesis is supported also by the great presence of phyllosilicates, interpreted to be mainly biotite.

In order to well understand the metamorphic effects of Palisades sill on the surrounding sedimentary successions, another sedimentary succession has been studied (Tab. 7.12).

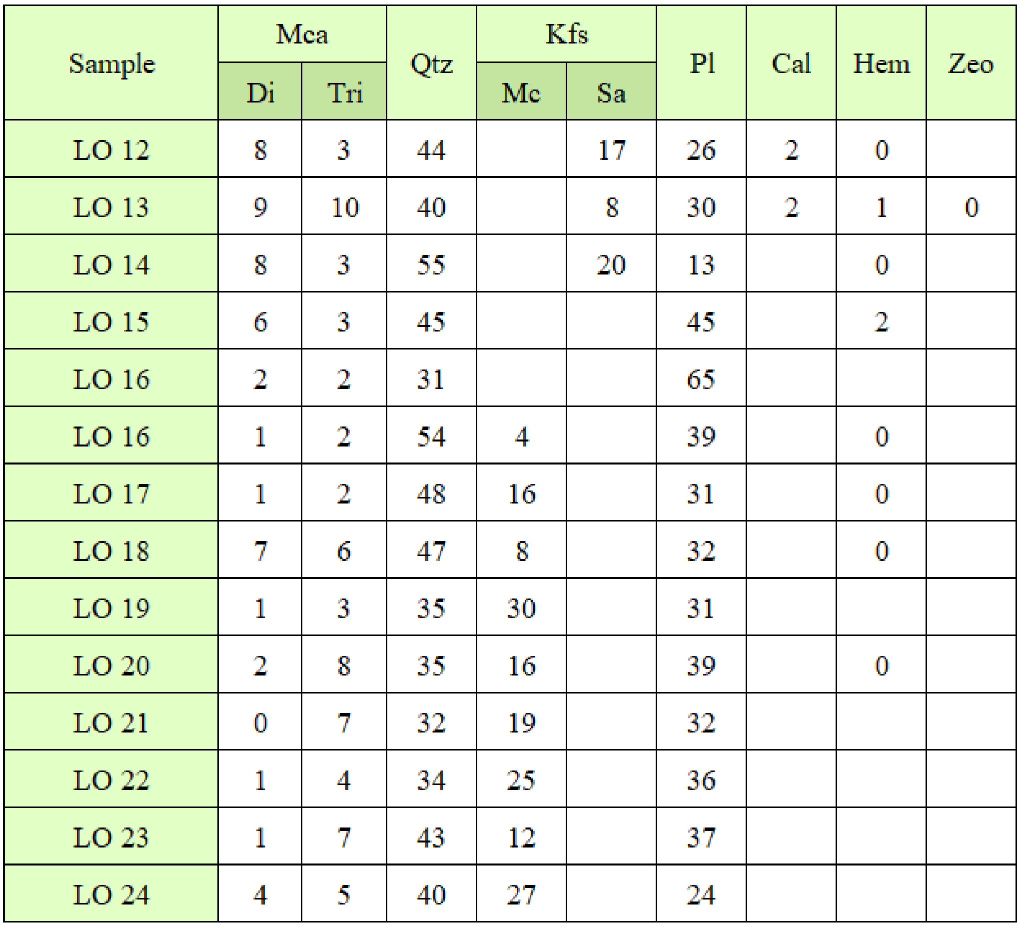

Sample	Mca		Qtz	Kfs		Pl	Cal	Hem	Zeo
	Di	Tri		Mc	Sa				
LO 12	8	3	44		17	26	2	0	
LO 13	9	10	40		8	30	2	1	0
LO 14	8	3	55		20	13		0	
LO 15	6	3	45			45		2	
LO 16	2	2	31			65			
LO 16	1	2	54	4		39		0	
LO 17	1	2	48	16		31		0	
LO 18	7	6	47	8		32		0	
LO 19	1	3	35	30		31			
LO 20	2	8	35	16		39		0	
LO 21	0	7	32	19		32			
LO 22	1	4	34	25		36			
LO 23	1	7	43	12		37			
LO 24	4	5	40	27		24			

Tab. 7.12 XRPD results, integrated with the semiquantitative estimation, are shown. Note that in some cases, by interpreting the diffractograms, some minerals appear to be present in the mineralogical association, but, by making the semiquantitative estimation, their presence has not been confirmed.

From Tab. 7.12, it is possible to notice the presence within the sedimentary succession of two different types of K-feldspar: both microcline and sanidine appear in the succession in relation to the distance from the sill. Sanidine, the high temperature polymorph, is present in the first three samples (LO 12, LO 13, LO 14). Microcline, the polymorph of low temperature, appears in the other samples, from LO 17 to LO 24. This is the most evident metamorphic effects of the sill emplacement. The transition between the sanidine domain and the microcline one is highlighted by the fact that in sample LO 15 and LO 16 no alkali-feldspar appears, while the amount of plagioclase increases from 13% in LO 12-LO 14 to 45% in LO 15 or 65% in LO 16 (Tab. 7.12). Phyllosilicates contents are very variable, but the first four samples are similar. In fact, LO 12, LO 13. LO 14 and LO 15 show the presence of dioctahedral phyllosilicates, such as, for instance, smectite.

7.4.3 XRPD results for the Moroccan samples

The XRPD analyses results integrated with the semiquantitative estimates are reported in Tab. 7.13. Remembering that sample LV 30 is the closest to the sill, some interesting trends can be observed.

Towards the sill, an increase in hematite and in K-feldspar is visible. Hematite is the reaction product of phyllosilicates containing Fe^{2+}, as chlorite. From the semiquantitative estimates chlorite seems to decrease by approaching the sill, being replaced partially by hematite.

Orthoclase is present only in the sample closest to the sill (LV 30), while microcline, the polymorph of low temperature, is present in the other samples (Fig. 7.3). This would suggest that at the contact with the sill a greater temperature was reached.

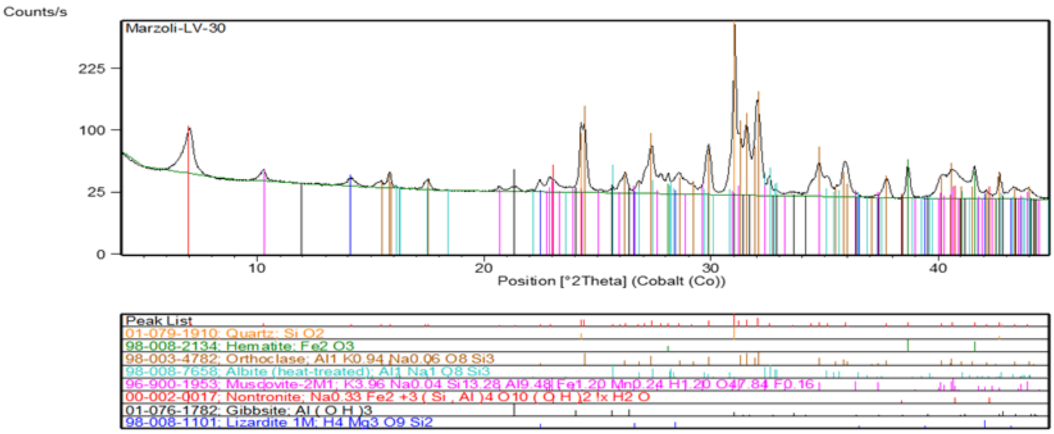

Fig. 7.3 The diffractogram of the sample LV 30 is here illustrated. Note the orthoclase peaks, and the nontronite peaks.

From (Fig. 7.3), it is also possible to observe the presence of the nontronite, a clay mineral belonging to the smectite group. Its well-defined peak is the first one from the left on the diffractogram (Fig. 7.3). By moving away from the sill this mineral disappears from sample LV 27, sample from which, instead, chlorite begins to appear. So, probably nontronite formation is linked to the effects of the sill emplacement. Probably, the formation of this mineral occurred at a later time with respect to the orthoclase formation and is probably linked to a hydrothermal activity that may have taken place during the cooling stage of the sill.

Other variations observable from Tab. 7.13 are concerning the trend of minerals as calcite, dolomite, quartz and plagioclase. Calcite and dolomite disappear by approaching the sill, even though their presence does not appear to be constant throughout the various samples.

Also quartz and plagioclase values decrease towards the sill. Particularly, even if plagioclase seems to appear in the diffractogram of sample LV 30, its presence has not been confirmed by the semiquantitative estimation (Tab. 7.13).

So, in the case of the Moroccan samples the metamorphic effects of the sill emplacement are principally traceable to the presence of orthoclase, the increase of hematite and nontronite and the decrease of chlorite close to the sill.

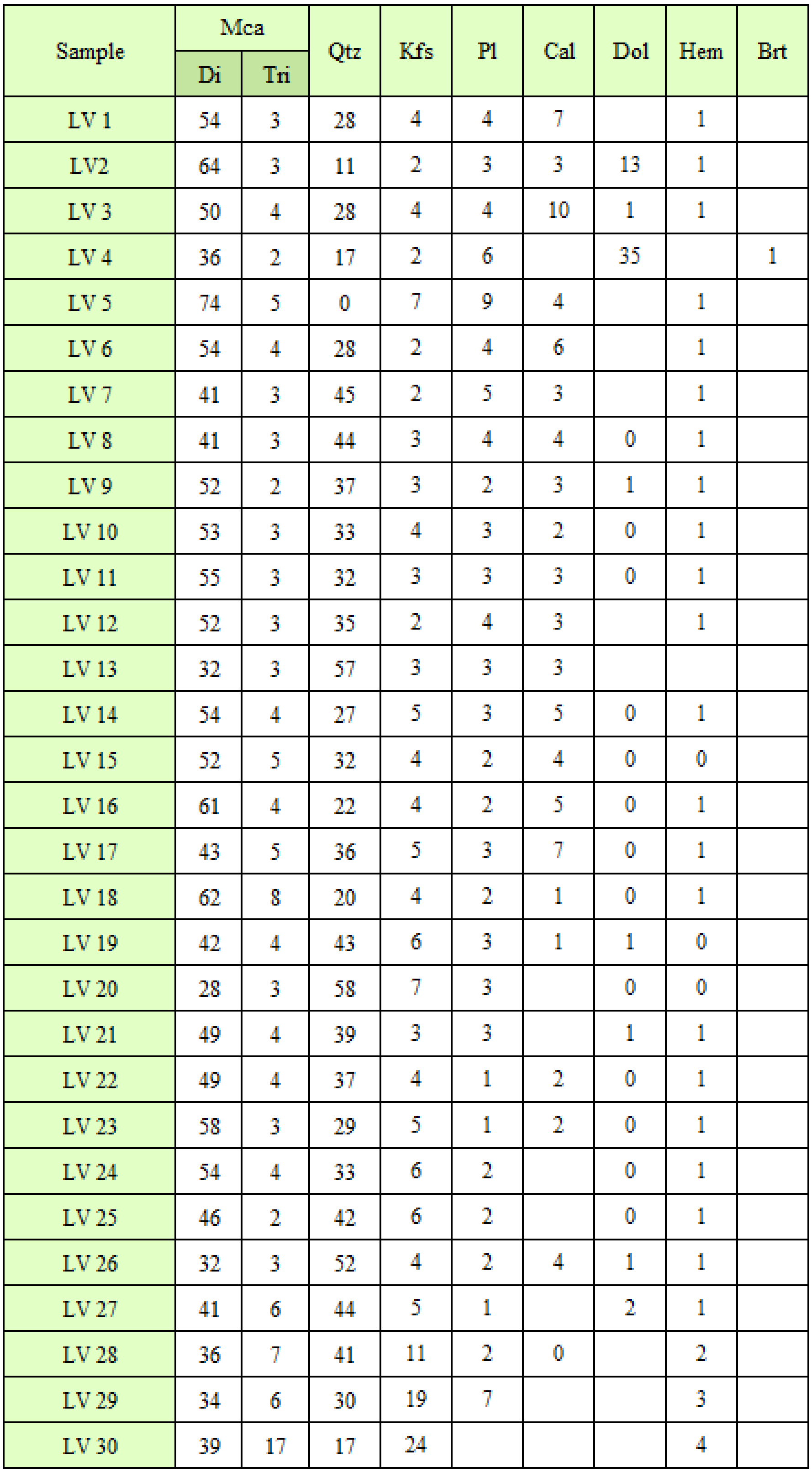

Sample	Mca		Qtz	Kfs	Pl	Cal	Dol	Hem	Brt
	Di	Tri							
LV 1	54	3	28	4	4	7		1	
LV2	64	3	11	2	3	3	13	1	
LV 3	50	4	28	4	4	10	1	1	
LV 4	36	2	17	2	6		35		1
LV 5	74	5	0	7	9	4		1	
LV 6	54	4	28	2	4	6		1	
LV 7	41	3	45	2	5	3		1	
LV 8	41	3	44	3	4	4	0	1	
LV 9	52	2	37	3	2	3	1	1	
LV 10	53	3	33	4	3	2	0	1	
LV 11	55	3	32	3	3	3	0	1	
LV 12	52	3	35	2	4	3		1	
LV 13	32	3	57	3	3	3			
LV 14	54	4	27	5	3	5	0	1	
LV 15	52	5	32	4	2	4	0	0	
LV 16	61	4	22	4	2	5	0	1	
LV 17	43	5	36	5	3	7	0	1	
LV 18	62	8	20	4	2	1	0	1	
LV 19	42	4	43	6	3	1	1	0	
LV 20	28	3	58	7	3		0	0	
LV 21	49	4	39	3	3		1	1	
LV 22	49	4	37	4	1	2	0	1	
LV 23	58	3	29	5	1	2	0	1	
LV 24	54	4	33	6	2		0	1	
LV 25	46	2	42	6	2		0	1	
LV 26	32	3	52	4	2	4	1	1	
LV 27	41	6	44	5	1		2	1	
LV 28	36	7	41	11	2	0		2	
LV 29	34	6	30	19	7			3	
LV 30	39	17	17	24				4	

Tab. 7.13 The XRPD analyses results, integrated with the semiquantitative estimation, for the Moroccan samples.

7.5 SEM analyses results

SEM analyses were conducted only on the Brazilian samples in order to try to identify some minerals useful for estimating metamorphic temperature. One of the minerals that has been searched through SEM analysis is biotite. SEM analyses have been conducted on several samples, particularly on sample RS 02.

Sample RS 02 contains the contact between the sedimentary rocks and a vein of basaltic melt, i.e. an apophysis of the main sill, whose position is located at about 30-50 cm from RS 02. The SEM analysis confirms the presence of chlorite, quartz and anatase as the main phases of the sedimentary rock. Traces of probable graphite within chlorite crystals (Fig. 7.4) have been observed as well. The actual presence of graphite needs confirmation trough Raman analysis.

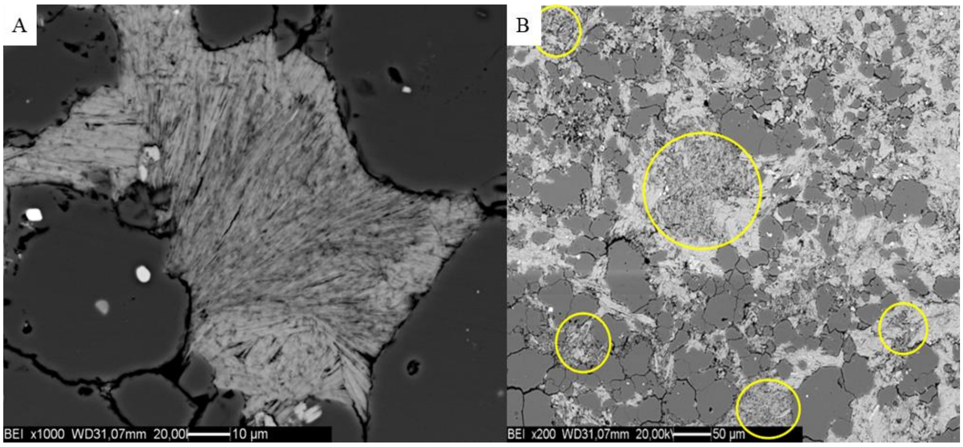

Fig. 7.4 SEM images for the thin section RS 02: A) a crystal of chlorite containing a second phase, considered to be graphite, with all around quartz; B) An overview of the thin section, where it is possible to observe the presence of the second within the chlorite (circled in yellow).

The basaltic vein contains relatively large crystals of plagioclase and alterated olivine, as well as micro-crystalline quartz, chlorite (replacing olivine) and sulphides (chalcopyrite). The basalt matrix is mainly constituted by chlorite, quartz and plagioclase. Chlorite occurs in two forms, one more ferriferous and one less ferriferous.

A vein, visible in thin section (Fig. 7.5) and originating from the contact with the sediment, contains quartz, biotite and probably ilmenite.

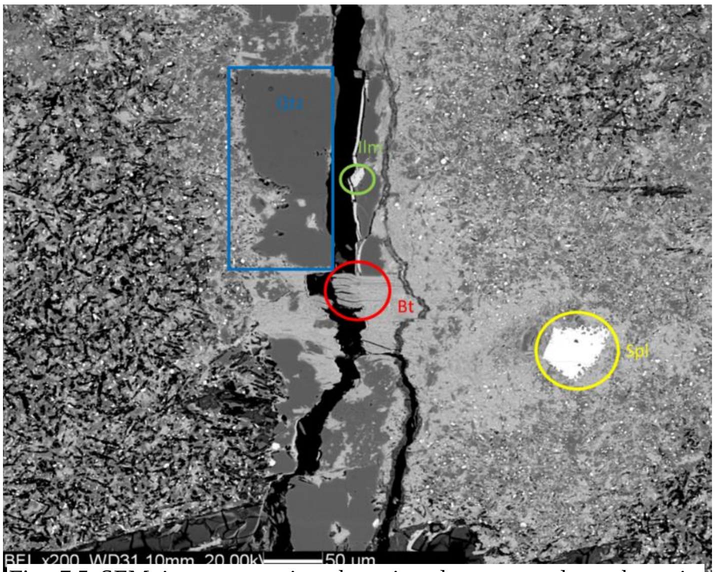

Fig. 7.5 SEM image reporting the minerals present along the vein. Quartz, biotite and ilmenite are visible. On the right side of the image a spinel is present, circled in yellow.

7.6 SILLi model results

7.6.1 Model results for Amazonas samples

The result tab obtained from the SILLi model for the Amazonas basin study case is shown in Fig. 7.6. The first graph in Fig. 7.6 shows the geothermal gradient (°C). The second one shows the vitrinite reflectance curve, whereas the third panel shows the T.O.C. content curve and the fourth one shows the T_{max} trend. The last two panels show respectively the pressure variation with depth (MPa) and the quantity of CO_2 of organic origin (kg/m^3) produced after sill emplacement. The charts of vitrinite reflectance (%Ro), T.O.C. content (wt%), T_{max} (°C) and the organic origin CO_2 produced (kg/m^3) are of particular interest to this study.

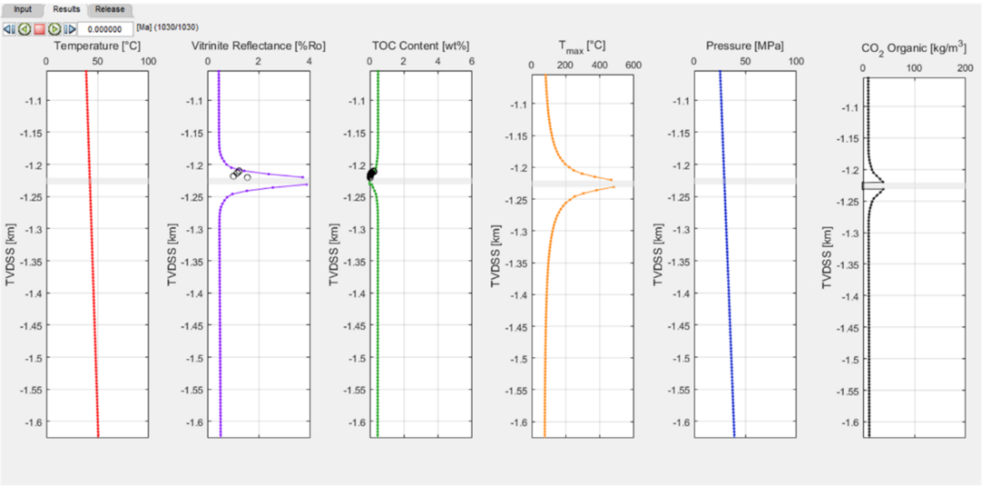

Fig. 7.6 The result tab for the Amazonas basin study case is here reported. The intrusion thickness is ca. 10 m and its emplacement temperature is of 1100°C.

As it is possible to observe in Fig. 7.6, the vitrinite reflectance values (%Ro) obtained from the analyses increase moving towards the sill. This trend is confirmed by the vitrinite reflectance curve calculated from the model. The T_{max} graph (Fig. 7.6) shows that the temperature increases progressively towards the sill. The maximum temperature estimated from the model is ca. 480-490 °C at the contact with the sill.

The T.O.C. content trend is opposite to the vitrinite reflectance trend and the T_{max} curve (Fig. 7.6). The T.O.C values (wt%) decrease by approaching the sill. From Fig. 7.6, it is possible to observe that the TOC curve modelled from the used 1D model fits very well the values obtained from the analyses.

All these trends suggest that the sill intrusion had a great influence on the evolution of the organic matter. The model indicates that sill emplacement causes degassing of CO_2 generated from the breakdown of the organic matter due to the increased temperatures. As visible from the graph of the produced organic CO_2 (kg/m^3; Fig. 7.6), the maximum amount of CO_2 produced by sill emplacement is ca. 40-45 kg/m^3 at the sill contact. The cumulative quantity of CO_2 originating from the organic matter and released into the atmosphere during intrusion of the sill equals ca. 42 ton/m^2 (Fig. 7.7).

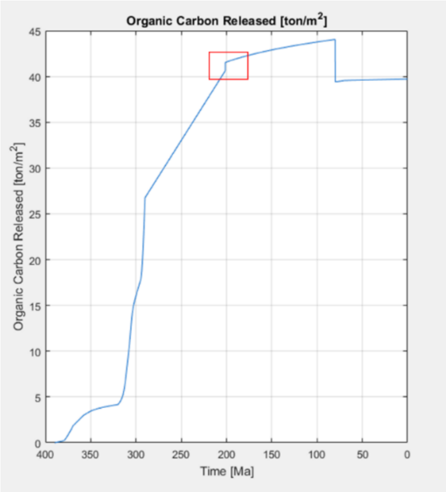

Fig. 7.7 Graph illustrating the amount of organic origin CO_2 released into the atmosphere in the history of Amazonas basin. In the rectangle the CO_2 amount released consequently sill emplacement is highlighted.

7.6.2 Model result for the Moroccan samples

SILLi model has also been applied to the Arganà Valley basin (Fig. 7.8). The vitrinite reflectance curve, modelled from the 1D model, is not consistent with the vitrinite reflectance results (%Ro) obtained during the research, confirming that the measured vitrinite reflectance values are affected by secondary processes, such as percolation of hot fluids or metamorphic fluids. The modelled T.O.C. content (wt%) lowers when approaching the sill, as expected, while the T_{max} (°C) increases towards the sill. The maximum temperature reached, estimated from the model, is ca. 650 °C above the sill and ca. 700 °C below the sill.

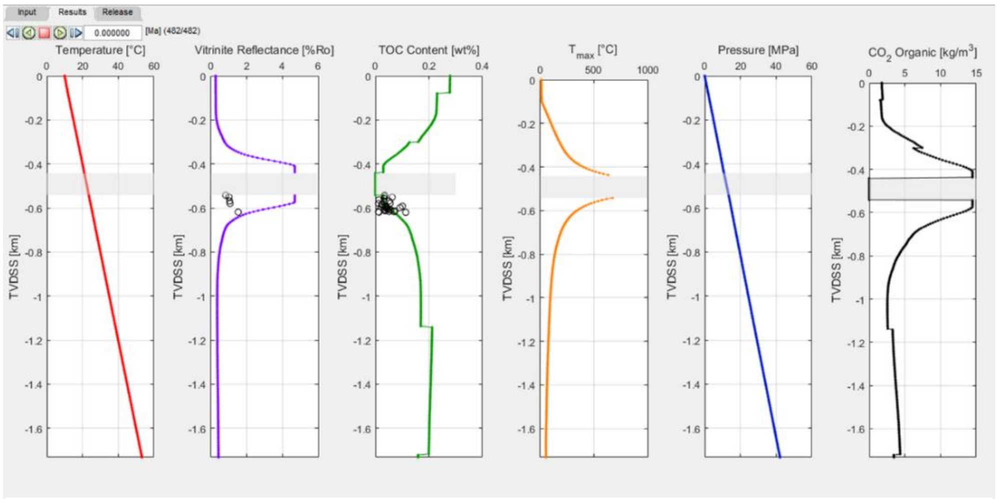

Fig. 7.8 The result tab for the Moroccan basin study case is here reported. The intrusion thickness is ca. 100 m and its emplacement temperature is of 1100°C.

As visible in Fig. 7.8, the production of organic origin CO_2 also increases towards the sill with a maximum peak of ~ 15 kg/m^3 at the contact with the sill. The cumulative amount of organic CO_2 released into the atmosphere (Fig. 7.9) is much lower than the Brazilian case and is ca. 7 ton/m^2.

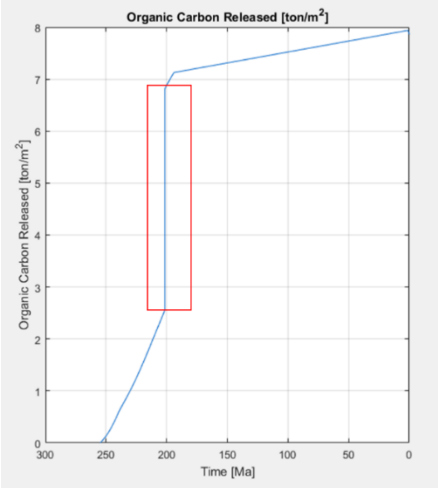

Fig. 7.9 Graph illustrating the amount of CO_{2org} released into the atmosphere in the history of Arganà Valley basin. In the rectangle the CO_2 amount released as sill emplacement consequence is highlighted.

7.6.3 Model result for the U.S.A. study case

The model results for the Newark basin study case are reported in Fig. 7.10.

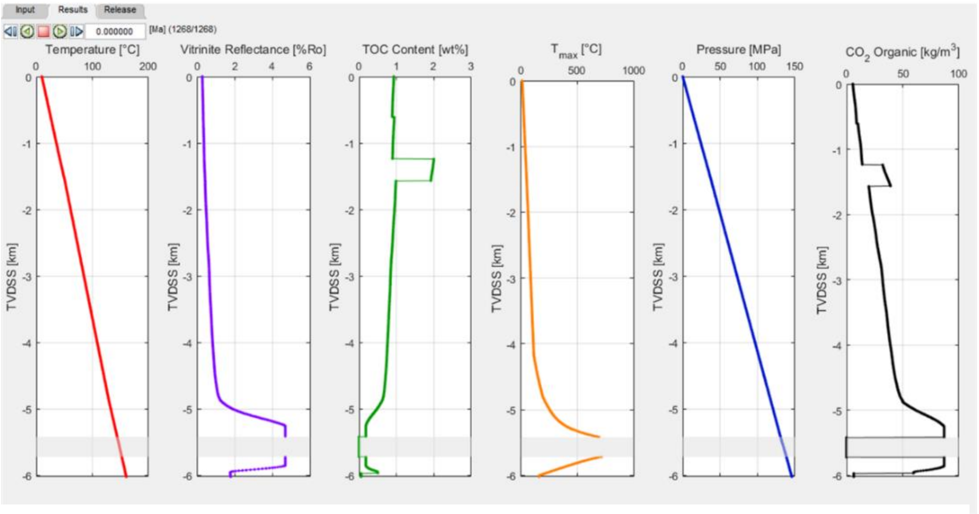

Fig. 7.10 The result tab for the Newark basin study case is here reported. The intrusion thickness is ca. 300 m and its emplacement temperature is of 1100°C.

The U.S.A sequence shows modeled results similar to the Brazilian one for the trend of vitrinite reflectance values (Ro%), the T.O.C. content (wt%) and T_{max} values (°C). So, as visible from the second panel, the modeled vitrinite reflectance curve shows an increase of vitrinite reflectance values (%Ro) by approaching the sill. This seems to be concordant with the visible increase of the T_{max} (°C) towards the sill (see the fourth panel, Fig. 7.10). The model estimated maximum temperature reached at the contact with the sill is ca. 700 °C. The modeled T.O.C. content (wt%; Fig. 7.10) decreases toward the sill. The Lockatong formation presents an average T.O.C. of 1.21% (its T.O.C. ranges from 0.5% to 2.72%) and, in the immediate proximity of the sill, a model estimated value of ~ 0.2% is reached.

All three of these trends suggest that a likely and strong degassing occurred after sill emplacement from the Lockatong formation sediments. The maximum peak of production of organic CO_2 is recorded at the contact with the sill and is equal to

~ 85 kg/m^3.

The amount of cumulative CO_2 produced and released because of sill emplacement is shown in Fig. 7.11. The cumulative amount of organic origin CO_2 released from the contact aureole generated from Palisades sill intrusion is equal to a maximum value of ~ 127 ton/m^2 of CO_2.

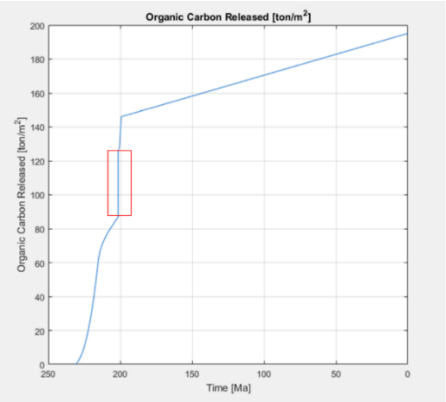

Fig. 7.11 Graph illustrating the amount of organic origin CO_2 released into the atmosphere in the history of Newark Basin. In the rectangle the CO_2 amount released consequently sill emplacement is highlighted.

8 Conclusions

From the geochemical analyses conducted on the samples collected in three different basins (Arganà valley, Morocco; Amazonas basin, Brazil; Newark basin, U.S.A.) it is possible to observe the effects of sill emplacements on the organic matter. By observing the T.C. (wt %) and the T.O.C. (wt %) contents in the Brazilian samples, it is possible to notice an increase of these values at increasing distance from the sill. In the case of the analyzed U.S.A. samples, instead, very low T.O.C. values are visible throughout the studied sedimentary succession. Probably, both the Brazilian samples T.O.C. trend and the U.S. low T.O.C. values are due to the thermal metamorphic action of the sill intrusions on the organic matter. So, a CO_2 degassing from the sediments occurred as a consequence of sill intrusions.

In the study case of the Amelal sill, outcropping in the southern portion of the Arganà Valley, no trend is visible and the T.O.C. values (wt %) are low and variable: they range from 0.01 % to 0.11%. As previously discussed in the subparagraph 7.1.2., the Amelal sill would not seem to have greatly influenced the underlying sedimentary sequence. This fact has been confirmed by the 1D sill model developed during this research for the three study. For the Moroccan study case the estimated cumulative organic origin CO_2 released into the atmosphere is equal to ~ 7 ton/m^2. This low amount of released CO_2 is due to the low initial T.O.C. values characterizing the Bigoudine Formation.

In the other two cases, the quantity of CO_{2org} released into the atmosphere is larger: in the case of the Brazilian sill the amount of CO_{2org} released is ~ 42 ton/m^2, whereas in the case of the U.S.A. sill the amount of CO_{2org} released into the atmosphere is ~ 127 ton/m^2.

Taking into account the thickness of the sills, it can be noticed that a thick sill does not necessarily produce a quantity of gas larger than a thin sill: the Brazilian sill, which has an estimated thickness of about 10 m, produced an amount of CO_2 six times larger than the Amelal sill (Morocco), according to the model results.

So, the amount of organic origin CO_2 produced after the sill emplacement also depends on the initial organic carbon content in the rocks.

Upscaling the amount of organic CO_{2org} produced by the emplacement of the Palisades sill (Newark Basin) and the Brazilian sill, it results that the total amount of CO_{2org} produced in the case of Palisades sill is equal to 204 Gt, whereas in the case of the Amazonas sill produced ca. 24 Gt of CO_{2org} for an estimated area of 500 km^2.

For the Brazilian study case it should be recalled that a lot of sills intruded 201.525 ± 0.065 Ma (Davies et al., 2017) not only in the Amazonas basin, but also in the Solimões basin. Heimdal et al. (2017) estimated that a total amount of 34,000 Gt of organic origin CO_2 was released from the Amazonas and the Solimões basins. Particularly, they estimated that a total amount of 73,000 Gt of CO_2 of both organic origin and inorganic origin was released into the atmosphere. Such high CO_2 production from the two Brazilian basins would therefore have greatly contributed to the end-Triassic carbon cycle perturbations. The Brazilian basins may have not been the only ones to produce such a quantity of CO_2: in fact a similar volume of sills is present in Guinea.

The importance of the other eastern North America (eastern Canada to southeastern U.S.A.) as well as European (Pyrenees), and other South America (Parnaiba, Bolivia) basins should not be forgotten.

The current concentration of CO_2 in the atmosphere is equivalent to 403 ppm corresponding to ca. 3000 Gt of CO_2 (for a total mass of the atmosphere of ca. 5 x 10^{18} kg). The amount of CO_2 released this year 2017 into the atmosphere because of the human activity is about 41 Gt; in 2013 this quantity was equivalent to 33.5 Gt of CO_2.

The comparison with the current CO_2 data suggests the importance of the CO_2 emissions related to sills or dikes emplacement within organic rich sediments occurred at the Tr-J boundary, thus highlighting their influence on the climate. Before the end-Triassic crisis, the atmospheric CO_2 concentration was probably ca. 1000 ppm, corresponding to ca. 8000 Gt.

Note that the CO_2 emissions related to the sill intrusions are not the only ones occurred at the end of the Triassic. The release of CO_2 from basaltic lava flow and the probable degassing from the destabilization of clathrates have to be remembered. In this context, the carbon cycle perturbations and the disturbance on the climate and on the environment, with the linked mass extinction, could be explained and associated with CAMP activity.

References

Aarnes I., Podladchikov Y., Svensen H., 2012. *Devolatilization-induced pressure build-up: Implications for reaction front movement and breccia pipe formation*. Geofluids, 12, pp. 265-279.

Aarnes I., Svensen H., Polteau S., Planke S., 2011a. *Contact metamorphic devolatilization of shales in the Karoo Basin, South Africa, and the effects of multiple sill intrusions*. Chemical Geology, 281, pp.181-194.

Aarnes I., Fristad K., Planke S., Svensen H., 2011b. *The impact of host-rock composition on devolatilization of sedimentary rocks during contact metamorphism around mafic sheet intrusions*. Geochemistry, Geophysics, Geosystems, 12, Q10019, doi: 10.1029/2011GC003636.

Aarnes I., Svensen H., Connolly J. A. D., Podladchikov Y., 2010. *How contact metamorphism can trigger global climate changes: Modeling gas generation around igneous sills in sedimentary basins*. Geochimica et Cosmochimima Acta, 74, pp. 7179-7195.

Allen P. A. and Allen J. R., 2014. *Basin Analysis: Principles and Application to Petroleum Play Assessment*. Wiley-Blackwell Publishing, pp. 619.

Ash S., 1986. *Fossil plants and the Triassic-Jurassic boundary*. In: Padian K. (Ed), The beginning of the Age of Dinosaurs, Cambridge University Press, Cambridge, pp. 432.

Barker C. E., Bone Y., Lewan M. D., 1998. *Fluid inclusion and vitrinite-reflectance geothermometry compared to heat-flow models of maximum paleotemperature next to dikes, western onshore Gippsland Basin, Australia*. Internal Journal of Coal Geology, 37, pp. 73-111.

Behar F., Beaumont V., De B. Penteado H. L., 2001. Rock-Eval 6 Tecnology: Performances and Developments. Oil and Gas Science and Technology – Rev. IFP, 56, pp. 111-134.

Bertrand H., Fornari M., Marzoli A., García-Duarte R., Sempere T., 2014.*The Central Atlantic Magmatic Province extends into Bolivia*. Lithos, 188, pp. 33-43.

Bertrand H., 1991. *The Mesozoic tholeiitic province of Northwest Africa: a volcano-tectonic record of the early opening of Central Atlantic*. In: Kampunzu, A.B., Lubala, R.T., (Eds), Magmatism in Extensional Structural Settings, The Phanerozoic African Plate, Springer-Verlag, 147-191.

Blackburn T. J., Olsen P. E., Bowring S. A., McLean N. M., Kent D. V., Puffer J., McHone G., Rasbury E. T., Et-Touhami M., 2013. *Zircon U-Pb Geochronology Links the End-Triassic extinction with the Central Atlantic Magmatic Province*. Science, 340, pp. 941-944.

Bryan S. E., Peate I. U., Peate D. W., Self S., Jerram D. A., Mawby M. R., Marsh J.S., Miller J. A., 2010. *The largest volcanic eruptions on Earth*. Eart-Science Reviews, 102, pp. 207-229.

Cainelli C. and Mohriak W. U., 1999. *Some remarks on the evolution of sedimentary basins along the eastern Bralizian continental margin*. Episodes, 22, pp. 206-216.

Callegaro S., Rigo M., Chiaradia M., Marzoli A., 2012. *Latest Triassic marine Sr isotopic variations, possible causes and implications*. Terra Nova, 24, pp. 130-135.

Clemente P., 2014. *Petroleum geology of the Campos and Santos basins, Lower Cretaceous Brazialian sector of the South Atlantic margin*. CERE (Center for Energy Resources Engineering) internal report.

Cohen A.S., and Coe, A.L., 2002. *New geochemical evidence for the onset of volcanism in the Central Atlantic magmatic province and environmental change at the Triassic-Jurassic boundary*. Geology, 30, pp. 267–270.

Coplen T.B., Brand W. A., Gehre M., Gröning M., Meijer H. A. J., Toman B., Verkouteren R. M., 2006. *New Guidelines for* ^{13}C *Measurements*. Analytical Chemistry, 78, pp. 2439-2441.

Cunha P. R. C., Melo J. H. G., da Silva O. B., 2007. *Bacia do Amazonas*. Boletim do Geociencias da Petrobas, 15, pp. 227-251.

Dal Corso J., Schmidt A. R., Seyfullah L. J., Preto N., Ragazzi E., Jenkyns H. C., Delclòs X., Néraudeau D., Roghi G., 2017. *Evaluating the use of amber in palaeoatmospheric reconstructions: The carbon-isotope variability of modern and Cretaceous conifer resins*. Geochimica et Cosmochimica Acta, 199, pp. 351-369.

Dal Corso J., Marzoli A., Tateo F., Jenkyns H. C., Bertrand H., Youbi N., Mahmoudi A., Font E., Buratti N., Cirilli S., 2014. *The dawn of CAMP volcanism and its bearing on the end-Triassic carbon cycle disruption*. Journal of the Geological Society, 171, pp. 153-164;

Davies J. H. F. L., Marzoli A., Bertrand H., Youbi N., Ernesto M., Schaltegger U., 2017. *End-Triassic mass extinction started by intrusive CAMP activity*. Nature communications, 8, article number 15596.

Delaney P.T., Pollard D.D., Ziony J.I., McKee E.H., 1986. *Field relations between dikes and joints: Emplacement processes and paleostress analysis*. Journal of Geophysical Research: Solid Earth, *91,* pp. 4920–4938.

Fedosh M. S. and Smoot J. P., 1988. *A cored stratigraphic section through the northern Newark Basin, New Jersey*. In Froelich A. J. and Robinson G. R. (Eds.), Studies of the Early Mesozoic Basins of the Eastern United States. U.S. Geological Survey Bulletin, 1776, pp. 19-24.

Filho A. T., Mizusaki A. M. P., Antonioli L., 2008. *Magmatism and petroleum exploration in the Brazilian Paleozoic basins*. Marine and Petroleum Geology, 25, pp. 143-151.

Galushkin Y. I., 1997. *Thermal effects of igneous intrusions on maturity of organic matter: A possible mechanism of intrusion*. Organic Geochemistry, 26, pp. 645-658.

Gonzaga F. G., Countinho L. F. C., Gonçalves F. T. T., 2000. *Petroleum geology of the Amazonas Basin, Brazil: modeling of hydrocarbon generation and migration.* In Mello M. R. and Katz B. J. (Eds), Petroleum systems of South Atlantic margins. AAPG Memoir 73, pp. 159-178.

Guex J., Bartolini A., Taylor D., Atudorei V., Thelin P., Bruchez S., Tanner L., Spencere L., 2009. *Comment on: "The organic carbon isotopic and paleontological record across the Triassic-Jurassic boundary at the candidate GSSP section at Ferguson Hill, Muller Canyon, Nevada, USA" by Ward et al., 2007*. Palaeogegraphy, Palaeoclimatology, Palaeoecology, 273, pp. 200-204.

Guex J., Bartolini A., Atudorei V., Taylor D., 2004. *High-resolution ammonite and carbon isotope stratigraphy across the Triassic-Jurassic boundary at New York Canyon (Nevada)*. Earth and Planetary Science Letters, 225, pp. 29-41.

Hallam A., Wignall P. B., 1997. *Mass Extinctions and their Aftermath*. Oxford University Press, Oxford, pp. 320.

Hallam A. and Goodfellow W. D, 1990. *Facies and geochemical evidence bearing on the end-Triassic disappearance of the Alpine reef ecosystems*. Historical Biology, 4, pp. 131-138.

Hansen H. J., 2006. *Stable isotopes of carbon from basaltic rocks and their possible relation to the atmospheric isotope excursion*. Lithos, 92, pp. 105-116.

Hanson R. B. and Barton M. D., 1989. *Thermal development of low-pressure metamorphic belts: results from two-dimensional numerical models*. Journal of Geophysical Research, 94, pp.10363-10377.

Heimdal T. H., Svensen H. H., Ramezani J., Iyer K., Pereiro E., Rodrigues R., Jones M. T., Callegaro S., 2017. Large-scale sill emplacement in Brazil as a trigger for the end-Triassic crisis. Scientific report; In Press..

Hillebrandt A., Krystyn L., Kürschner W.M., Bonis N.R., Ruhl M., Richoz S., Schobben M. A. N., Urlichs M., Bown P.R., Kment K., McRoberts C.A., Simms M., Tomãsových A., 2013. *The Global Stratotype Sections and Point (GSSP) for the base of the Jurassic System at Kuhjoch (Karwendel Mountains, Northern Calcareous Alps, Tyrol, Austria).* Episodes, 36, pp. 162-198.

Hoefs J., 1973 . *Stable Isotope Geochemistry*. Springer-Verlag, pp. 142.

Hofmann A., Tourani A., Gaupp R., 2000. *Cyclicity of Triassic to Lower Jurassic continental red beds of the Argana Valley, Morocco: implications for palaeoclimate and basin evolution.* Palaeogeography, Palaeoclimatology, Palaeoecology, 161, pp. 229-266.

Holness M. B., Dane K., Sides R., Richardson C., Caddick M., 2005. *Melting and melt segregation in the aureole of the Glenmore Plug, Ardnamurchan*. Journal of metamorphic petrology, 23, pp. 29-43.

Hunt J. M., 1996. *Petroleum Geochemistry and Geology*. W. H. Freeman and Company, pp. 617

Iyer K., Schmid D. W., Planke S., Millet J., 2017a. *Modelling hydrothermal venting in volcanic sedimentary basins: Impact on hydrocarbon maturation and paleoclimate*. Earth and Planetary Science Letters, 467, pp. 30-42.

Iyer K., Svensen H., Schmid D. W., 2017b. *SILLi 1.0: 1D Numerical Tool Quantify the Thermal Effects of Sill Intrusions*. Geoscientific Model Development Discussions, in review, https://doi.org/10.5196/gmd-2017-132.

Jamtveit B., Svensen H., Podladchikov Y. Y., Planke S., 2004. *Hydrothermal vent complexes associated with sill intrusions in sedimentary basins*. In: Breitkreuz, C. & Petford, N. (Eds) Physical Geology of High-Level Magmatic Systems. Geological Society, London, Special Publications, 234, 233–241.

Jones M. T., Jerram D. A., Svensen H. H., Grove C., 2016. *The effects of large igneous provinces on the global carbon and sulphur cycles*. Palaeogeography, Palaeoclimatology, Palaeoecology, 441, pp. 4-21.

Kerrick D. M. and Connolly J. A. D., 2001. *Metamorphic devolatilization of subducted marine sediments and the transport of volatiles into the Earth' s mantle*. Nature, 411, pp. 293-296

Killops S. and Killops V., 2005. *Introduction to organic geochemistry*. Blackwell Publishing, pp. 393.

Knight K. B., Nomade S., Renne P. R., Marzoli A, Bertrand H., Youbi N., 2004. *The Central Atlantic Magmatic Province at the Triassic-Jurassic boundary: paleomagnetic and* $^{40}Ar/^{39}Ar$ *evidence from Morocco for brief, episodic volcanism.* Earth and Planetary Science Letters, 228, pp. 143-160.

Lindström S., van de Schootbrugge B., Hansen K. H., Pedersen G. K., Alsen P., Thibault N., Dybkjær K., Bjerrum C. J., Nielsen L. H., 2017. *A new correlation of Triassic-Jurassic boundary successions in NW Europe, Nevada and Peru, and the Central Atlantic Magmatic Province: A time.line for the end-Triassic mass extinction*. Palaeogeography, Palaeoclimatology, Palaeoecology, 478, pp. 80-102.

Lindström S., Pedersen G. K., van de Schootbrugge B., Hansen K. H., Kuhlmann N., Thien J., Johansson L., Peterson H. I., Alwmark C., Dybkjær K., Weibel R., Erlström M., Nielsen L. H., Oschmann W., Tegner C., 2015. *Intense and widespread seismicity during the end-Tirassic mass extinction due to emplacement of a large igneous province*. Geology, 43, pp. 387-390.

Martindale R. C., Berelson W. M., Corsetti F. A., Bottjer D. J., West A. J., 2012. *Constraining carbonate chemistry at a potential ocean acidification event (the Triassic-Jurassic boundary) using the presence of corals and coral reefs in the fossil record*. Palaeogeography, Palaeoclimatology, Palaeooecology, 350-352, pp. 114-123.

Marzoli A., Jourdan F., Puffer J. H., Cuppone T., Tanner L. H., Weems R. E., Bertrand H., Cirilli S., Bellieni G., De Min A., 2011. *Timing and duration of Central Atlantic magmatic province in the Newark and Culpeper basins, eastern U.S.A.*. Lithos, 122, pp. 175-188.

Marzoli A., Bertrand H., Knight K. B., Cirilli S., Buratti N., Vérati C., Nomade S., Renne P. R., Youbi N., Martini R., Allenbach K., Neuwerth R., Rapaille C., Zaninetti L., Bellieni G., 2004. *Synchrony of the Central Atlantic magmatic province and the Triassic-Jurassic boundary climatic and biotic crisis*. Geology, 32, pp. 973-976.

Marzoli A., Renne P. R., Piccirillo E. M., Ernesto M., Bellieni G., De Min A., 1999. *Extensive 200-Million-Year-Old Continental Flood Basalts of the Central Atlantic Province*. Science, 284, pp. 616-618.

McElwain J. C., Wagner P. J., Hesselbo S. P., 2009. *Fossil Plant Relative Abundances Indicate Sudden Loss of Late Triassic Biodiversity in East Greenland*. Science, 324, pp. 1554-1556.

Mc Hone J. G., 2000. *Non-plume magmatism and rifting during the opening of the Central Atlantic Ocean*. Tectonophysics, 316, pp. 287-296.

Muirhead D. K., Bowden S. A., Parnell J., Schofield N., 2017. *Source rock maturation owing to igneous intrusion in rifted margin petroleum systems*. Journal of the Geological Society, https://doi.org/10.1144/jgs2017-011

Nomade S., Knight K. B., Beutel E., Renne P. R., Verati C., Féraud G., Marzoli A., Youbi N., Bertrand H., 2007. *Chronology of the Central Atlantic Magmatic Province: Implications for the Central Atlantic rifting processes and the Tirassic-Jurassic biotic crisis*. Palaeogeography, Palaeoclimatology, Palaeoecology, 244, pp. 326-344.

Olsen P., 1997. *Stratigraphic record of the Early Mesozoic breakup of Pangea in the Laurasia-Gondwana rift system*. Annual Review Earth Planet Science, 25, pp. 337-401.

Olsen P., Kent D. V., Cornet B., Witte W. K., Schlische R. W., 1996. *High-resolution stratigraphy of the Newark basin (early Mesozoic, eastern North America)*. Geological Society of America Bulletin, 108, pp. 40-77.

Olsen P. E., Sues H. D., 1986. *Correlation of continental Late Triassic and Early-Jurassic sediments, and patterns of the Triassic-Jurassic tetrapod transition*. In: Padian K. (Ed.), The Beginning of the Age of Dinosaurs. Cambridge University Press, Cambridge, UK, pp. 321–351.

Panfili G., Cirilii S., Marzoli A., Dal Corso J., Bertrand H., Medina F., Youbi Nasrrddine, 2017. *New palynological constraints show rapid emplacement of the Central Atlantic Magmatic Province during the end-Triassic mass extinction interval*. In review.

Raup D. M. and Sepkoski J. J., 1982. *Mass Extinctions in the Marine Fossil Record.* Science, 215, pp. 1501-1503.

Roden M. K., Miller D. S., 1991. *Tectono-thermal history of Hartford, Deerfield, Newark and Taylorsville Basins, eastern United States, using fission-track-analysis.* Schweizerische mineralogische und petrographische Mitteilungen, 71, pp. 187-203.

Ruhl M., Kürschner W. M., 2011. *Multiple phases of carbon cycle disturbance from large igneous province formation at the Triassic-Jurassic transition*. Geology, 39, pp. 431-434.

Ruhl M., Bonis N. R., Reichart G.J., Sinninghe Damsté J. S., Kürschner W. M., 2011. *Atmospheric Carbon Injection Linked to End-Triassic Mass Extinction*. Science, 333, pp. 430-434.

Sachse V. F., Wenke A., Littke R., Jabour H., Kluth O., Zühlke R., 2016. *2D petroleum system analysis of the Tarfaya Basin, on-offshore Morocco, North Africa*. Marine and Petroleum Geology, 77, pp. 1108-1124.

Schaller M. F., Wright J. D., Kent D.V., 2011. *Atmospheric* pCO_2 *perturbations associated with the Central Atlantic Magmatic Province*. Science, 331, pp. 1404-1409.

Schlische R. W., Andres M. H., 1996. *Stratigraphic effects and tectonic implications of the growth of normal faults and extensional basins*. In Beratan, K.K (Ed.) , Reconstructing the History of Basin and Range Extension Using Sedimentology and Stratigraphy: Boulder, Colorado. Geological Society of America Special Publication, 303, pp. 183-203.

Schoene B., Geux J., Bartolini A., Schaltegger U., Blackburn T. J., 2010. *Correlating the end-Triassic mass extinction and flood basalt volcanism at the 100 ka level*. Geology, 38, pp. 387-390.

Senger K., Millet J., Planke S., Ogata K., Haug Eide C., Festøy M., Galland O., Jerram D. A., 2017. *Effects of igneous intrusions on the petroleum system: a review*. First break, 35, pp. 1-10.

Senger K., Planke S., Polteau S., Ogata K., Svensen H., 2014. *Sill emplacemen and contact metamorphism in a siliciclastic reservoir on Svalbard, Artic Norway*. Norwegian Journal of Geology, 94, pp. 155-169.

Sigurdsson H., 1990. *Evidence of volcanic loading of the atmosphere and climate response*. Palaeogeography, Paleoclimatology, Palaeoecology, 89, pp. 277-289.

Smoot J. P., 1991. *Sedimentary facies and depositional environments of early Mesozoic Newark Supergroup basins, eastern North America*. Palaeogeography, Palaeoclimatology, Palaeoecology, 84, pp. 369-423.

Spencer L. G., Tanner L. H., 2015. *End-Triassic nonmarine biotic events*. Journal of Palaeogeography, 4, pp. 331-348.

Steckler M. S., Omar G. I., Karner G. D., Kohn B. P., 1993. *Pattern of hydrothermal circulation within the Newark basin from fission-track analysis*. Geology, 21, pp. 735-738.

Stordal F., Svensen H. H., Aarnes I., Roscher M., 2017. *Global temperature response to century-scale degassing from the Siberian Traps Large igneous province*. Palaeogeography, Palaeoclimatology, Palaeoecology, 471, pp. 96-107.

Svensen H., Iyer K., Schimd D. W., Mazzini Adriano, 2017. *Modelling of gas generation following emplacement of an igneous sill below Lusi, East Java, Indonesia.* Marine and Petroleum Geology, 30, pp. 1-8.

Svensen H., Planke S., Neumann E.R., Aarnes I., Marsh J. S., Polteau S., Harstad C. H., Chevallier L., 2015. *Sub-Volcanic Intrusions and the Link to Global Climatic and Environmental Changes.* Advances in Volcanology, pp. 1-24.

Svensen H., Fristad K. E., Polozov A. G., Sverre P., 2015. *Volatile generation and release from continental large provinces*. In Schmidt A., Fristad K.E., Elkins-Tanton L. T. (Eds), Volcanism and Global Environmental Change, Cambridge University Press, Cambridge, pp. 358.

Svensen H. and Jamtveit B., 2010. *Metamorphic Fluids and Global Environmental Changes*. Elements, 6, pp. 179-182.

Svensen H., Planke S., Polozov A. G., Schmidbauer N., Corfu F., Podlachikov Y. Y., Jamtveit B., 2009a. *Siberian gas venting and the end-Permian environmental crisis.* Earth and Planetary Science Letters, 277, pp. 490-500.

Svensen H., Schmidbauer N., Stordal F., Plake S., 2009b. *Contact metamorphism, halocarbons, and environmental crises of the past.* Environmental Chemistry, 6, pp. 466-471.

Svensen H., Sverre P., Chevallier L., Malthe-Sørenssen A., Corfu F., Jamtveit B., 2007. *Hydrothermal venting of greenhouse gases triggering Early Jurassic global warming*. Earth and Planetary Scince Letters, 256, pp. 554-566.

Svensen H., Planke S., Malthe-Sørrensen A., Jamtveit B., Myklebust R., Rasmussen Eidem T., Rey S. S., 2004. *Release of methane from a volcanic basin as a mechanism for initial Eocene global warming.* Nature, 429, pp. 542-545.

Sweeney J. J., Burnham A. K., 1990. *Evaluation of a simple model of vitrinite reflectance based on Chemical kinetics*. The American Association of Petroleum Geologists Bulletin, 74, pp. 1559-1570.

Tanner L. H., Spencer L. G., Chapman M. G., 2004. *Assessing the record and the causes of Late Triassic extinctions*. Earth-Science Reviews, 65, pp. 103-139.

Traverse A., 1988. *Plant evolution dances to a different beat*. Historical Biology, 1, pp. 277-301.

Ungerer P. and Pelet R., 1987. *Extrapolation of the kinetics of oil and gas formation from laboratory experiments to sedimentary basins*. Nature, 327, pp. 52-54.

Van Houten, 1971. *Contact Metamorphic Mineral Assemblages, Late Triassic Newark Group, New Jersey*. Contributions to Mineralogy and Petrology, 30, pp. 1-14.

Verati C., Rapaille C., Féraud G., Marzoli A., Bertrand H., Youbi N., 2007. *^{40}Ar/^{39}Ar ages and duration of the Central Atlantic Magmatic Province volcanism in Morocco and Portugal and its relation to the Triassic-Jurassic boundary*. Palaeogeography, Palaeoclimatology, Palaeoecology, 244, pp. 308-325.

Walters C. C., Kotra R. K., 1990. *Thermal maturity of the Jurassic shales from the Newark Basin, U.S.A.: influence on hydrothermal fluids and implications to basin modeling*. Applied geochemistry, 5, pp. 211-225.

Wang D., Song Y., Liu Y., Zhao M., Qi T., Liu W., 2012. *The influence of igneous intrusions on the peak temperatures of host rocks: Finite-time emplacement, evaporation, dehydration and decarbonation*. Computers and Geoscinces, 38, pp. 99-106.

Waples D. W. and Waples J. S., 2004. *A Review and Evaluation of Specific Heat Capacities of Rocks, Minerals, and Subsurface Fluids. Part 1: Minerals and Nonporous rocks*. Natural Resources Research, 13, pp. 97-122.

Ward P. D., Garrison G. H., Haggart J. W., Kring D. A., Baettie M. J., 2004. *Isotopic evidence bearing on Late Triassic extinction events, Queen Charlotte Islands, British Columbia, and implications for the duration and cause of the Triassic/Jurassic mass extinction*. Earth and Planetary Sciences Letters, 224, pp. 589-600.

Williford K. H., Ward P., Garrison G., Buick R., 2007. *An extended organic carbon-osotope record across the Triassic-Jurassic boundary in the Queen Charlotte Islands, British Columbia, Canada*. Palaeogeography, Palaeoclimatology, Palaeoecology, 244, pp. 290-296.

Wignall P. B., 2001. *Large igneous provinces and mass extinctions*. Earth-Science Reviews, 53, pp. 1-33.

Withjack M. O., Schlische R. W., Malinconico M. L., Olsen P. E., 2013. *Rift-basin development: Lessons from the Triassic-Jurassic Newark basin of eastern North America*. In: Mohriak W. U., Danforth A., Post P. J., Brown D. E., Tari G. C., Nemcok M., Sinha S. T. (Eds), Conjugate Divergent Margins. Geological Society, London. Special Publications, 369, pp. 301-321.

Wotzlaw J.F., Guex J., Bartolini A., Gallet Y., Krystyn L., McRoberts C. A., Taylor D., Schoene B., Schltegger U., 2014. *Towards accurate numerical calibration of the Late Triassic: High-precision U-Pb geochronology constraints on the duration of the Rhaetian*. Geology, 42, pp. 571-574.

Acknowledgements

First of all, I would like to thank my supervisor, Andrea Marzoli, for the great opportunity he has given me to follow him in his studies concerning the CAMP and for allowing me to make a unique experience. I want to thank him for allowing me to go to Oslo to learn to develop the SILLi model and to take me to Morocco to sample with him. I would also thank him for the infinite patience he has had to endure me and my anxiety!

I would like to thank my co-tutor, Nereo Preto, for accompanying me to the adventure in the labs and for following me during the development of the geochemical analyses.

I would like to thank all the laboratory technicians, researchers, PhD students and professors who have been assisting me or helping me during the last two years: Jacopo Dal Corso, Luca Peruzzo, Richard Spiess, Federico Zorzi, Bernardo Cesare, Manuel Rigo, Fabio Tateo, Aurelio Giaretta, Xin Jin and Leonardo Tauro.

I would like to thank Henrik Svensen, researcher at UiO University, for providing me with the scripts needed to develop the 1D model for the estimation of the amount of CO_2 release in the atmosphere. I would like to thank him for allowing me to go to Oslo to learn how to run in the correct way the model. I want to thank him for the attentions he provided me during my stay in Oslo. I also want to thank him PhD student, Thea Hatlen Heimdal, to help me in learning how to develop the 1D SILLi model. I would therefore like to thank Sara Callegaro for “l’ italianità” provided me when I was in Oslo and to help me in finding accommodation.

Many thanks to Annamaria Fioretti and Youbi Nasrrddine for having accompanied and helped my supervisor and me in collecting Moroccan samples.

I want to thank my family, because without their help today I would not be here to write thanks for this wonderful experience.

Many thanks to my friends, especially to me geo-friends (Zaga, Simo, Elena, Sofi, Puli, Pasi, Vero, Anna, Cate, Gaia, Ga, Giada, Erika, Vinci, Benji, Laura, Luca, Ale, Sturo, Pietrino, Marco, Demo…) for having been close to me in the last few months, for having borne me while I have been insulting every kind of engineer and to be able to keep up with my own extravagant ideas.

Special thanks also to the librarians of the geosciences library, Emanuela, Lorenzino e Nicolò, for helping me to look for unlikely articles and for not expelling me from the library during the moments of “sagra” that I have done.

And, in the end, many thanks to Miriam and Simone, my flatmates, for the “disagio” offered me every evening and every dinner!